Weak Lensing Analysis of Galaxy Groups

Patrícia Figueiró Spinelli

Weak Lensing Analysis of Galaxy Groups

Patrícia Figueiró Spinelli

Dissertation der Fakultät für Physik
Dissertation of the Faculty of Physics

der Ludwig-Maximilians-Universität München
at the Ludwig Maximilian University of Munich

für den Grad des
for the degree of

Doctor rerum naturalium

vorgelegt von Patrícia Figueiró Spinelli
presented by

aus Caxias do Sul, Brasilien (Brazil)
from

Munich, 06 June 2011

Zusammenfassung

Der schwache Gravitationslineneffekt ist ein wichtiges Mittel für die Untersuchung von Galaxienverbänden wie Galaxiengruppen oder -haufen. Die kohärente Verzerrung der Formen der Hintergrundgalaxien erlaubt die Bestimmung der Gesamtmasse eines Systems ohne weitere Annahmen über den dynamischen Zustand oder den Entwicklungszustand. Massenabschätzungen für Galaxiengruppen spielen in der Kosmologie eine große Rolle. Da Galaxiengruppen im Gegensatz zu -haufen über weite Rotverschiebungsbereiche beobachtet werden, wird dadurch eine Unterscheidung zwischen verschiedenen kosmologischen Modellen ermöglicht. Allerdings wirkt in diesem Zusammenhang das Gravitationsfeld des Haupthalos nicht als einzige Quelle für die Verzerrungen, da auch die gesamte Massenverteilung entlang der Sichtlinie berücksichtigt werden muss. Aufgrund der eher geringen Masse von Galaxiengruppen spielt diese Kontamination im Vergleich zur gravitativ induzierten Scherung eine nicht zu unterschätzende Rolle.

Das Ziel dieser Dissertation ist die Untersuchung von Galaxiengruppen unter Nutzung des schwachen Gravitationslineneffekts. Dabei steht vor allem die Quantifizierung der Kontamination durch Objekte entlang der Sichtlinie im Mittelpunkt. Auf Grundlage von Simulationen des COSMOS-Feldes wird das Schersignal um 165 Galaxiengruppen auf Verstärkung beziehungsweise Abschwächung des Signals des Haupthalos durch benachbarte Gruppen untersucht. Den Mock-Katalogen liegen Beobachtungen mit dem CFHT und Subaru zugrunde, aus denen photometrische Rotverschiebungen für die Objekte im Feld und eine realistische Galaxienverteilung abgeleitet werden. Die Positionen der Galaxiengruppen werden dem COSMOS-Röntgen-Katalog für ausgedehnte Quellen entnommen. Das zugrundeliegende Gruppensample hat eine Medianmasse von $M_{200} = 3.1 \times 10^{13}$ M$_\odot$ und liegt bei einer Medianrotverschiebung von $z = 0.68$. Unter der Annahme dass Galaxien durch ein Navarro-Frenk-White-Dichteprofil (NFW) beschrieben werden, berechnet sich das erwartete gravitative Scherfeld aus der Summe der durch die einzelnen Linsen induzierten Scherungen. Wir kommen zu dem Schluss, dass das Signal-zu-Rausch-Verhältnis für die Detektion eines Haupthalos im Vergleich zum isolierten Halo um $\approx 15\% \times \sqrt{n_{gal}/30}$ beeinträchtigt wird. Gruppen mit Nachbarn in geringer projizierter Entfernung ($\lesssim 1'$) werden am stärksten beeinflusst, aber auch Halos in größerer Winkeldistanz erzeugen ein durchaus messbares Signal. Diese weiter entfernten Gruppen können als unkorrelierte großskalige Strukturen interpretiert werden. Die durchschnittliche systematische Abweichung in der Massenexzessabschätzung beträgt null mit einer RMS von 6-72%, abhängig von der verwendeten Apertur. Eine Möglichkeit zur Eliminierung dieses Bias ist die Koaddition der Dichteprofile verschiedener Gruppen. Das Schersignal, das von großskaligen Strukturen erzeugt wird, wirkt dabei als externe Rauschquelle. Die dadurch eingeführte durchschnittliche Unsicherheit beträgt $\sigma_{\gamma_t}^{\mathrm{LSS}} \sim 0.006$ pro Vektorkomponente bei einer Aperturgröße von $\theta \sim 5'$. Dies entspricht $\sim 1.8\%$ des Werts einer der intrinsischen Elliptizitätskomponenten. Im Falle von Messungen von ~ 3000 Galaxien in einer bestimmten Apertur führt dieses Rauschen durch die großskaligen Strukturen zu einem Fehler in der Größenordnung des Fehlers durch die intrinsische Elliptizitätsverteilung. Da dies ein Wert ist, der bereits durch gegenwärtige Surveys wie COSMOS erreicht wird, sollte dieser Effekt nicht außer Acht gelassen werden.

Abstract

Weak gravitational lensing is an important technique to study galaxy associations such as clusters and groups. Based on the coherent distortion imprint on the shape of background galaxies, this technique is capable of measuring the total mass content of the systems under investigation without making any assumption on their dynamical or evolutionary state. Mass estimates of galaxy groups are very relevant in the field of cosmology. In contrast to galaxy clusters, groups can be found in abundance at the redshift range where one can discriminate between cosmological models. However, the shape distortion of background galaxies is not only affected by the gravitational field of the main halo but by all the mass content along the line-of-sight. Given the low mass range of galaxy groups, the line-of-sight contamination becomes very important when compared to the weak lensing shear induced by these systems. The aim of this thesis is to study galaxy groups using weak gravitational lensing as a tool. We particularly focus on the contamination introduced by line-of-sight objects. Using COSMOS shear mock data we analyze the shear profile around 165 groups and investigate the level at which the neighboring groups can enhance or suppress the shear signal from the main halo. The mock data are based on CFHT and Subaru observations, which are used to obtain the photometric redshifts of galaxies in the field, and a realistic galaxy density, given by the weak lensing distortion analysis of the observed data. We further use the X-ray information taken from the COSMOS X-ray catalog of extended sources to trace the galaxy group distribution. Our group sample is characterized by a median mass of $M_{200} = 3.1 \times 10^{13}$ $M_{\odot}$ and median redshift of $z = 0.68$. The expected gravitational shear field of these groups is calculated assuming that the halos are described by Navarro-Frenk-White (NFW) density profiles. The total shear is then computed by summing the shear over all the lenses. We conclude that, on average, the signal-to-noise for a detection of the main halo is affected by $\approx 15\% \times \sqrt{n_{gal}/30}$ with respect to the signal-to-noise the same halo would have if it was isolated in the sky, where n_{gal} is the observed galaxy density. Groups with neighbors that are close in projected distance ($\lesssim 1'$) are the most strongly affected, but halos located at larger angular distances also cause a measurable shear signal. These (angular) distant groups can be interpreted as uncorrelated large-scale structure. The average bias in the mass excess estimate of individual groups that is introduced by the external halos is zero with an rms value of $\sim 6 - 72\%$, depending on the aperture size used. One way to eliminate this bias is by stacking the density contrast profiles of several groups. The shear signal introduced by large-scale structure acts as an external source of noise. The averaged uncertainty introduced is $\sigma_{\gamma_{\rm t}}^{\rm LSS} \sim 0.006$ per component for an aperture size of $\theta \sim 5'$, which corresponds to $\sim 1.8\%$ of the one-component intrinsic ellipticity value. This large-scale structure noise error becomes equal to intrinsic ellipticity noise if there are measurements for ~ 3000 galaxies within a certain aperture, a number that is already achieved by current deep surveys such as COSMOS and, therefore, that should not be ignored.

Contents

List of Figures

List of Tables

Chapter 1

Preface

The moment this thesis is written is very exciting, but at the same time, rather controversial. We live in an epoch when large telescopes explore regions of distant objects down to the smallest detail. It is the time in which surveys map the full sky, delivering enormous amount of data on a daily basis. The time when space telescopes reveal the Universe in a way that would otherwise be invisible from the ground. There is no doubt that our knowledge about the cosmos is increasing rapidly. Yet, ironically, we do not know the nature of what appears to be the main constituents of the Universe, and naively, we call them dark energy and dark matter.

The quest for an absolute and global understanding of the Universe has triggered the development of many theoretical and observational techniques on cosmology. Among them, there is the phenomenon of weak gravitational lensing, the topic that will be introduced in details throughout this thesis.

The equivalence principle says that all bodies are affected by gravity. In fact, this statement even holds for bodies with no mass. This means that the paths chosen by light respond to the surrounding mass. As a consequence, the light distribution of galaxies carry information on the matter content the light photons have encountered on their way to Earthbound observers. This property makes gravitational lensing an unique tool to directly map the mass distribution of Universe.

Gravitational lensing is sensitive to both dark matter and dark energy and has became a valuable tool to cosmology. In fact, the weak gravitational lensing regime has been identified by the report of the Dark Energy Task Force (Albrecht et al., 2006) as one of the most promising tools to understand the nature of dark energy. In a consideration to the dark matter problem, the weak lensing analysis of clusters in an ongoing merger process is capable of probing the so-called collisionless nature[1] of dark matter (Clowe et al., 2006). If enough evidence is accumulated supporting this hypothesis, then the weak lensing technique can be

---

[1]According to the dark matter models (based on observational facts), these particles should only interact gravitationally, with a lack of internal viscosity, so that when dark matter particles move across each other there is no collisional effects.

used to confirm the validity of General Relativity at large scales and rule out theories of modified gravity (MOND).

Weak gravitational lensing is also an attractive technique to study groups and clusters of galaxies as individual systems. Since the weak lensing signal does not depend on the dynamical or evolutionary state of the systems under investigation, it has advantage upon other techniques, such as X-rays (e.g. Böhringer et al., 2000) or Sunyaev-Zeldovich effect (e.g. Birkinshaw, 1999; Carlstrom et al., 2002) for which mass estimates assume the hydrostatic equilibrium of the intra-cluster gas. However, the current systems analyzed using the weak lensing technique are biased towards galaxy clusters ($\gtrsim 10^{14}$ M$_\odot$), for which the lensing signal is stronger than for galaxy groups and, therefore, not so affected by the noise introduced by the intrinsic shape of galaxies. The weak lensing analysis of individual galaxy groups has been very limited so far, because it requires a much higher density of galaxies in order to eliminate this noise.

If on the one hand, weak lensing mass estimates of individual systems are valuable because the total mass can directly be probed, on the other hand, statistical studies of clusters and groups can be used to constrain cosmology. The number of virialized halos $n(M, z)$ of a certain mass range $[M, M + dM]$ as function of redshift z depends on the mass content of the Universe and on its evolution with time (Eke et al., 1996; Reiprich & Böhringer, 2002; Rosati et al., 2002). At high redshifts ($z \geq 0.8$), the abundance of these systems differ significantly between competing cosmological models. In this context, the weak lensing measurements of galaxy groups are particularly valuable, because they constitute the most common gravitationally bound associations of galaxies. In contrast to galaxy clusters, groups can be found in abundance at the redshift range used to discriminate between cosmological models.

In practice, weak lensing is rather challenging. The induced gravitational shear changes the intrinsic ellipticity of galaxies by a very tiny amount. For instance, galaxies have an average intrinsic ellipticity of the order of $\mathbf{e}^s \sim 0.4 \pm 0.4$, whereas the change introduced by gravitation (also measured in terms of ellipticities) is of the order of $\gamma \sim 0.03$. In other words, this means that only a few percent of the total ellipticity of galaxies is a response to gravitation, the other portion is due to their own intrinsic shapes. Because the intrinsic ellipticities are not known a priori, it is not possible to discriminate between the portions due to gravitation and to galaxy morphology. This makes weak lensing a very noisy technique, not being possible to measure the weak lensing signal of individual galaxies. To overcome this problem, the average gravitational distortion within a certain area is computed, obtained by measuring ellipticities of an ensemble of galaxies. Since the orientation of the intrinsic ellipticity of galaxies has no preferred direction and are randomly distributed[2], the portion due to intrinsic morphology is expected to be canceled out when the measurements are performed over many galaxies.

There are other sources of uncertainty which are often ignored and which limit the precision of the weak lensing measurements, such as the induced shear signal introduced by the large-scale structure (LSS) and by the possible presence of multiple halos along the line-of-sight. In case the observed gravitational shear signal is affected by such external contributors, the calculated physical parameters are not reliable.

In a consideration of the first problem, Hoekstra (2001, 2003) computed analytically the

---

[2]There are some circumstances for which this assumption breaks down, for instance, galaxies residing in a cluster tend to be mutually aligned.

contribution of the uncorrelated LSS to the mass estimates of clusters of galaxies to weak lensing measurements. Hoekstra (2001, 2003) found that the large-scale structure does not bias the mass estimate itself but it does introduce uncertainty in the measurement that can not be ignored. These findings were confirmed in a recent work (Hoekstra et al., 2011) using N-body simulations.

With regard to the second problem, Brainerd (2010) made a study of the frequency and the effect of multiple deflections in galaxy-galaxy lensing. Deflections by multiple lenses included all foreground lenses apart from the nearest lens to the source in projected distance. Brainerd (2010) concluded that if the observed gravitational shear is used to constrain fundamental parameters associated with the galaxy halo it is crucial to take the multiple lens calculations into account.

For massive galaxy clusters ($M \sim 10^{15}\,\mathrm{M_\odot}$), there is a small probability that two or more clusters can be aligned along the line-of-sight. Therefore, the distortion on the shape of a background galaxy induced by any other deflector along the line-of-sight is not comparable to the magnitude of the distortion that a massive object such as a galaxy cluster induces. This statement does not hold for less massive halos such as galaxy groups, for which the shape of a background source galaxy can be equally distorted by other groups along the line-of-sight, given that there is realistic probability of finding such a configuration. When this is the case, the total distortion measured can not be associated to an unique galaxy group.

Little work has been conducted on the weak lensing mass estimates of galaxy groups and the line-of-sight contamination. Given the importance of galaxy groups to cosmology and the advantages that weak lensing technique offers to study the mass of galaxy associations, the aim of this thesis is to study galaxy groups using weak gravitational lensing as a tool. In particular, we want to address the questions:

- Can isolated groups ($M = 10^{12} - 10^{14}\,\mathrm{M_\odot}$) be detected via the weak lensing distortion they introduce on the shape of background galaxies?
- Is it possible to measure the gravitational shear signal of an ensemble of galaxy groups?
- Can multiple halos along the line-of-sight enhance the weak lensing signal-to-noise ratio of a group detection so that it can be confused with a detection of an individual group?
- Is the contribution of close halos (in projected distance) canceled out when the gravitational shear profile of several groups is averaged? If yes, how many groups does one have to average over?
- Does the LSS noise affect the mass measurements? How much does this source of noise contribute to the total error budget?

The line-of-sight and LSS contamination of weak lensing measurements can be studied via simulations. The distortion induced by a foreground mass on the shape of a background source galaxy depends on the mass distribution of the foreground lens and on the ratio of the distance of the lens relative to the background source over the distance of the source. Hence, if the foreground mass distribution is known and the positions and redshifts of background galaxies are available, the expected shear field along the line-of-sight can be computed. The total shear is obtained by adding the contribution of all systems acting as lenses.

A robust way to set up such simulations is using observational data. The COSMOS field (Scoville et al., 2007) is an ideal data set for this purpose due to the broad wavelength coverage with which the field has been observed. The XMM-Newton and Chandra data (Finoguenov et al., 2007) provide information on the galaxy group and cluster distribution

over the redshift range $z \sim 0.07 - 1.8$. Field galaxies, for which reliable shapes can be measured, were observed with three different telescopes: CFHT, Subaru and HST. Multiwavelength imaging (Capak et al., 2007; Taniguchi et al., 2007) and spectroscopy (Lilly et al., 2007) of galaxies in the field allow to estimate the photometric redshifts of galaxies over the redshift range $z \sim 0.01 - 2.5$ (Brimioulle et al., 2008). In this work, we have used the available information on the COSMOS field to create realistic shear mock catalogs of this region. We compare how the gravitational shear changes for the case where lenses are considered as isolated systems and when they lie embedded in their environment. The results of this thesis were recently submitted to Monthly Notices of the Royal Astronomical Society journal for publication.

This thesis is organized as follows. Chapter 2 provides fundamental concepts on cosmology that will be useful to follow the analysis whereas Chapter 3 provides the necessary theoretical background for the understanding of the gravitational lensing effect. The technical and scientific aspects of this work are presented in Chapters 4–7. Chapter 4 presents the Subaru and the CFHT COSMOS data, which are used for weak lensing purposes later on. This chapter explains the details on how the data were processed and reduced in order to achieve the desired quality. Chapter 5 provides the details on the COSMOS catalogs and how they are used: in Section 5.1 the X-ray catalog is introduced and the method used to select galaxy groups is described; Section 5.2 explains how the photometric redshifts of galaxies are estimated and Section 5.3 describes how the gravitational shear catalog is computed. The information provided by these catalogs is subsequently used to create the shear mock catalogs, as explained in Chapter 6. Chapter 7 explores the current weak lensing analysis methods applied to isolated and multiple lensing mock catalogs, with the aim of answering the above scientific questions. Finally, we conclude and summarize this work in Chapter 8.

Throughout this thesis we adopt WMAP5 ΛCMD cosmology with $\Omega_{\mathrm{M}} = 0.258$, $\Omega_{\Lambda} = 0.742$ and $H_0 = 71.9 \, \mathrm{km \, s^{-1} \, Mpc^{-1}}$ (Hinshaw et al., 2009). MegaCam/CFHT and Suprime-Cam/Subaru color filters are differentiated by adding a prime (CFHT), e.g. i', and a cross (Subaru), e.g. i^+, in the filter name.

Chapter 2

The Universe

*What makes the Universe so hard to comprehend
is that there's nothing to compare it with.*

Anonymous

The first attempt to use physical laws to understand the Universe dates back to the year 1692, when Isaac Newton discussed this matter with Richard Bentley via correspondence (e.g. The Newton Project[1] and Janiak, 2009). Back then, Isaac Newton realized that his Universal Law of Gravitation, when applied to cosmological scales, could not form a homogeneous, isotropic and static Universe. More than two centuries later, with the advent of the General Relativity, Albert Einstein introduced a compelling theory of the Universe (Einstein, 1916). Einstein's field equations are given by

$$G_{\mu\nu} = \frac{8\pi G T_{\mu\nu}}{c^4} \tag{2.1}$$

and show that the space-time curvature at a given location and time is equal to the energy/matter content at that locale. But Einstein could not find a static solution for the Universe either. Thus, he included a term in his equation that he called *cosmological constant* Λ and that acted as an expulsive force to counteract gravity.

Some years later, Alexander Friedmann found an expanding Universe solution to Einstein's field equations. Friedmann's findings were subsequently supported by the observational evidence of the distance and recession velocity of galaxies, discovered by Edwin Hubble in 1929. The cosmological constant fell into oblivion until very recently, when the evidence of an accelerated expansion of the Universe revived interest in the idea.

This was the starting of what is now called cosmology, an active branch of astronomy that studies the overall structure of Universe, where the theory of General Relativity still remains the theoretical groundwork. The purpose of this chapter is to outline key concepts on cosmology that will be useful to follow this thesis. In Section 2.1 basic equations of the standard cosmological model are provided. In Section 2.2 we present the most important results from the cosmic microwave background experiment WMAP, which conceives the state-of-the-art cosmology. Finally, Section 2.3 is dedicated to the key objects of this thesis: groups and clusters of galaxies. The information compiled in this chapter was extracted from several sources

---

[1]http://www.newtonproject.sussex.ac.uk/view/texts/normalized/THEM00256

namely from the textbooks *Modern cosmology* (Dodelson, 2003); *Observational Cosmology* (Serjeant, 2010); *Groups of Galaxies in the Nearby Universe* (Saviane et al., 2007); *Encyclopedia of Astronomy and Astrophysics* (Murdin, 2001); and from the papers *The cosmological constant and dark energy* a review from Peebles & Ratra (2003) and *Five-Year Wilkinson Microwave Anisotropy Probe Observations: Data Processing, Sky Maps, and Basic Results* from Hinshaw et al. (2009).

2.1   The Standard Cosmological Model

What is meant by standard cosmological model or concordance cosmology is the best current model that describes the Universe. Observational evidence supports the idea that we live in an isotropic and homogeneous Universe (in its large-scale properties) where there is no preferred location and all individuals feel the same effects. Observations also indicate that the Universe is expanding. Such an Universe is described by a Robertson-Walker metric given by

$$ds^2 = c^2 dt^2 - a^2(t)[d\chi^2 + f_K^2(\chi)(d\theta^2 + \sin^2\theta d\phi^2)]\,. \tag{2.2}$$

This metric includes the contribution of the four space-time coordinates: the time-like coordinate dt and the spatial-like coordinates $(d\chi, d\theta, d\phi)$, with c being the speed of the light. The Robertson-Walker metric can be given in a number of different ways. The one provided here is given in a hyperspherical coordinate system and makes use of the *scale factor $a(t)$* that takes into account the expansion of the Universe. The factor $f_K(\chi)$ depends on the curvature K of the Universe, and is given by

$$f_K(\chi) = \begin{cases} K^{-1/2}\sin(K^{1/2}\chi) & (K > 0) \\ \chi & (K = 0) \\ (-K)^{-1/2}\sinh[(-K)^{1/2}\chi] & (K < 0)\,. \end{cases} \tag{2.3}$$

The curvature K determines the geometry of the Universe: when $K = 0$ the geometry is Euclidean (flat), when $K > 0$ the geometry is spherical (closed) and when $K < 0$ the geometry is hyperbolic (open). It is the density of all constituents of the Universe that regulates whether the Universe is flat, closed or open.

Scale Factor

The scale factor $a(t)$ is a central quantity for the cosmology of a growing space-time. It is a time-dependent function that parametrizes the relative expansion of the Universe. By definition, $a(t = 0) := a(t_0) = 1$ and at earlier times $a(t)$ is smaller then today. Many cosmological parameters can be written in terms of the scale factor. For instance if $\ell(t)$ is the proper distance at time t and $\ell(t_0) = \ell_0$ is the proper distance today, then

$$\ell(t) = a(t)\ell_0\,. \tag{2.4}$$

The rate of change of the distance is given by the speed $v(t) = H(t)\ell(t)$, where H is the Hubble parameter (Peebles & Ratra, 2003). Considering that $v(t) = \dot{\ell}(t) = \dot{a}(t)\ell_0$, it is possible to find

$$\frac{\dot{a}(t)}{a(t)} = H(t)\,. \tag{2.5}$$

If $v \ll c$ then $v(t) = H(t)\ell(t)$ is the Hubble's law. The notation $H(t_0) := H_0$ is used to express Hubble's parameter today. Furthermore, it is also common to parametrize the Hubble's parameter today by h defining

$$H_0 = 100\,h \;\mathrm{km\,s^{-1}\,Mpc^{-1}} \tag{2.6}$$

where h can have any positive value. In this thesis we have adopted $h = 0.72$, in agreement with the WMAP5 results as explained in the next section.

A relation between the *redshift z* and the scale factor can also be deduced. The redshift is an observable quantity, which can be measured by the displacement of spectral features of a given object to the red end of the spectrum. It is defined as

$$z = \frac{\Delta\lambda}{\lambda} = \frac{\lambda_0 - \lambda}{\lambda} \tag{2.7}$$

where λ is the wavelength of a photon emitted at time t, and the λ_0 is the observed wavelength at a posterior time t_0. When the photon is emitted the scale factor is $a(t)$. Since the photon is traveling as the Universe expands the wavelength gets stretched. If the photon is observed today, then the scale factor is $a(t_0) = 1$ and $\lambda = a(t)\lambda_0$. Thus, it is possible to infer from the redshift definition that

$$1 + z = \frac{1}{a(t)}\,. \tag{2.8}$$

With this result, it is possible to express all the time-dependent variables in cosmology in terms of the redshift z. This relation tells us that the observed redshift of objects at cosmological distances is a consequence of the expansion of the Universe.

It is worth noting that redshifts can also be attributed to the Doppler effect, which causes a shift of wavelengths to the red when the source is moving away from the observer. However, the recession velocity of cosmologically distant objects observed today are a pure consequence of the expansion of the Universe.

Friedmann Solutions of Einstein's Equation

In the last decade, observational evidence has pointed out that we are not just living in an expanding Universe, but also that this expansion is accelerated. This observationally supported result, that will be discussed in the next section, caused the revival of Einstein's cosmological constant, but now used in a different context: it has been re-introduced in order to explain the in-built tendency of the Universe to an accelerated expansion. The cosmological constant appears multiplied by the metric $g_{\mu\nu}$ added on the left-hand side of equation (2.1). The solution to Einstein's equation for a Robertson-Walker metric of equation (2.2) was derived by Friedmann in 1922. This equation can be shown to yield[2] (Friedman, 1922)

$$\left[\frac{\dot{a}(t)}{a(t)}\right]^2 = \frac{8\pi G}{3}\rho(t) - \frac{Kc^2}{a(t)^2} + \frac{\Lambda c^2}{3} \tag{2.9}$$

$$\frac{\ddot{a}(t)}{a(t)} = -\frac{4\pi G}{3}\left[\rho(t) + \frac{3p(t)}{c^2}\right] + \frac{\Lambda c^2}{3} \tag{2.10}$$

---

[2]Hereafter the tensorial notation is dropped for clarity and brevity.

with G being the gravitational constant. These equations provide the evolution of the scale factor with the time, depending on the density content of the Universe ρ and the pressure p of the matter, radiation and Λ. The solutions to the original Einstein's field equations can be recovered once $\Lambda = 0$. Combining the time derivative of equation (2.9) with (2.10) we find the conservation law in the expanding Universe

$$\frac{d\rho}{dt} + \frac{\dot{a}}{a}[3\rho + \frac{3p}{c^2}] = 0\,, \tag{2.11}$$

where the relation between the density ρ and pressure p is given by the equation of state $w = p/\rho c^2$.

Density Parameter

The amount of matter necessary in order for the Universe to be flat can be computed from Friedmann's equation (2.9) assuming that $K = 0$ and $\Lambda = 0$, so that

$$\rho_{crit} := \rho(t) = \frac{3H^2(t)}{8\pi G} \tag{2.12}$$

which is called *critical density*, because it is the turn point between an open and a closed Universe. An analysis of the total energy of the Universe $E = \mathcal{K} + U$ also leads to the critical density equation. A static Universe requires $\mathcal{K} = U$, so that

$$\frac{1}{2}m\left[H(t)\ell(t)\right]^2 = \frac{mG}{\ell(t)}\left[\frac{4\pi}{3}\rho(t)\ell(t)^3\right] \tag{2.13}$$

which gives exactly the same result as equation (2.12) since $E = 0$ yields a flat Universe. When $E > 0$, the kinetic energy $\mathcal{K}$ on the left-hand side of the equation (2.13) is higher than the potential energy U and the Universe expands forever. In the opposite situation, when $E < 0$, the Universe will contract at a certain time t, because the potential energy U is larger than the kinetic energy.

The ratio of the density of the Universe at time t to the critical density ρ_{crit} defines the dimensionless quantity

$$\Omega(t) = \frac{\rho(t)}{\rho_{crit}(t)} \tag{2.14}$$

known as the *density parameter*. It is a common practice in cosmology to derive the density parameter of each contributor responsible for the evolution of the Universe: matter, radiation, curvature and cosmological constant. From equation (2.9) and splitting the density ρ into the matter and radiation components so that $\rho = \rho_{\mathrm{M}} + \rho_{\mathrm{R}}$, we find

$$\Omega_{\mathrm{M}} = \frac{8\pi G}{3H^2}\rho_{\mathrm{M}}, \quad \Omega_{\mathrm{R}} = \frac{8\pi G}{3H^2}\rho_{\mathrm{R}}, \quad \Omega_{\Lambda} = \frac{\Lambda c^2}{3H^2} \quad \text{and} \quad \Omega_{\mathrm{K}} = -\frac{Kc^2}{a^2 H^2} \tag{2.15}$$

which leads to

$$\Omega_{\text{total}} = \Omega_{\mathrm{R}} + \Omega_{\mathrm{M}} + \Omega_{\Lambda} = 1 - \Omega_{\mathrm{K}} \tag{2.16}$$

where Ω_{R} refers to the radiation density parameter, Ω_{M} to the matter, Ω_{K} to the curvature and Ω_{Λ} to the cosmological constant term (Serjeant, 2010).

Finally, we can rearrange the terms of equation (2.11) to find a relation between the density and the scale factor

$$a^{-3} \frac{d[\rho a^3]}{dt} = -3 \frac{\dot{a}}{a} \frac{p}{c^2}. \tag{2.17}$$

Since matter has zero pressure ($w \approx 0$), $\rho_M \propto a^{-3}$. Radiation has a pressure of $p = \rho c^2/3$ ($w = 1/3$), yielding $\rho_R \propto a^{-4}$ (Dodelson, 2003). From equation (2.15) and the definition of the density parameter we can thus find

$$H(t)^2 = H_0^2 \left[\frac{\Omega_R}{a^4} + \frac{\Omega_M}{a^3} + \frac{\Omega_K}{a^2} + \Omega_\Lambda \right]. \tag{2.18}$$

Although this result is just a "work around" of the first Friedmann equation by rearranging several terms, it has the advantage that it can be related to the present-day observables. We can define it in terms of the redshift

$$H(z)^2 = H_0^2 E(z)^2 \tag{2.19}$$

where

$$E(z) := \sqrt{\Omega_R(1+z)^4 + \Omega_M(1+z)^3 + \Omega_K(1+z)^2 + \Omega_\Lambda}. \tag{2.20}$$

Distances

An expanding space-time requires special attention to be paid to the definition of distances. For instance, the physical distance[3] between two events in an expanding Universe is larger than the physical distance of the same events in a static Universe. The *comoving distance* follows the expansion, meaning that the distance of two events is kept fixed as the Universe expands (Dodelson, 2003), as illustrated in Figure 2.1. The comoving distance of two objects located at z_1 and z_2 is calculated as

$$D_c(z_1, z_2) = \frac{c}{H_0} \int_{z_1}^{z_2} \frac{dz'}{E(z')}. \tag{2.21}$$

A classic distance measurement in astronomy is the *angular distance* $D_a(z)$, which is defined as the ratio of an object's physical length ℓ to its angular size θ (in radians) as it appears on the sky (Dodelson, 2003). It is a good approximation to the proper distance, which is the distance at the time when the light left the object and is given by

$$D_a(z) = \frac{D_c}{1+z} \quad \text{and} \quad D_a = \frac{\ell}{\theta}. \tag{2.22}$$

The angular distance increases with redshift and has a maximum value at $z \sim 1.5$ where it starts to decrease as $z \to \infty$. Because of that, the angular size θ has the opposite behavior: it initially decreases with redshift but at $z \sim 1.5$ it turns over and starts to increase with redshift, as illustrated in Figure 2.2. Consequently, very distant objects appear large enough in the sky to be observed.

The proper calculation of angular distances is of great importance to gravitational lensing. We can generalize the definition of the angular distance between two objects at z_1 and z_2, by the integral

$$D_a(z_1, z_2) = \frac{c}{H_0(1+z_2)} \int_{z_1}^{z_2} \frac{dz'}{E(z')}. \tag{2.23}$$

---

[3]The real amount of space between objects far apart.
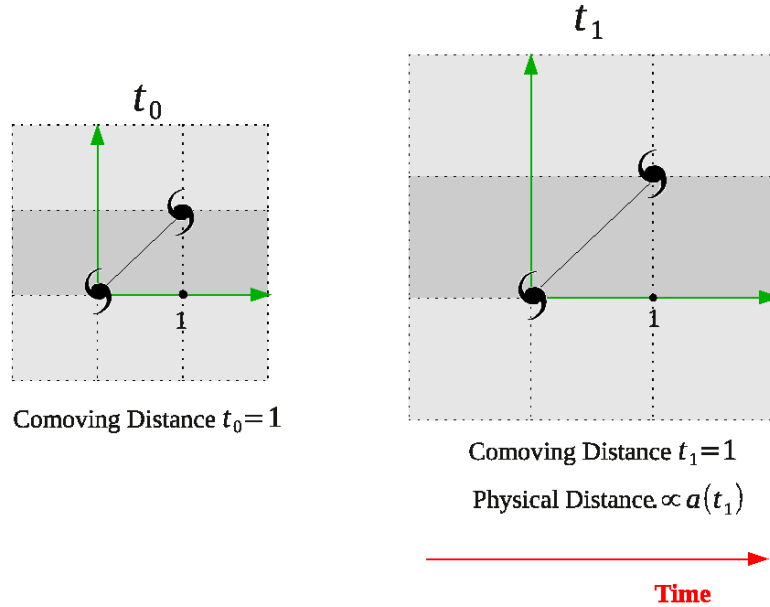
Figure 2.1: The comoving coordinate system follows the expansion of the Universe, hence the comoving distance between two objects is constant in the absence of external forces. The physical separation of the objects changes as the Universe expands and it is proportional to the scale factor times the comoving distance of the objects. Figure adapted from Dodelson, 2003.

2.2   State of the Art Cosmology

The best description of the Universe so far is illustrated in Figure 2.3. The Universe was formed a finite time ago, starting from a very dense and hot state, when space, time, matter and radiation were coupled together. At a certain time the Universe started to expand. According to this model, in the very first moments (between 10^{-33} and 10^{-32} seconds) the Universe suffered a dramatic expansion. This period is called *inflation*. As the Universe expanded, the temperature of the primordial plasma decreased. At a time of about 100 seconds the temperature had already dropped to the point that nuclear reactions were possible and the first light elements could be formed. After that, the Universe was constituted of a mixture of atomic nuclei, photons and electrons in thermal equilibrium. Photons could not escape from this opaque plasma, due to the high rate of collisions. The first time photons could travel freely was $\sim 380{,}000$ years later, when the matter and the radiation decoupled. Thus, the Universe became transparent. It took one billion years after the matter-radiation decoupling for matter to clump and form the first stars and galaxies. More recently, about 5 billion years after the Universe was formed, the expansion rate started to increase again, an effect that is observed today.

The above description is called the Lambda-Cold Dark Matter (ΛCDM) model, frequently referred to as the standard model, since it provides the best known description of the Universe. The ΛCDM model evokes the *Big Bang* theory with an adjunct inflationary theory. The success of the Big Bang theory rests on some observational facets, namely: (1) the abundance of light elements expected to be formed when the temperature of the Universe starts to decrease; (2) the receding of galaxies in all directions; (3) the observation of the primordial radiation, which is observed in the microwave region of the spectra today. In addition,
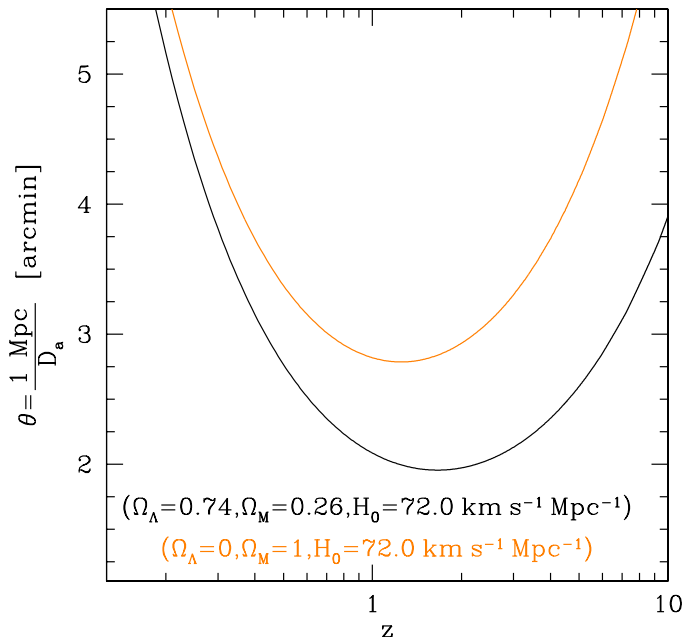
Figure 2.2: The angular size θ of an object with physical length $\ell = 1\,\mathrm{Mpc}$ as a function of redshift z for two cosmological models: Einstein-de Sitter (orange) and ΛCDM (black). The turn over at $z \sim 1.5$ makes possible the observation of distant objects because they appear large enough on the sky.

the ΛCDM model includes the existence of *dark matter*, a non-luminous type of matter which interacts only gravitationally, and *dark energy*, responsible for late-time accelerating expansion, but for which there is still no clear explanation. As we shall see in what remains of this section, the Universe appears to be composed of 72% dark energy, 23% dark matter and only 4.6% ordinary matter.

There are many techniques employed to estimate cosmological parameters that support the model described above. For instance, the evidence for an accelerating Universe was triggered by the observation of Type Ia supernovae (Riess et al., 1998; Perlmutter et al., 1999). The existence of dark matter has been confirmed by studying the motions of galaxies and galaxy clusters (e.g. Zwicky, 1937; Rubin et al., 1980; Koopmans & Treu, 2003; Clowe et al., 2006). Among all different probes, the study of the primordial radiation, or *cosmic microwave background* (CMB), brought great benefits to cosmology. The CMB spectrum is the closest approximation of a black-body spectrum ever measured in nature and has a temperature of $\bar{T} = 2.725\,\mathrm{K}$ (or $\bar{\lambda} = 1.0634\,\mu\mathrm{m}$). The observed temperature fluctuations, of the order of milli kelvins, are sensitive to the structure and evolution of the Universe as a whole.

The Wilkinson Microwave Anisotropy Probe (WMAP) experiment was able to measure the full microwave sky with a $0.0002\,\mathrm{K}$ precision. After only three years of data collection it was already considered a breakthrough science experiment. With the five-year data, described in Hinshaw et al. (2009) and Komatsu et al. (2009), to use the author's own words *no convincing deviations from the minimal six-parameter ΛCDM model* was found. This means that according to WMAP, we live in a flat Universe, dominated by a dark energy component which accelerates its expansion, and that the bulk of matter interacting gravitationally is non-luminous[4]. Table 2.1 summarizes the most important parameter values obtained from

---

[4]We call the attention to the fact that the results from seven-year data have already been published by the WMAP team. The results will not be discussed here because all the analysis employed in this thesis adopted WMAP5 cosmology. However, the quantities calculated from the seven-year data are in excellent agreement
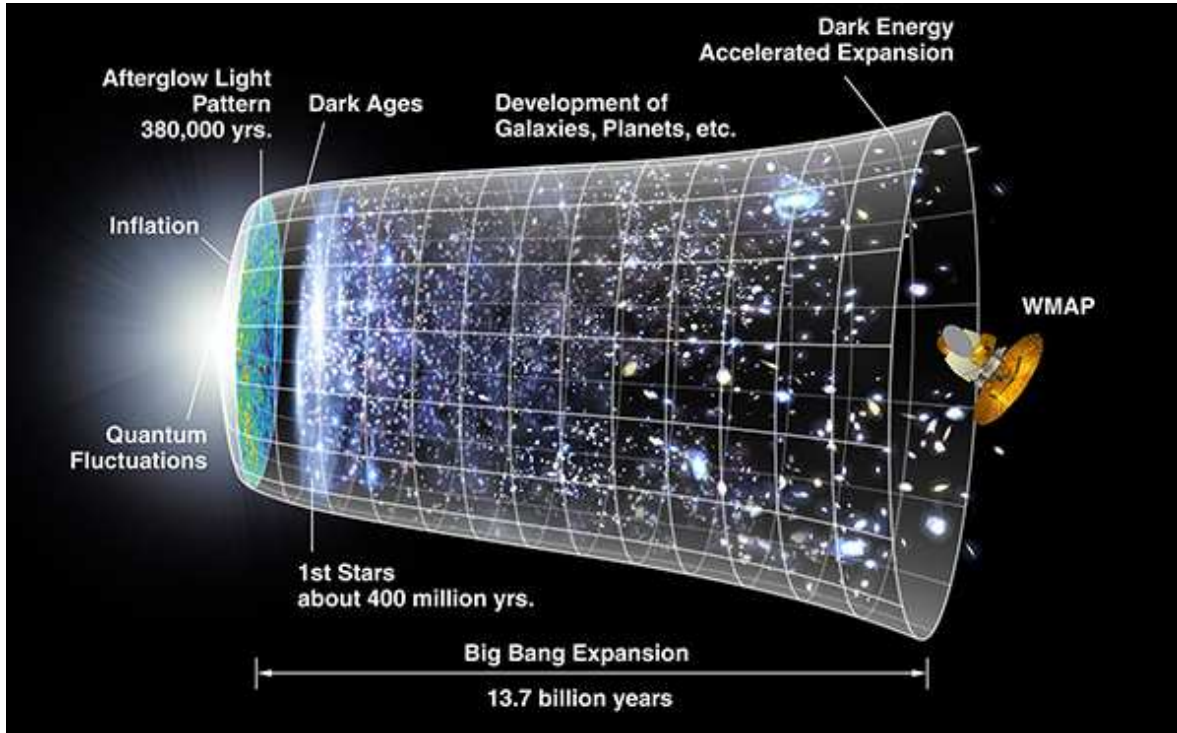
Figure 2.3: The timeline of the Universe according to the results of the WMAP experiment. The far left illustrates the earliest moments that can be probed with the experiment, when a signature of a dramatic expansion of the Universe is found. This period, called inflation, happened sometime between 10^{-33} and 10^{-32} seconds after the Universe was formed. As the Universe expanded, it got less and less dense and photons were allowed to propagate freely. This first outglow was emitted about 380,000 years after the inflation period and it is observed and used by the WMAP team to constrain the cosmological parameters. As the expansion rate gradually slowed down, the matter could couple together through gravity, creating the first stars and galaxies. On the far right, an illustration of the more recent phase of the Universe, when the expansion has begun to speed up again. The structure of the Universe is shown as observed today, after 13.7 billion years after its formation. Image credits: NASA/WMAP Science Team.

the CMB data. The values listed on the Table 2.1 are used throughout this work: $\Omega_{\mathrm{M}} = 0.258$, $\Omega_{\Lambda} = 0.742$ and $H_0 = 71.9\,\mathrm{km\ s^{-1}\ Mpc^{-1}}$.

2.3   The Clustering of Matter in the Universe

The Universe can be treated as homogeneous and isotropic when we look at the large-scale structures (hereafter called LSS), i.e., structures with sizes larger than $\sim 1000\,\mathrm{Mpc}$. On smaller scales, at the nodes of the cosmic web, we observe outstanding formations like galaxy clusters and groups. Such structures are deviations from the global homogeneity and isotropy of the Universe. A complete cosmological model must be able to explain how these structures originated.

In the standard model, structures are formed from density perturbations which occur in the early Universe and which grow with time. These perturbations are a consequence of quantum fluctuations, magnified to macroscopic scales during the inflationary period. The

---

with those from WMAP5.

Name	Symbol	Value
Age of the Universe	t_0	$13.69 \pm 0.13\,\text{Gyr}$
Hubble constant	H_0	$71.9^{+2.6}_{-2.7}\,\text{km}\,\text{s}^{-1}\,\text{Mpc}^{-1}$
Baryon density	Ω_b	0.0441 ± 0.0030
Dark matter density	Ω_c	0.214 ± 0.027
Dark energy density	Ω_Λ	0.742 ± 0.030
Fluctuation amplitude at $8h^{-1}\,\text{Mpc}$	σ_8	0.796 ± 0.036
Redshift of matter-radiation equality	z_{eq}	3176^{+151}_{150}
Total density	Ω_total	$1.099^{+0.100}_{-0.085}$
Total Matter density	Ω_M	0.2581
Radiation density	Ω_R	8.1240×10^{-5}
Curvature of the Universe	Ω_K	-0.0990

Table 2.1: Summary of the cosmological parameters as extracted from the WMAP five-year results. The values shown here are taken from Table 7 of Hinshaw et al. (2009). Some of the listed parameters are obtained directly from the fit of the data. Other parameters are derived and provided by the WMAP team. The last three parameters of the table are calculated considering that $\Omega_\text{M} = \Omega_b + \Omega_c$, $\Omega_\text{R} = \Omega_\text{M}/(1 + z_{eq})$ and $\Omega_\text{K} = 1 - \Omega_\text{total}$.

amplitude of the perturbations increases with the subsequent expansion of the Universe by gravitational instability process. When the Universe reaches the era dominated by matter, fluctuations are bounded hierarchically: small virialized systems merge to form larger halos, that eventually form the LSS observed today.

Galaxy clusters are the largest structures in the Universe that are gravitationally bound. They are also the latest to be formed, about 10 billion years ago. The study of galaxy clusters can be directly linked to understanding the formation of LSS and, consequently, to cosmology. Furthermore, since galaxies residing in clusters exhibit different properties from the ones in the field, these objects arouse astronomers' interest as individual laboratories. Groups of galaxies, in turn, are smaller associations but are more abundant than galaxy clusters. Thus, they are important for understanding galaxy evolution, since $50 - 70\%$ of the galaxies in the Universe live in groups.

Although there is no definition able to strictly distinguish galaxy clusters from groups, these systems are usually studied separately. In part, this happens because there is no clear idea of how they might be related. In the following, we highlight the most important characteristics of both structures as well as the observational techniques used to study them.

2.3.1   Clusters of Galaxies

Clusters are large collections of galaxies, typically more than fifty, bound together by gravitational attraction. Clusters are constituted of baryonic and dark matter, with a baryon over total mass fraction comparable to that measured from the CMB. The nearest clusters to the Earth are Virgo and Coma, at distances of D=14.9 Mpc (Ebeling et al., 1998) and D=94 Mpc (Struble & Rood, 1999), respectively. Only a few percent of the total mass of the Universe is in clusters.

The vast region between the galaxies in a cluster is filled by tenuous, highly ionized gas, called *intergalactic medium* (IGM). The plasma forming the IGM is the dominant baryonic component of galaxy clusters and produces thermal Bremsstrahlung, which peaks at X-ray wavelengths ($\lambda = 0.1 - 100\,\mathring{A}$). This plasma also interacts with CMB photons, producing

inverse Compton scattering which leaves a signature at millimeter wavelengths.

Only $1 - 2\%$ of galaxies in the Universe reside in clusters (Murdin, 2001), most of them early-types, with Hubble morphological classification between E and S0. The brightest cluster galaxy (BCG) is commonly used as a reference to the cluster center, since they are normally located at the kinetic center of the host. The BCGs are among the most massive elliptical galaxies in the Universe.

These are the typical properties of clusters (Murdin, 2001; Rosati et al., 2002; Serjeant, 2010; van Paradijs & Bleeker, 1999):

- Number of galaxies: 50–1000.
- Mass range: $M = 10^{14} - 10^{15} \, \mathrm{M_\odot}$.
- Radius: $R = 1 - 3 \, \mathrm{Mpc}$.
- Optical B-band luminosity: $L = 10^{11} - 10^{13} \, \mathrm{L_\odot}$.
- Velocity dispersion of galaxies: $\sigma_v = 800 - 1400 \, \mathrm{km \, s^{-1}}$.
- Temperature of the intra-cluster gas: $T = 10^7 - 10^8 \, \mathrm{K}$.
- X-ray luminosity: $L_{\mathrm{X}} = 10^{42.5} - 10^{45} \, \mathrm{erg \, s^{-1}}$.
- Baryon density: $n = 10^2 - 10^5 \, \mathrm{m^{-3}}$.
- Fraction of the gas over the total baryonic matter: $\sim 90\%$.
- Percentage of the different constituents relative to the total mass of the cluster: $\sim 1-2\%$ galaxies, $\sim 5 - 18\%$ gas, and $\sim 80\%$ dark matter.

2.3.2   Groups of Galaxies

Galaxy groups are collections of at least two galaxies located close enough to each other to be gravitationally bound. Groups constitute the most common galaxy associations, hence the evolution of the majority of galaxies happens inside a group. For instance, our own Galaxy resides within the Local Group, which contains over 40 members[5].

Groups can be observed in a wide range of dynamical states. They can be found at fully virialized stage, exhibiting properties similar to galaxy clusters, but also in the process of collapsing for the first time, like the Local Group. Not all galaxy groups are X-ray luminous objects. Systems containing few galaxies are commonly identified via optical selection methods and are designated *poor systems*. Massive evolved groups can be detected in the X-ray regime, since the intra-group medium is hot enough to shine at these wavelengths.

Contrary to clusters of galaxies, groups can be found in relative abundance at all redshifts, including $z > 1$. Local studies of galaxy groups reveal that both early- and late-type galaxy populations exist within a group. Furthermore, the galaxies within a group are strongly affected by mergers, because of the low velocity dispersion of the groups. This has a great impact on the evolution of the member galaxies.

Studies of nearby and distant groups have reported a smaller baryon over total mass fraction than the one predicted by the standard cosmological model (e.g. Giodini et al., 2009, and references therein). Possible explanations for this fact can be ascribed to several physical processes like AGN-heating, that could systematically underestimate the baryon over total mass fraction.

These are some of the typical characteristics of galaxy groups (Saviane et al., 2007; Murdin, 2001):

---

[5]For further information, see M. Irwin's web-page: http://www.ast.cam.ac.uk/˜mike/local_members.html.

- Number of galaxies: 2–50.
- Mass range: $M = 10^{12} - 10^{14}\,\mathrm{M}_\odot$.
- Radius: $R < 1.5\,\mathrm{Mpc}$.
- Velocity dispersion: $\sigma_v < 500\,\mathrm{km\,s^{-1}}$.
- Luminosity of X-ray detected groups: $L_\mathrm{X} = 10^{41} - 10^{43}\,\mathrm{erg\,s^{-1}}$.

2.3.3   Observational Methods

Bound associations of galaxies can be found and studied using different observational techniques. This section summarizes some of the most common methods applied to date.

Optical: The most natural way to find groups and clusters is to visually search for high concentrations of galaxies on the sky. The first systematic searches of clusters used photometric plates and a finding algorithm based on the luminosity of the grouped galaxies and their projected radius with respect to the center of the cluster. The catalog presented by Abell (1958) comprised of almost 1600 rich galaxy clusters. The cluster-finding technique adopted to create this catalog served as a prototype for other cluster surveys for many years.

Nowadays, group and cluster-finding techniques using optical bands depend on whether or not galaxy redshifts are available. For instance, the spatial distribution and the photometric properties of galaxies in several passbands are used in the so-called *matched filter* technique to search for and study groups and clusters when galaxy redshifts are not known (e.g. Postman et al., 1996). From the color information and the luminosity of galaxies, this method estimates the most likely redshift and the richness of the candidate system. Thus, these properties are tested against the properties of foreground and background galaxy distributions. Another method for finding clusters is the *red-sequence* technique, introduced by Gladders & Yee (2000). This method searches for regions densely populated by red galaxies. It relies on the fact that most of the galaxies living in clusters are old early-types and, therefore, clusters show an excess of red galaxies in comparison to the field.

When galaxy redshifts are available, finding algorithms search for three-dimensional clustering, evaluating how much the overdense regions differ from purely random configurations.

The most precise way to determine the redshift and the velocity dispersion of a cluster or a group is by measuring the redshift of the galaxies belonging to the system. This allows to study the velocity distribution of galaxies, calculate the mean redshift and the velocity dispersion of the cluster or group. Therefore, with spectroscopic data, kinematic studies of the groups and clusters can be performed. One advantage of the spectroscopic analysis is that it can probe a wide range of bound system masses. On the other hand, a complete analysis requires that for each galaxy belonging to a cluster or a group, a spectrum is taken. Although nowadays we have the advantage of Multi-Object Spectrograph cameras (e.g. GMOS at Gemini and VIMOS at VLT telescopes) that can take several spectra at the same time, to obtain the spectra of hundreds or thousands of galaxies can be costly. Another issue is that the signal-to-noise ratio of the spectra decreases with the increase of the redshift.

X-rays: The high temperature ($10^7 - 10^8\,\mathrm{K}$) of the gas observed in the cores of galaxy clusters makes them X-ray sources. Furthermore, since the *crossing time* for a galaxy in the center of a cluster is of the order of 10^9 years (van Paradijs & Bleeker, 1999), which is less than the age of the Universe, clusters must be bound and virialized structures.

The evolution of X-ray astronomy helped increase the number of detected galaxy clusters

and groups as well as to understand many issues about their physical nature. Current deep X-rays surveys like COSMOS (Finoguenov et al., 2007) are able to measure the flux of extended sources down to a limit of 10^{-15} erg cm^{-2} s^{-1}. This is translated into an apparent luminosity of $L_{\mathrm{X}} \sim 10^{41}$ erg s^{-1}. For comparison, normal galaxies (that are not considered X-ray luminous objects) have soft X-ray luminosities $< 10^{40}$ erg s^{-1}.

The intra-cluster gas is constituted primarily of highly-ionized atoms of hydrogen and helium. Although several emission mechanisms can play a role in the observed X-ray luminosities[6], the dominant mechanism at high temperatures is thermal Bremsstrahlung.

Unfortunately, only few clusters have detailed temperature profile measurements. Thus, the general assumption is that the particles of the cluster have an isothermal distribution, meaning that the velocity distribution is Maxwellian. Assuming that the thermal velocities of the particles of the plasma are of the same order as the velocities of galaxies, the temperature of the gas is computed as (Rosati et al., 2002)

$$\frac{3}{2}\, k_B\, T \simeq \frac{1}{2}\, \mu\, m_p\, \sigma_v{}^2 \tag{2.24}$$

$$k_B\, T \simeq 6 \left(\frac{\sigma_v}{10^3\, \mathrm{km\, s^{-1}}} \right)^2 \mathrm{keV} \tag{2.25}$$

where k_B is the Boltzmann's constant, m_p is the proton mass, μ is the mean molecular weight, with $\mu = 0.6$ for a primordial composition with a 76% fraction contributed by hydrogen. Since both gas and galaxies are assumed to share the same dynamics, $v_{\mathrm{rms}} \equiv \sigma_v$ is the root mean square of the velocities of galaxies.

The total mass of the clusters is calculated assuming that the pressure gradients balance the gravitational force or, in other words, that the systems are in hydrostatic equilibrium. The application of the hydrostatic equilibrium to spherical systems and ideal gases yields

$$M(< R) = -\frac{k_B T}{G \mu m_p} \left[\frac{d \ln \rho_{\mathrm{gas}}}{d \ln r} + \frac{d \ln T}{d \ln r} \right] r \,, \tag{2.26}$$

where $p(r) = \rho(r) k_B T / \mu m_p$ is assumed. If the temperature is constant throughout the cluster, then equation (2.26) is known as *Lame-Emden equation*.

The density profile that follows from the Lame-Emden equation has no closed form solution. Thus, an alternative is to use the β-model (Cavaliere & Fusco-Femiano, 1976). The β-model profile also describes an isothermal gas in hydrostatic equilibrium, but for which the potential well is associated with a King dark-matter density profile. The β-model is given by

$$\rho_{\mathrm{gas}}(r) = \rho_0 \left[1 + \left(\frac{r}{r_c} \right)^2 \right]^{-3\beta/2} , \tag{2.27}$$

where r_c is the core radius. The β parameter is the ratio between kinetic energy and thermal gas energy (see equation 2.24).

In practice, the observed X-ray surface brightness is measured from observations and fitted to a β-model, yielding estimates of β and r_c from which the cluster mass follows. The X-ray surface brightness profile corresponding to equation (2.27) is given by

$$I(r) = I_0 \left[1 + \left(\frac{r}{r_c} \right)^2 \right]^{-3\beta+0.5} . \tag{2.28}$$

---

[6]For example, radiative cooling and shock heating by accretion.

The X-ray luminosity L_X is proportional to the density of the gas ρ_{gas}^2 and to the volume V it encloses, therefore $L_X \propto \rho_{gas}^2 r^3$. It has also been shown that the total mass and the luminosity are related as $M \propto L_X^{3/4}$ (for more details, see Kaiser, 1986)[7]. This relation has been tested by measuring the luminosity and the total mass of several clusters using X-ray data. However, the X-ray emission is only associated with the baryonic content of the clusters and can be subject to other astrophysical processes. This is expected to introduce a potential bias in the measurements. Therefore, it is essential to perform absolute mass calibration, taking advantage of other mass measurement methods such as weak lensing. In Section 5.1 of Chapter 5, we provide further information on how physical quantities such as luminosity and temperature are obtained from X-ray observations.

One clear disadvantage of X-ray analysis of bound systems is the universal assumption of hydrostatic equilibrium, spherical symmetry and isothermally. These assumptions can be sources of systematic errors, especially when studying individual systems. This is even more important for low mass objects like groups, which nowadays can be detected and studied in the X-rays due to the high sensitivity of the current telescopes.

Sunyaev-Zel'dovich Effect: The free electrons of the hot intra-cluster gas scatter the incoming CMB photons via the inverse Compton effect, leading to a small change in the energy and frequency of CMB photons passing through the cluster. By comparing the CMB radiation near to a cluster with the CMB radiation coming through the cluster, it is possible to map the distribution of the hot intra-cluster gas. This effect is known as the thermal Sunyaev-Zel'dovich (hereafter called SZ, Sunyaev & Zeldovich, 1980) and is observed at millimeter and submillimeter wavelengths.

The SZ flux has a clear frequency signature: the intensity of the scattered radiation is reduced at low frequencies and increased at high frequencies. The turn-over happens at $\nu = 217\,\mathrm{GHz}$ (or $\lambda = 1.4\,\mathrm{mm}$), independently of the redshift of the cluster. This means that clusters cast shadows below $217\,\mathrm{GHz}$ and shine above this value.

Similar to X-ray observations, SZ observations also provide information on the intra-cluster gas. The observed SZ brightness is also associated to the total mass of a cluster assuming hydrostatic equilibrium. Furthermore, scaling relations can be obtained similarly as for X-ray measurements.

One difference from the X-ray flux is that the SZ flux Y depends linearly on the density of the gas, i.e., $Y \propto \rho_{gas}$. This means that SZ is a better probe for studying the outskirts of clusters in comparison to X-rays, because the density of the gas in these regions is smaller than the density in the cluster cores. Another advantage compared to X-ray data is that the SZ effect is redshift-independent. On the other hand, the current clusters studied with the SZ technique are biased towards high-mass systems ($M > 2 \times 10^{14}\,\mathrm{M_\odot}$), because only high-mass clusters produce an SZ signal large enough to be measured with current instruments.

Gravitational Lensing: A mass distribution like a galaxy or a galaxy cluster can act as a gravitational lens, bending the light distribution of background galaxies. This means that the observed shape distortion of background galaxies can be used to infer physical properties of the object that induces the lensing effect. The mass estimate obtained from gravitational lensing is related to the total mass of the lens, i.e., this effect is sensitive to both the baryonic and dark matter content of the lens. Furthermore, the lensing signal does not depend on the

---

[7]The actual relation is $M_{total}(L_X, z) \propto L_X^{3/4}(1+z)^{-21/8}$

dynamical or evolutionary state of the system under investigation nor makes any assumption about the baryonic physics or hydrostatic equilibrium. Therefore, gravitational lensing, the main topic of this thesis, is an important technique to study groups and clusters of galaxies.

The strong lensing effect (cf. Section 3.2 of Chapter 3 for further information on the lensing regimes) occurs in the densest regions of the Universe. Hence, this lensing regime probes the innermost regions of the mass distribution. Unfortunately, the observation of strong lensing features, such as multiple images and arcs, is limited to the angular resolution of the telescopes.

In the weak lensing regime it is possible to extend the analysis to the periphery of the clusters and groups as well as to encompass those systems which do not show any strong lensing signature. In this lensing regime, the distortion or *shear* that a halo imprint on the shape of background galaxies is very small. This distortion can not be observed by eye nor measured for individual galaxies, so the weak lensing signal is quantified by averaging the shear over many galaxies. Furthermore, the shear is measured in terms of ellipticities, but since galaxies have their own intrinsic ellipticity which is not known a priori, the intrinsic shape of galaxies adds white noise to the shear measurements. In order to eliminate this source of noise, this method requires a high-density of background galaxies that can only be achieved with very deep observations. The current systems analyzed using the weak lensing method are biased towards galaxy clusters ($\gtrsim 10^{14}$ M$_\odot$) and intermediate redshifts ($z < 1$), for which the weak lensing signal is more efficient and therefore not so strongly affected by the white noise introduced by intrinsic ellipticities. However, weak lensing detections of high-redshift clusters ($z > 1$) using deep space-based data have been reported recently in the literature.

Chapter 3 provides further information on the gravitational lensing effect, covering the theoretical and practical aspects of this method.

Chapter 3

Gravitational Lensing

Then I would feel sorry for the dear Lord.
The theory is correct anyway.

Albert Einstein, when asked about the possibility
that the experiments conducted by Sir Eddington
and the Royal astronomer Frank Dyson could
disprove the theory of General Relativity.

The theory of General Relativity was formulated in 1915 during the First World War. It brought great excitement among scientists, but it lacked of an experimental confirmation. The bending of light rays was too small to be observed in a laboratory, thus scientists had to wait the war to be ended to conduct an expedition to measure the deflection of light rays produced by the Sun. Since the deflection angle is proportional to the mass of the deflector, more massive bodies produce larger deflections. In the case of the Sun, a deflection of 1.75 seconds of arc was expected, given by the equation

$$\hat{\alpha}_\odot = \frac{4GM}{c^2\xi} = \frac{4GM_\odot}{c^2 R_\odot}$$
$$= 1.75''.$$

where ξ is the closest distance from the center of the deflector at which the light rays pass, M is the mass of the deflector, G is the gravitational constant and c the light speed. This small deflection was enough to rule out or confirm the theory of General Relativity, because it is twice as large the value obtained by the Newtonian theory.

The proposed experiment was to measure the positions of stars with and without the Sun in front of them. The presence of the Sun as a foreground object would change the apparent position of stars close to the line-of-sight of the Sun. Since the brightness of the Sun outshines the luminosity of stars during the day, this experiment could only be conducted during a solar eclipse. As soon as the war ended, a group of scientists lead by the Royal astronomer Sir Frank Watson Dyson and Sir Arthur Stanley Eddington started to prepare for the next total eclipse, which occurred in May 1919. At that time, the position of the Sun was in Hyades cluster, a dense background group of stars. This historic expedition was published on the front page of many important newspapers around the world, like the London News, reproduced in Figure 3.1. The measured deviation confirmed the General Relativity and the experiment was recognized as a major scientific achievement of the 20th century.
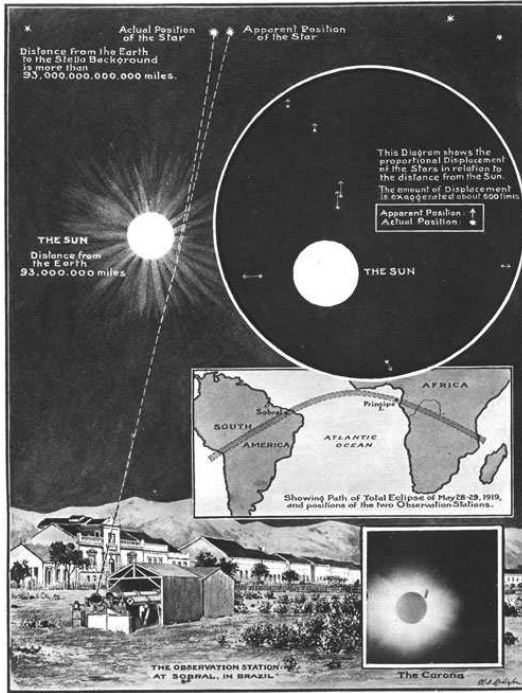
Figure 3.1: Taken from the 22 November 1919 edition of the London News. The sketch shows how the Sun bends the light rays of background stars. The stripe in the world map shows the regions where the eclipse was visible. The cities marked in the map show where the observations were made simultaneously: the Príncipe island in the current Democratic Republic of São Tomé and Príncipe, where the main team of scientists was, and in Sobral, Brazil.

The deflection of light by a massive body like the Sun is also called as gravitational lensing effect, in analogy to the distortion of the light by an optical lens. In this chapter we explore the theory of gravitational lensing, following the textbooks *Gravitational Lensing: Strong, Weak and Micro* (Schneider et al., 2006); *Gravitational Lensing: An Astrophysical Tool* (Courbin & Minniti, 2002); *The Shapes of Galaxies and their Dark Halos* (Natarajan, 2002) and the *Weak Gravitational Lensing* review from Bartelmann & Schneider (2001).

3.1   Fundamental Principles of Gravitational Lensing

Assuming the validity of General Relativity, in the gravitational lensing theory the light is treated as a collection of rays that travel in straight lines. The rays are deflected when they pass through the gravitational field produced by a massive body, which is often referred as lens or deflector. Figure 3.2 shows a sketch of the typical lensing geometry: the light emitted by a source at redshift z_s would be observed at the angular position $\boldsymbol{\beta}$, but the presence of a deflector at redshift z_d changes the light path so that the source is observed at the apparent position $\boldsymbol{\theta}$. This is a two dimensional (2D) problem in projection on the sky, where $\boldsymbol{\beta} = \boldsymbol{\beta}(\beta_1, \beta_2)$ and $\boldsymbol{\theta} = \boldsymbol{\theta}(\theta_1, \theta_2)$, for which the observer sees the images of background sources displaced from their original positions. Hereafter all the 2D quantities will be denoted with bold font. We also adopt the standard lensing notation to indicate distances: D_d, D_s and D_{ds} stands for the angular diameter distances between the observer and the lens, the observer and the source, and the lens and the source, respectively. The angular diameter distances are calculated according to equation (2.23).

If the length scale of the deflector is much smaller than the distances between observer-deflector and deflector-source, the lens is said *thin* and the involved angles are very small,
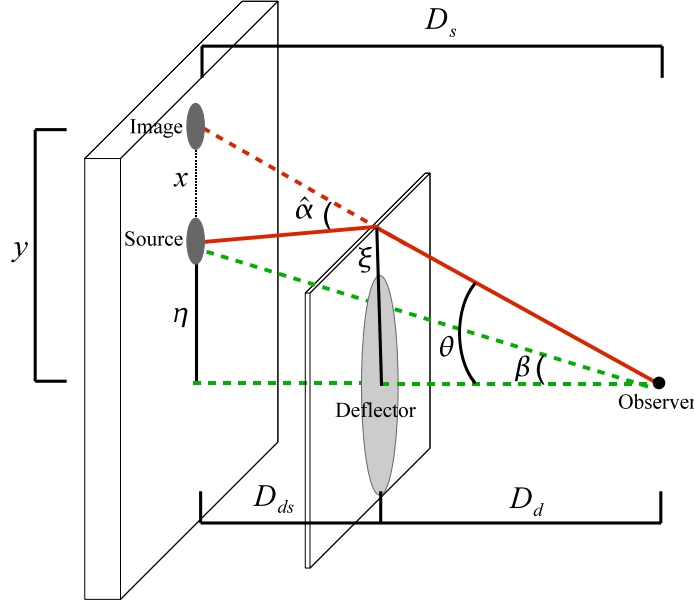
Figure 3.2: Illustration of the lens geometry: a light ray emitted by a source (e.g. a galaxy) travels on its path to the observer and encounters a deflector. In the absence of the deflector, the angular position observed would be β. Since the mass of the deflector changes the geometry of space-time, the angular position of the light ray is observed at θ.

therefore

$$\frac{y}{D_s} = \frac{\xi}{D_d}$$

$$\frac{\eta + x}{D_s} = \frac{\xi}{D_d} \tag{3.1}$$

and

$$\beta = \eta/D_s, \quad \theta = \xi/D_d \quad \text{and} \quad \hat{\alpha} = x/D_{ds} \tag{3.2}$$

where η is the position of the source in the source plane, ξ is the *impact vector* and $\hat{\alpha}$ is the *deflection angle* measured in the lens plane. Both lens and source planes are defined as planes perpendicular to a straight line from the observer to the center of mass of the lens (optical axis). Using equations (3.1) and (3.2) one obtains

$$\begin{aligned} \beta &= \frac{\xi}{D_d} - \frac{\hat{\alpha}D_{ds}}{D_s} \\ &\equiv \theta - \alpha(\theta) \end{aligned} \tag{3.3}$$

where we have introduced the *scaled deflection angle*

$$\alpha(\theta) = \hat{\alpha}\frac{D_{ds}}{D_s} \, . \tag{3.4}$$

Equation (3.3) is known as the *ray-tracing* or *lens equation* and it links the source plane to the lens plane so that it is possible to relate the true position of a source to its observed

position on the sky. From the lens equation, it follows that: (1) if the equation has more than one solution for a fixed $\boldsymbol{\beta}$, multiple images of a source is observed and (2) the shape of a source appears different after being lensed. This shape distortion happens because the light bundles are deflected differentially. In order to determine the shape of the observed image, it is necessary to solve the lens equation for all points within the extended light distribution of the source. If the source is smaller than the angular scale on which the lens properties change, then the mapping can be locally linearized

$$\begin{pmatrix} \beta_1 \\ \beta_2 \end{pmatrix} = \mathcal{A}(\boldsymbol{\theta}) \begin{pmatrix} \theta_1 \\ \theta_2 \end{pmatrix} \tag{3.5}$$

where $\mathcal{A}(\boldsymbol{\theta})$ is the Jacobian matrix.

Once the image position and the mass distribution of the lens are known, it is possible to calculate the true position of the source. For an extended mass distribution of the deflector, the measured deflection is equal to the superposition of the deflection angles produced by the infinitesimal mass elements, given by

$$\hat{\boldsymbol{\alpha}}(\boldsymbol{\xi}) = \frac{4G}{c^2} \int \Sigma(\boldsymbol{\xi}') \frac{\boldsymbol{\xi} - \boldsymbol{\xi}'}{|\boldsymbol{\xi} - \boldsymbol{\xi}'|^2} d^2\xi' \quad \text{or} \quad \boldsymbol{\alpha}(\boldsymbol{\theta}) = \frac{4G}{c^2} \frac{D_{ds}}{D_s} D_d \int \Sigma(D_d\boldsymbol{\theta}') \frac{\boldsymbol{\theta} - \boldsymbol{\theta}'}{|\boldsymbol{\theta} - \boldsymbol{\theta}'|^2} d^2\theta' , \tag{3.6}$$

where the *surface mass density* $\Sigma(\boldsymbol{\xi})$ is the three-dimensional mass density $\rho(\boldsymbol{r})$ projected along the optical axis onto the lens plane, i.e.

$$\Sigma(\boldsymbol{\xi}) = \int \rho(\boldsymbol{\xi}, z') dz' \quad \text{or} \quad \Sigma(\boldsymbol{\theta}) = \int \rho(D_d\boldsymbol{\theta}, z') dz' . \tag{3.7}$$

A simple density profile often used to approximate the mass distribution of astronomical objects like galaxies and galaxy clusters is the so-called *singular isothermal sphere* (SIS), given by

$$\rho(r) = \frac{\sigma_v^2}{2\pi G r^2} \quad \Rightarrow \quad \Sigma(\xi) = \frac{\sigma_v^2}{2G\xi} , \tag{3.8}$$

where σ_v is the value of an effective velocity dispersion. Although this model is unphysical (diverges at $r \to 0$ and has an infinity total mass), at first order, it can still be applied to the lensing properties of galaxies and clusters.

Since both deflection angle and gravitational potential depend on the mass distribution of the lens, it is possible to relate both quantities. The *2D lensing potential* ψ is defined as the three-dimensional Newtonian gravitational potential $\Phi = \Phi(\boldsymbol{\xi}, z)$ projected along the optical axis onto the lens plan and scaled in such a way that $\nabla\psi = \boldsymbol{\alpha}$, yielding

$$\psi = \frac{2}{c^2} \frac{D_{ds}}{D_s D_d} \int \Phi(D_d\boldsymbol{\theta}, z') dz' . \tag{3.9}$$

As we shall see in what remains of this section, the lensing potential has some powerful mathematical implications and from it we can derive the stretching and the amplification that the images of sources suffer after being lensed.

Applying the second derivative to the lensing potential $\nabla^2\psi = \nabla_\theta^2\psi = D_d^2\nabla_\xi^2\psi$, it results on

$$
\begin{aligned}
\nabla^2\psi &= \frac{2}{c^2}\frac{D_dD_{ds}}{D_s}\nabla_\xi^2\left[\int\Phi(D_d\boldsymbol{\theta},z')dz'\right] \\
&= \frac{2}{c^2}\frac{D_dD_{ds}}{D_s}\int\nabla_\xi^2\left[G\int\rho(\boldsymbol{\xi}',z')\frac{\boldsymbol{\xi}-\boldsymbol{\xi}'}{|\boldsymbol{\xi}-\boldsymbol{\xi}'|^2}d^2\xi'\right]dz' \\
&= \frac{2}{c^2}\frac{D_dD_{ds}}{D_s}\int G\left[4\pi\rho(\boldsymbol{\xi},z')\right]dz' \\
&= 2\frac{4\pi G}{c^2}\frac{D_dD_{ds}}{D_s}\int\rho(\boldsymbol{\xi},z')dz' \\
&= 2\frac{4\pi G}{c^2}\frac{D_dD_{ds}}{D_s}\Sigma(\boldsymbol{\theta})\,.
\end{aligned}
\tag{3.10}
$$

It is convenient to define the *dimensionless surface mass density*,

$$
\kappa(\boldsymbol{\theta}) = \frac{\Sigma(D_d\boldsymbol{\theta})}{\Sigma_{crit}}
\tag{3.11}
$$

where the *critical surface mass density* Σ_{crit} is defined as

$$
\Sigma_{crit} = \frac{c^2}{4\pi G}\frac{D_s}{D_dD_{ds}}\,.
\tag{3.12}
$$

The dimensionless surface mass density is also known as *convergence* and the formation of multiple images of a source is related to it. Thus, according to the value of κ the lensing effect is referred as *strong* or *weak*. Section 3.2 provides further information on the lensing regimes. With the convergence κ defined, we can thus rewrite equation (3.10) as

$$
\nabla^2\psi = 2\kappa
\tag{3.13}
$$

which is the 2D Poisson equation. Thus, in the lensing context, the Poisson equation describes how the lensing potential ψ is determined from the dimensionless surface mass density distribution κ.

From the combination of the second derivatives of the lensing potential, it is possible to define

$$
\gamma_1 := \frac{1}{2}\left(\frac{\partial^2\psi}{\partial\theta_1^2}-\frac{\partial^2\psi}{\partial\theta_2^2}\right)\quad\text{and}\quad\gamma_2 := \frac{\partial^2\psi}{\partial\theta_1\theta_2}=\frac{\partial^2\psi}{\partial\theta_2\theta_1}\,,
\tag{3.14}
$$

with γ_1 and γ_2 being the components of the complex quantity

$$
\boldsymbol{\gamma}\equiv\gamma_1+\mathrm{i}\,\gamma_2=|\boldsymbol{\gamma}|\mathrm{e}^{2\mathrm{i}\varphi}
\tag{3.15}
$$

called *shear*, where the phase φ is defined as the angle to the real axis and the and modulus $|\boldsymbol{\gamma}|$. The dependence on 2φ assures the invariance under rotation by $180°$. The shear is related to the distortion imprinted on the shape of the observed image: the modulus $|\boldsymbol{\gamma}|$ gives the strength and φ the direction of the distortion. For weak lensing purposes, we also define the *reduced shear*

$$
\begin{aligned}
\mathbf{g} &:= \frac{\gamma}{1-\kappa}=\frac{|\gamma|}{1-\kappa}\mathrm{e}^{2\mathrm{i}\varphi} \\
\mathbf{g} &\equiv g_1+\mathrm{i}g_2
\end{aligned}
\tag{3.16}
$$

which is also a complex quantity with similar properties to the shear. Hereafter all the complex quantities will be denoted with bold font.

So far, the derivatives of gravitational lensing potential have been associated with three important quantities: the scaled deflection angle $\boldsymbol{\alpha}$, the convergence κ and the shear $\boldsymbol{\gamma}$. All this information can be combined to derive the distortion matrix given by the Jacobian, introduced in equation (3.5), given by

$$\mathcal{A}(\boldsymbol{\theta}) = \frac{\partial \boldsymbol{\beta}}{\partial \boldsymbol{\theta}} = \left(\delta_{ij} - \frac{\partial^2 \psi(\boldsymbol{\theta})}{\partial \theta_i \partial \theta_j} \right) = \left(\begin{array}{cc} 1 - \kappa - \gamma_1 & -\gamma_2 \\ -\gamma_2 & 1 - \kappa + \gamma_1 \end{array} \right) \quad (3.17)$$

$$= (1 - \kappa) \left(\begin{array}{cc} 1 - g_1 & -g_2 \\ -g_2 & 1 + g_1 \end{array} \right) . \quad (3.18)$$

Writing in terms of its eigenvalues

$$\mathcal{A}(\boldsymbol{\theta}) = (1 - \kappa) \left(\begin{array}{cc} 1 & 0 \\ 0 & 1 \end{array} \right) - |\boldsymbol{\gamma}| \left(\begin{array}{cc} \cos 2\varphi & \sin 2\varphi \\ \sin 2\varphi & -\cos 2\varphi \end{array} \right) , \quad (3.19)$$

the Jacobian matrix $\mathcal{A}$ provides a clear interpretation of the convergence κ and the shear $\boldsymbol{\gamma}$: (1) the first term demonstrates that κ is responsible for the isotropic expansion or contraction of the images observed on the lens plane; (2) the second term shows that $\boldsymbol{\gamma}$ is responsible for the anisotropic stretching of the shape. Without the second term of equation (3.19), convergence alone would just change the size of the image, leaving its shape unchanged.

Both shear $\boldsymbol{\gamma}$ and convergence κ depend on the ratio $D_d D_{ds}/D_s$. This ratio reveals the lensing efficiency when plotted as a function of the redshift of the lens z_d, as illustrated on the left panel of Figure 3.3. Deflectors located at intermediate redshifts ($z_d = 0.25 - 0.50$) are the most efficient lenses. In addition, the ratio $D_d D_{ds}/D_s$ can be used as a cosmological test if analyzed as a function of the redshift of the sources z_s. This test is valid because different cosmologies yield in a different amplitude of the curve $D_d D_{ds}/D_s$ versus z_s. This cosmology-dependent diagnostic plot, shown on the right panel of Figure 3.3, is used when the mass of the lens and the accurate redshifts of the background sources are known.

In addition to the shape distortion, gravitational lensing of an object also produces a *magnification* of the source. Since there is a change in the size of the lensed image, the flux is not conserved. If there are no absorbers or emitters along the path of which the light bundles travel, the number of photons is conserved. In other words, this means that the surface brightness is conserved by lensing. The magnification is defined as the ratio of the observed flux from the image over the flux from the unlensed source. It is possible to formalize the magnification through the Jacobian matrix $\mathcal{A}$ as (Schneider et al., 2006)

$$\mu = \frac{1}{\det \mathcal{A}} = \frac{1}{(1 - \kappa)^2 - |\boldsymbol{\gamma}|^2} . \quad (3.20)$$

The magnification is not a frequency-dependent quantity. Instead, it is only a function of the relative change in area of the lensed to the source images.

Finally, for strong lensing purposes, we can introduce the scalar function

$$\tau(\boldsymbol{\theta}, \boldsymbol{\beta}) = \frac{1}{2}(\boldsymbol{\theta} - \boldsymbol{\beta})^2 - \psi(\theta) \quad (3.21)$$
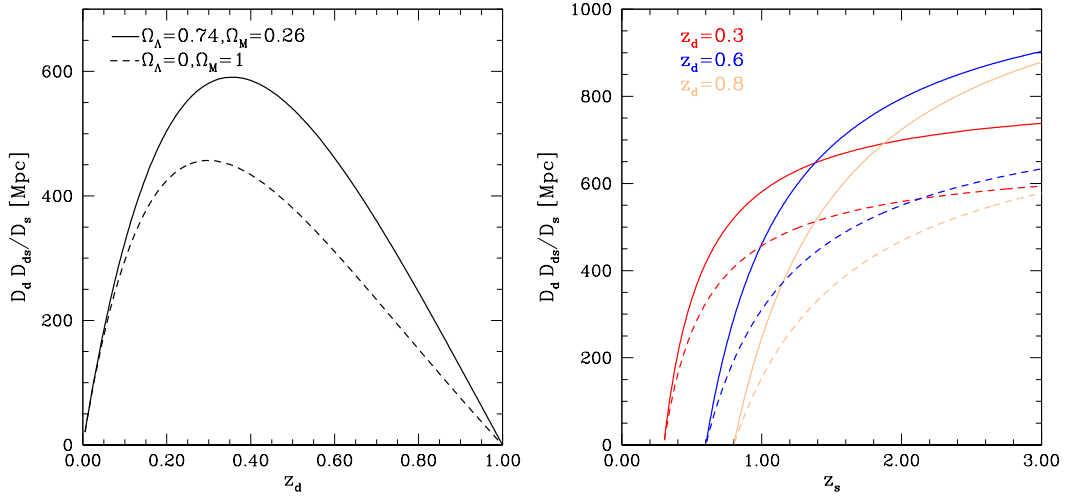
Figure 3.3: Left: The ratio $D_d D_{ds}/D_s$ as a function of the redshift of the lens for a fixed source population at $z_s = 1$. The lensing efficiency is shown for two different cosmologies: ΛCDM (solid line) and Einstein-de Sitter (dashed line) and is higher at intermediates redshifts. Right: The ratio $D_d D_{ds}/D_s$ as a function of the redshift of the sources for three different redshifts: $z_d = 0.3$ (red), $z_d = 0.6$ (blue) and $z_d = 0.8$ (orange). The two different cosmologies are differentiated by the line type as in the left panel. This plot can be used as a cosmological test when the lens parameters and the source redshifts are precisely known.

called the *Fermat potential* or the *time-delay function*. Since physical light rays take paths that make the travel time stationary, the condition to form images is

$$\nabla \tau(\boldsymbol{\theta}, \boldsymbol{\beta}) = \mathbf{0}\,. \tag{3.22}$$

This equation express the Fermat Principle and it is equivalent to the lens equation. The Fermat potential is of a great value for the understanding of multiple images in the strong lensing regime.

In conclusion, it is worth emphasizing that the gravitational lensing is an achromatic effect. This property makes the study of the lensing phenomena possible at various wavelengths. Furthermore, as shown throughout this section, gravitational lensing produces many observable effects. So far, the field of weak lensing has focused on shape measurements of sources, but magnification effects in the number counts have also been used recently. The field of strong lensing has focused on the observed relative positions and fluxes of a multiply imaged systems. Quasar lensing has focused on the time-delay between multiple images. The choice of the appropriated quantity depends on the lensing regime and the method adopted in the analysis. Table 3.1 summarizes the measurable effects explained in this section that are currently used in the lensing analysis.

3.2 Lensing Regimes

As previously mentioned, the lens equation can have more than one solution for a fixed $\boldsymbol{\beta}$. If this is the case, the source is imaged multiple times. This happens when $\Sigma \geq \Sigma_{crit}$ or $\kappa \geq 1$. Only the densest regions of the Universe can provide these spectacular lensing effects often seen in the form of giant arcs or rings. This regime is known as *strong lensing*.

Quantity	Symbol	Related to
Deflection angle	α	Change in position of the observed image relative to the true position of the source.
Convergence	κ	Isotropic change in size of the lensed image relative to the source.
Shear	$\boldsymbol{\gamma}$	Anisotropic change in size of the lensed image; magnitude and direction of the stretching.
Magnification	μ	Change in flux of the lensed object (ratio of the image flux to source flux).
Time-delay	τ	Difference in the time arrival between the paths of multiply imaged objects.

Table 3.1: Summary of the quantities defined in the lensing theory.

More representative regions of the Universe where $\Sigma < \Sigma_{crit}$ and $\kappa < 1$ need to be examined statistically. This is the domain of *weak lensing*. There is a third branch of lensing analysis called *microlensing*, which is the lensing effect originated by stellar mass objects. Microlensing is similar to strong lensing, but due to the very low lens masses involved, the displacement of light of a source can not be resolved and, therefore, this technique relies on different observational methods. In the following, we summarize the properties and applications of these three lensing regimes.

3.2.1   Strong Lensing

The strong lensing regime refers to the gravitational effect that produces multiple images, arcs and rings. The first detection of multiple images dates back to the year of 1979, when a "pair of quasars" with identical colors, redshifts and spectra was discovered by Walsh et al. (1979). Nowadays, this effect has been studied using both galaxies and galaxy clusters as foreground lenses. It probes the innermost regions of the mass distributions and can also be used to estimate cosmological parameters, such as the Hubble constant, derived through the time-delay of the multiple images of quasars (e.g. Fassnacht et al., 2002; Colley et al., 2003). Figure 3.4 shows the strong lensing effect produced by the cluster Abell 2667 and by a sample of elliptical galaxies observed with the Hubble Space Telescope.

The imaging of sources in the strong lensing regime can be studied using Fermat potential and the Jacobian matrix $\mathcal{A}(\boldsymbol{\theta})$. Images can only be formed where $\nabla\tau = 0$. This means that multiple images are located in the lens plane at a minimum, maximum or saddle points, i.e., stationary points of the Fermat potential τ.

Multiple Images

The regions on the lens plane for which the determinant $\mathcal{A}(\boldsymbol{\theta})$ vanishes are of great importance to the qualitative understanding of multiple imaging. On the lens plane, the points for which $\det|\mathcal{A}(\boldsymbol{\theta})| = 0$ form smooth closed curves called *critical curves*. Mapping them back to the source plane we obtain curves called *caustic curves*, that are not necessarily smooth, and can develop cusps. The position of a source relative to the caustics determines the number, the location, the orientation and the magnification of the multiple images. Depending on the lens model, the shape and the number of critical and caustic curves changes.
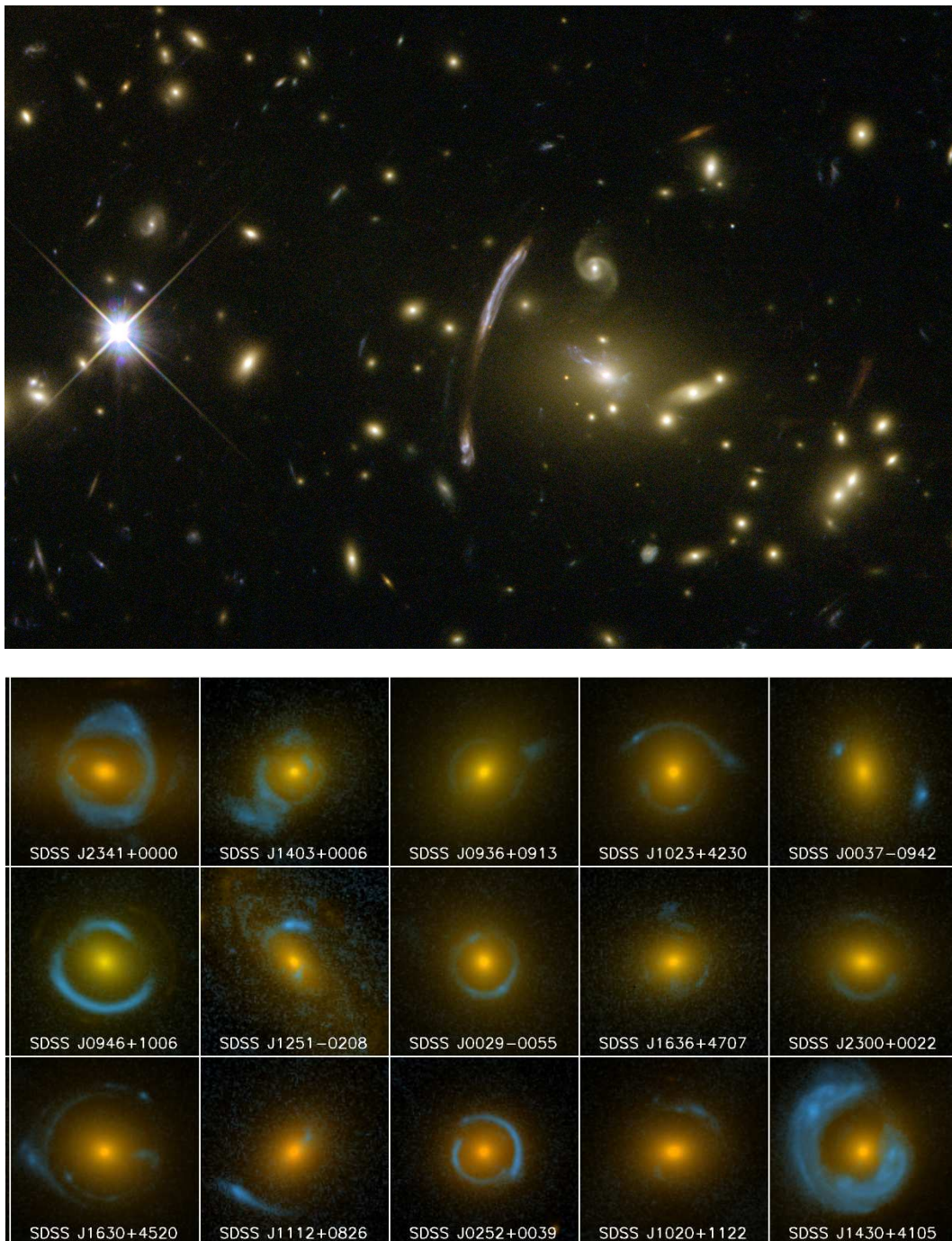
Figure 3.4: Top: The gravitational lensing effect on a galaxy behind the massive galaxy cluster Abell 2667. The yellowish galaxies are members of the galaxy cluster. The distorted galaxy, seen as a partial arc, is located at a higher redshift than the galaxy cluster. Image credits: NASA, ESA, Jean-Paul Kneib et al. Bottom: The lensing effect due to massive galaxies. The yellow elliptical galaxies act as lenses, distorting the light of the blue background galaxies. Image credits: A. Bolton, for the SLACS team and NASA/ESA.

Figure 3.5 illustrates the critical and the corresponding caustic curves of a non-singular isothermal ellipsoid lens ($\kappa(\boldsymbol{\theta}) \propto |\boldsymbol{\theta}|^{-1}$) and illustrates how the source is imaged into the lens plane. The figure shows a compact source crossing a cusp caustic (left) and a fold caustic configuration (right). An analysis of the figure provides many important aspects these curves, namely:

- Sources close to a caustic are highly magnified and their position on the lens plane is close to the corresponding critical curve.
- Sources crossing a caustic have their number of images changed by ± 2. For instance, the source represented by gray dot is imaged three times. Hence, a source within of the two caustics, as exemplified by the green and blue dots, have 2×2 extra images, totaling five images.
- Depending on whether a source lies close to a cusp or to a fold, the disposition of the multiply lensed images changes. The left panel of the figure shows a cusp caustic configuration whereas the right panel shows a fold caustic configuration.
- The outer critical curve is transformed through the lens mapping onto the inner caustic curve (dashed lines) and the inner critical curve is transformed onto the outer caustic curve (solid lines). The inner critical curve is called *radial* and the outer one *tangential*.
- For this lens model, the images near to the inner critical curve are distorted preferentially in the radial direction. Those located near to the outer critical curve are preferentially distorted in the tangential direction. As we shall see in Section 3.2.2, in the weak lensing regime, the expect distortion is always tangential.

Einstein Radius

When the source, deflector and observer are perfectly aligned, the observed lensed image can be a complete ring, called *Einstein ring*. Few complete Einstein rings have been observed so far, but there are several observations of partial ring-like systems. The radius of an Einstein ring depends on the mass distribution of the deflector. For a point-mass lens the Einstein radius is given by

$$\theta_E = \sqrt{\frac{4GM}{c^2}\frac{D_{ds}}{D_s D_d}}\,. \tag{3.23}$$

For an extended lens described by an SIS mass profile defined in equation (3.8), the Einstein radius is

$$\theta_E = 4\pi \left(\frac{\sigma_v}{c}\right)^2 \frac{D_{ds}}{D_s}\,. \tag{3.24}$$

3.2.2   Weak Lensing

Weak lensing is the study of the lensing effect that occurs in less dense environments, i.e. $\kappa < 1$. In contrast to the strong lensing regime, it can be applied to the vast majority of the Universe. The technique relies on the shape measurement of faint galaxies, that suffers a slight distortion in the presence of foreground mass concentrations. Since galaxies have their own intrinsic shape, weak lensing is a very noisy technique, not being possible to measure the weak lensing signal of individual galaxies. Instead, what is measured is the coherent distortion of many background galaxies within a region. This is the reason why weak lensing is considered a statistical technique.
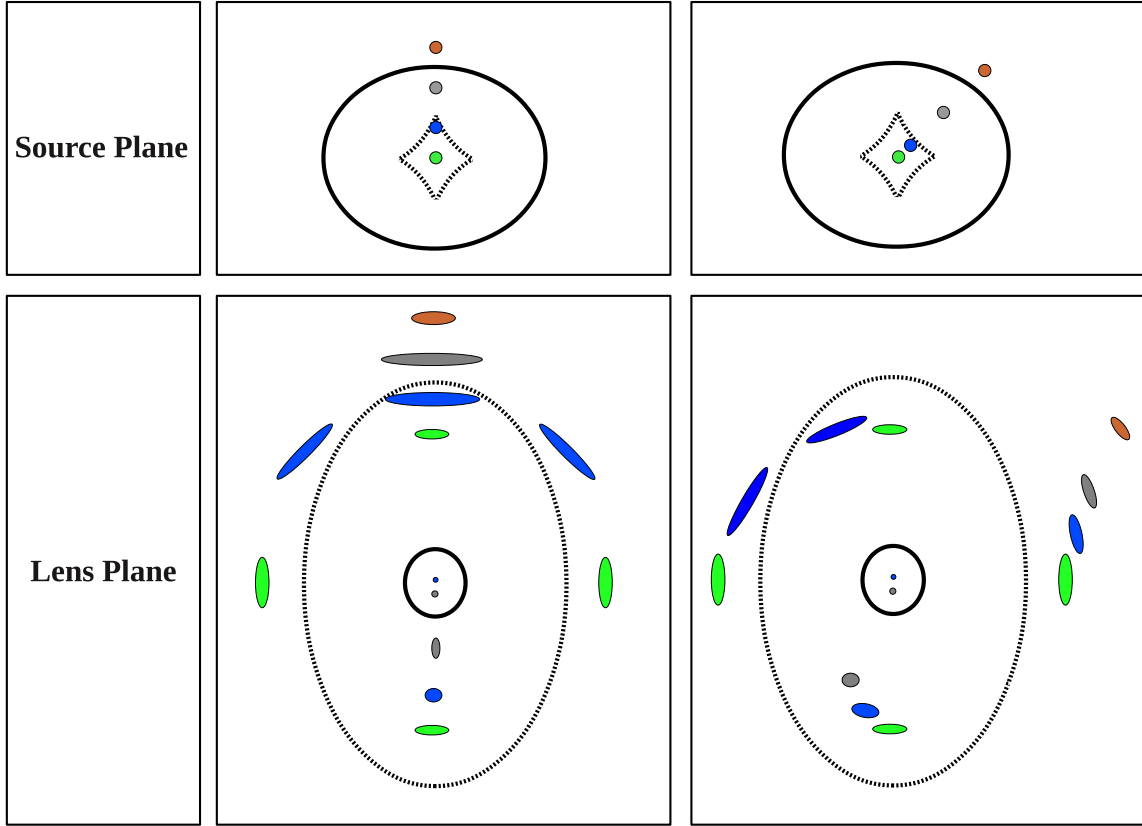
Figure 3.5: The caustic (top) and the critical (bottom) curves of a lens with a dimensionless surface mass density that follows $\kappa(\boldsymbol{\theta}) \propto |\boldsymbol{\theta}|^{-1}$. Depending on position $\boldsymbol{\beta}$ relative to the caustics (color coded in this example), a source is imaged a different number of times: (1) when it lies outside all the caustics (orange dot) the source is imaged once; (2) when it lies within one caustic (gray dot) it is imaged $2+1$ times and (3) when it lies within two caustics (blue and green dots) it is image $2 \times 2 + 1$ times. The outer critical curve is transformed onto the inner caustic (dashed lines) and is called *tangential*, whereas the inner critical curve transforms onto the outer caustic (solid lines) and is called *radial*.

In the weak lensing regime, the observed quantity is the reduced shear **g** introduced in equation (3.16). However, by definition, this regime probes non-dense regions of the Universe where $\kappa \ll 1$. Therefore, the reduced shear **g** is approximately equal to the gravitational shear $\boldsymbol{\gamma}$,

$$\mathbf{g} \approx \boldsymbol{\gamma} \,. \tag{3.25}$$

Thus, all the physical interpretations of the shear $\boldsymbol{\gamma}$ can be applied to the reduced shear **g**. It is common to find both quantities in the literature to express the shape distortion inferred by weak lenses.

Tangential and Cross Shear

The definition of the (reduced) shear provided by equations (3.16) and (3.15) are given in terms of a cartesian system, yet the shape of galaxies tend to align with the foreground mass concentration[1]. This means that, for a circular symmetric distribution, shapes are

---

[1]This is not necessarily true for the strong lensing regime.

tangentially aligned, or even radially aligned in case of an underdensity distribution. Thus, it is convenient to define a coordinate system that specifies these properties. The *tangential* and the *cross* components of the shear are given by

$$\gamma_\text{t} = -\Re\left[\boldsymbol{\gamma} \times \text{e}^{-2\text{i}\phi}\right] \quad \text{and} \quad \gamma_\text{x} = -\Im\left[\boldsymbol{\gamma} \times \text{e}^{-2\text{i}\phi}\right], \tag{3.26}$$

where ϕ is the polar angle between the horizontal axis and the position of the lensed object relative to the deflector, as illustrated in Figure 3.6. The above equations lead to

$$\gamma_\text{t} = -\gamma_1 \cos(2\phi) - \gamma_2 \sin(2\phi) \quad \text{and} \quad \gamma_\text{x} = \gamma_1 \sin(2\phi) - \gamma_2 \cos(2\phi). \tag{3.27}$$

For example, if $\boldsymbol{\gamma} = \gamma_1$ and $\phi = 90°$ there is a tangential alignment: the shear is real and positive. If $\boldsymbol{\gamma} = \gamma_1$ and $\phi = 0°$, then there is a radial alignment: the shear is real but negative. Both examples yield in a zero value for the cross shear component. This happens because gravitation can only induce tangential or radial alignments, which correspond to the real part of the shear. The cross shear, corresponding to the imaginary part, can not be induced by gravitation. If such a coherent pattern is observed, then something else is provoking it. For instance, the telescope optics or intrinsic alignments of galaxies. This makes the cross shear component a tool to search for systematic errors. Figure 3.6 illustrates the tangential and cross shear alignments.

The decomposition of the shear signal in the tangential and cross components are often referred as *E-modes* and *B-modes*. This naming convention has roots in the CMB polarization, for which the observed pattern on the sky is split into these components. The E-mode is the electric-field like decomposition or gradient-mode. The B-mode is the magnetic-field like decomposition or curl-mode. Since gravity is a conservative force, the curl is zero and the B-modes as well.

Shape Measurements: From Image Ellipticities to Gravitational Shear

Weak lensing requires precise measurements of galaxy shapes. Since this effect is expected to turn circular images into elliptical ones, a starting point to this analysis is to think in terms of ellipticities. Thus, the galaxies with elliptical isophotes have their shapes and sizes defined by the properties of the enclosed isophotes.

Since gravitational lensing conserves the surface brightness $I(\boldsymbol{\theta})$ and shapes of galaxies can be very irregular, ellipticities can be better estimated from the tensor of second moments of the surface brightness distribution, defined as

$$Q_{ij} = \frac{\int d^2\theta\, I(\boldsymbol{\theta}) q_I[I(\boldsymbol{\theta})](\theta_i - \bar{\theta}_i)(\theta_j - \bar{\theta}_j)}{\int d^2\theta\, I(\boldsymbol{\theta}) q_I[I(\boldsymbol{\theta})]}, \quad i,j \in \{1,2\}, \tag{3.28}$$

where $q_I[I(\boldsymbol{\theta})]$ is a weight function and $\bar{\boldsymbol{\theta}}$ is the center of an image located at the angular position $\boldsymbol{\theta}$ (Blandford et al., 1991). The tensor is conveniently defined in a way that its trace describes the size of the image and the traceless part contains information on the ellipticity of the image. The size of the image is given by

$$\omega = \sqrt{(Q_{11}Q_{22} - Q_{12}^2)}. \tag{3.29}$$

A circular image has $Q_{11} = Q_{22}$ and $Q_{12} = 0$ and $\omega = Q_{11} = Q_{22}$.
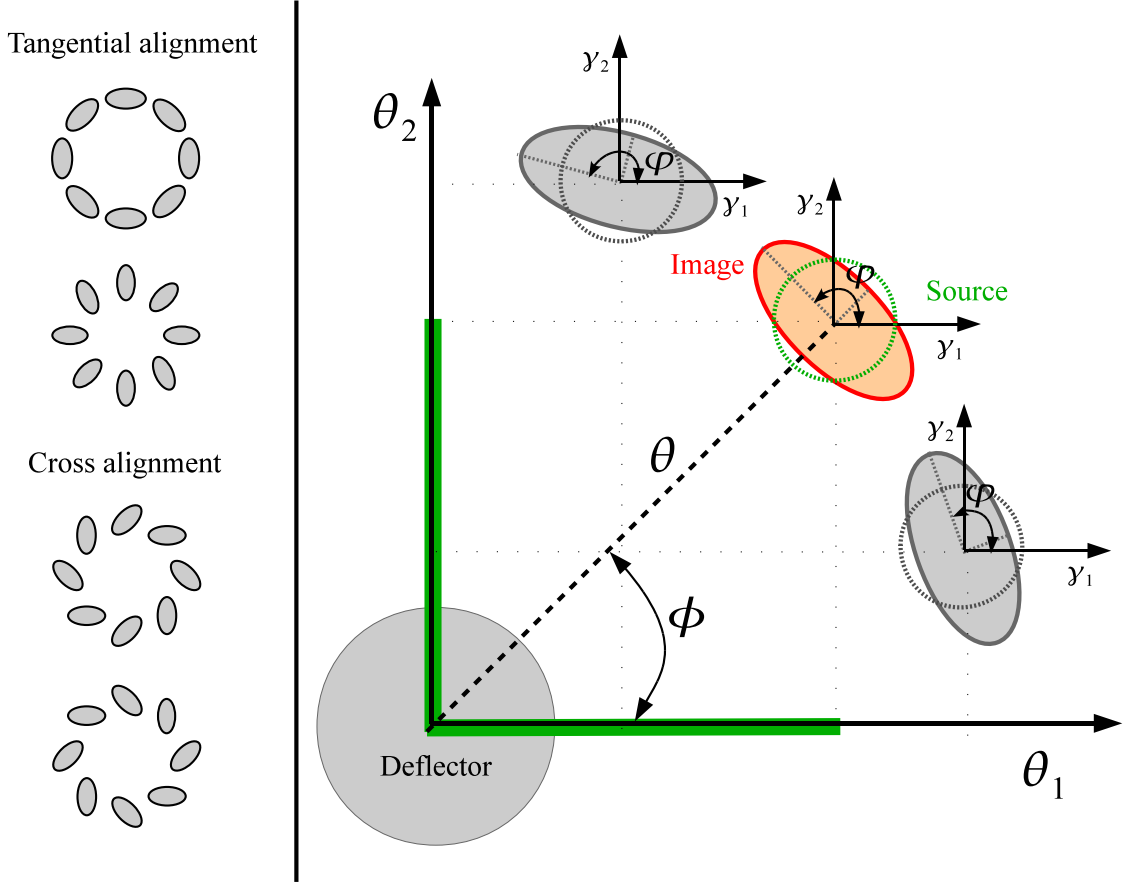
Figure 3.6: Left: Tangential and cross shear alignments in the weak lensing regime. Mass distributions can induce tangential or the radial alignments, which correspond to the real part of the shear. No mass distribution in nature can induce cross alignments. Such kind of alignments correspond to the imaginary part of the shear and can be induced by other problems affecting the observations. Right: A close look to the tangential shear and the parameters involved in its calculation. A source galaxy (e.g. the green circle) has a projected distance θ to the deflector. In the source plane, the galaxy has a circular shape. The weak gravitational lensing changes the shape of this galaxy, so that in the lens plane, its image is an ellipse (e.g. the red ellipse). The change in size is governed by the convergence κ and the distortion by the shear γ. In a cartesian system, the shear γ is expressed in terms of the components γ_1 and γ_2. In the tangential-cross coordinate system, the deflector is the reference point, so that the tangential and the cross components are computed in terms of γ_1, γ_2 and the phase ϕ.

From the second moments of the surface brightness we can define the complex ellipticity in two different ways. The first one as

$$
\begin{aligned}
\epsilon &= \frac{Q_{11} - Q_{22} + 2\mathrm{i}\,Q_{12}}{Q_{11} + Q_{22} + 2\sqrt{Q_{11}Q_{22} - Q_{12}^2}} \\
&= \epsilon_1 + \mathrm{i}\,\epsilon_2\,.
\end{aligned}
\tag{3.30}
$$

or alternatively as

$$
\begin{aligned}
\chi &= \frac{Q_{11} - Q_{22} + 2\mathrm{i}\,Q_{12}}{Q_{11} + Q_{22}} \\
&= \chi_1 + \mathrm{i}\,\chi_2\,.
\end{aligned}
\tag{3.31}
$$

Both definitions can be applied to measure the shapes of galaxies. The two complex ellipticities have the same phase, but differ in their absolute value, yet they can be converted one into the other. In the case of an object with well defined elliptical isophotes, the complex ellipticities can be related with the semi-major a and semi-minor b axis of the ellipses via

$$\boldsymbol{\epsilon} = \frac{a - b}{a + b} e^{2\mathrm{i}\phi} \quad \text{and} \quad \boldsymbol{\chi} = \frac{a^2 - b^2}{a^2 + b^2} e^{2\mathrm{i}\phi} \,. \tag{3.32}$$

We can apply equation (3.28) to the source images and define the complex ellipticities in the source plane. The transformation of ellipticities from the source to lens plane was derived by Seitz & Schneider (1995) and is given by

$$\boldsymbol{\chi}^s = \frac{\boldsymbol{\chi} - 2\mathbf{g} + \mathbf{g}^2 \boldsymbol{\chi}^*}{1 + |\mathbf{g}|^2 - 2\Re(\mathbf{g}\boldsymbol{\chi}^*)} \quad \text{and} \quad \boldsymbol{\epsilon}^s = \begin{cases} \frac{\boldsymbol{\epsilon} - \mathbf{g}}{1 - \mathbf{g}^* \boldsymbol{\epsilon}} & \text{if} \quad |\mathbf{g}| \le 1 \\[2ex] \frac{1 - \mathbf{g}\boldsymbol{\epsilon}^*}{\boldsymbol{\epsilon}^* - \mathbf{g}^*} & \text{if} \quad |\mathbf{g}| > 1 \,. \end{cases} \tag{3.33}$$

By interchanging the source and image ellipticities and $\mathbf{g} \to -\mathbf{g}$ in these equations, one obtains the inverse transformation of ellipticities, i.e, the image ellipticities are calculated from the source ellipticities.

Eventually, after defining image ellipticities from the measurement of the light distribution of galaxies, we can relate the ellipticities to the induced gravitational (reduced) shear. If all galaxies were intrinsically circular (null ellipticity), weak gravitational lensing effect would change the shape of galaxies to ellipses. Thus, the (reduced) shear could directly be estimated from the shape of the observed galaxies. However, galaxies are not intrinsically round and have ellipticities spread over all the range of possible values. Since we live in an isotropic and homogeneous Universe, there is no preferred direction to where galaxies tend to align. Therefore, the orientation of galaxy shapes is randomly distributed. Consequently, when averaged over many galaxies, the expected value of the probability distribution of intrinsic ellipticities is zero

$$\langle \boldsymbol{\chi}^s \rangle = \langle \boldsymbol{\epsilon}^s \rangle = 0 \,. \tag{3.34}$$

This means that, by measuring ellipticities of distant galaxies within a certain region, we can get an unbiased estimate of the local shear field. The relation of the image ellipticities and the (reduced) shear has been shown to yield (Schneider & Seitz, 1995; Schramm & Kayser, 1995; Seitz & Schneider, 1997)

$$\frac{\langle \boldsymbol{\chi} \rangle}{2} \approx \langle \boldsymbol{\epsilon} \rangle \approx \mathbf{g} \approx \boldsymbol{\gamma} \,. \tag{3.35}$$

Therefore, in the weak gravitational lensing limit, the observed shape of a source galaxy is directly related to the lensing induced (reduced) shear according to

$$\boldsymbol{\epsilon} = \epsilon_1 + \mathrm{i}\,\epsilon_2 = (\epsilon_1^s + \gamma_1) + \mathrm{i}\,(\epsilon_2^s + \gamma_2) \tag{3.36}$$

$$\boldsymbol{\chi} = \chi_1 + \mathrm{i}\,\chi_2 = (\chi_1^s + 2\gamma_1) + \mathrm{i}\,(\chi_2^s + 2\gamma_2) \,. \tag{3.37}$$

Since is not possible to infer the induced (reduced) shear from one single galaxy, the accuracy of the (reduced) shear estimate depends on the number of galaxies within a region where shapes can be measured. It is this characteristic that establishes the "statistical" nature of the weak lensing regime. In this sense, the noise defined as

$$\sigma_{\boldsymbol{\epsilon}} = \sqrt{\langle \boldsymbol{\epsilon}^s \boldsymbol{\epsilon}^{s*} \rangle} \quad \text{and} \quad \sigma_{\boldsymbol{\chi}} = \sqrt{\langle \boldsymbol{\chi}^s \boldsymbol{\chi}^{s*} \rangle} \tag{3.38}$$
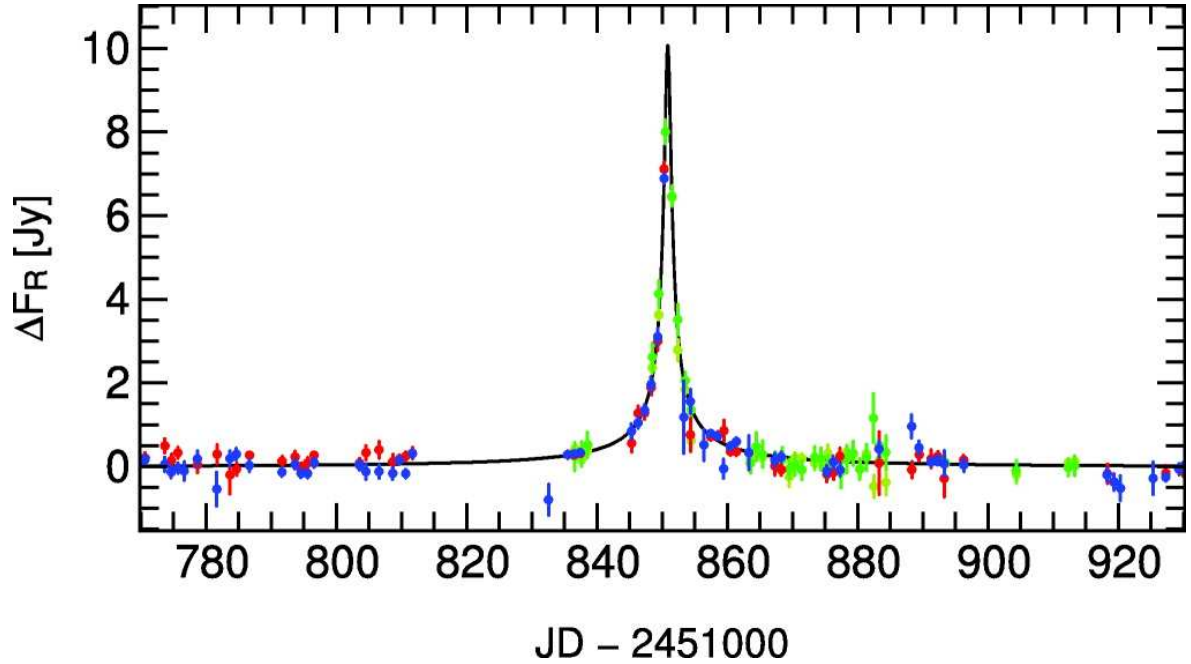
Figure 3.7: Light Curve of the M31 microlensing event WeCAPP-GL1/POINT-AGAPE-S3 (Riffeser et al., 2008). Data points with error bars show the measured flux with three different filters (color coded) and the solid line shows the best-fit microlensing light curve.

and can be reduced by measuring the ellipticities over N galaxies, so that

$$\frac{\sigma_\epsilon}{\sqrt{N}} \quad \text{and} \quad \frac{\sigma_\chi}{\sqrt{N}} \,. \tag{3.39}$$

3.2.3 Microlensing

A representative case of study of a microlensing event is the lensing effect of a single foreground star on a single background star in the Milky Way or Local Group. Unfortunately, such a configuration has very low probability to happen ($\sim 10^{-6}$ for each potential lens), even considering the regions densely populated by lenses and sources, like the Galactic plane.

Stars have their proper motion and when they move, passing by in front of a background source, they produce a change in the apparent brightness of the source. The timescale on which this change is observed varies from seconds to years and, therefore, this effect can be monitored. The microlensing effect can be detected by studying the light curve of objects, hence monitoring dense stellar fields where potential lenses and sources can be found. Thus, a microlensing event is a transient phenomenon.

Microlensing can also be used to find extrasolar planets and to constrain the fraction of massive compact halos (MACHOS) in the Galaxy. The first microlensing observation was reported in 1993. Current surveys used to monitor microlensing events are also useful for other branches of astronomy, namely stellar statistics and variability. Microlensing can be discriminated from other phenomena involving the flux variation of a source by the lack of chromatic effects in the form. Figure 3.7 shows the light curve of a microlensing event reported by Riffeser et al. (2008).

Chapter 4

Data Reduction

The COSMOS field (α=10:00:28.6, δ=+02:12:21.0) is the largest contiguous area imaged deeply with Hubble Space Telescope (HST) using the Advanced Camera for Surveys (ACS). With the primary goal of studying the formation and evolution of galaxies as a function of redshift (Scoville et al., 2007), the field covers approximately 1.64 degrees^2 and has also been imaged with many other telescopes. The wavelength coverage spans from X-rays to radio. In this work we use CFHT u^*, g', r', i' and z' bands, H band obtained with CAHA telescope and COSMOS public K_s band, obtained with KPNO and CTIO telescopes, to derive multi-color catalogs and photometric redshifts. CFHT i' and Subaru i^+ bands are used in the gravitational shear analysis and X-ray data observed with XMM-Newton and Chandra are used to trace the galaxy groups and clusters.

In this chapter we describe the data reduction of the images used in the lensing analysis. In Section 4.1 we briefly discuss the major concerns of a weak lensing optimized data reduction. In Section 4.2 we discuss the Subaru data set and the reduction, illustrating each reduction procedure. We also provide an overview of the Subaru data found in the COSMOS archive and explain why these public data are not satisfactory for a weak lensing study. Section 4.3 follows with a summary of the CFHT data which were processed and kindly provided by Michael Lerchster. Table 4.1 provides a summary of the data used in the lensing analysis.

The CFHT reduction procedure described in this chapter was also applied for the other CFHT bands (u^*, g', r' and z'). The CAHA H band is described in Gabasch et al. (2008). The KPNO and CTIO K_s band data were retrieved from the COSMOS archive[1] and the details

---

[1] http://irsa.ipac.caltech.edu/data/COSMOS/images/

Telescope	EXP_TIME	mag$_{lim}$[c]	Seeing	Astrometry[d]	Area	Pixel Scale
CFHT i'	~ 32.5[a] h	26.9	$0.71''$	$0.14''$	1.00 degrees^2	$0.186''$
Subaru i^+	~ 0.7[b] h	26.0	$0.60''$	$0.22''$	0.55 degrees^2	$0.200''$

Table 4.1: Summary of the data used in the lensing analysis.

[a] For the lensing analysis we only stack exposures taken during CFHT MegaPrime phase three.
[b] We only stack individual exposures taken with the same camera orientation angle and offset between different exposures less then $3'$.
[c] The 5σ limiting magnitude within $2''$ diameter aperture.
[d] With respect to SDSS-R6 catalog.

of the reduction are given by Capak et al. (2007). The X-ray data used in the derivation of the catalog of extended sources can be found in Finoguenov et al. (2007) and Finoguenov et al. in preparation.

4.1 Weak Lensing Optimized Data Reduction

The data reduction is a standard procedure to take before the scientific analysis of astronomical images. It consists of several actions to eliminate all kinds of systematics or artifacts in the observed images that are not produced by the astronomical target. It also consists in finding the correct mapping from the image coordinates to the real positions on the sky, as well as the co-addition of all the individual exposures to obtain a final image. As in any other field of astronomy, the images observed with the aim of performing a weak lensing analysis also need to be reduced. Besides that, the weak lensing also requires a special care with the observational strategy adopted and atmospheric conditions at which images are observed.

Observational Strategy

In the weak lensing analysis observations taken with long exposures and which cover a wide-field area of the sky are highly desirable. The first requirement comes from the fact that the signal-to-noise of a weak lensing detection depends on the number of background galaxies that shapes can be measured. Taking observations with long integration time means that the weak lensing signal is measured more accurately because statistics are favored by a higher number of galaxies. The second requirement concerns the angular scale that groups and cluster of galaxies occupy on the sky, which is typically $> 3'$. In order to measure the weak lensing signal in the outskirts of a cluster, it is important to take measurements at large radii. Even if the desired experiment does not involve the analysis of a galaxy cluster, wide-field coverage is still necessary. For instance, the galaxy-galaxy lensing analysis needs wide coverage in order to find sufficient lenses and lensed objects in the field.

The turbulence in the Earth's atmosphere blurs the objects, making their image rounder, but the turbulence can also smear the shape of faint galaxies. This effect is called *seeing* and it is estimated from the full width at half maximum (FWHM) of the seeing disk, which is also referred as the point spread function (PSF) of the images. Since weak lensing relies on the shape measurements of galaxies, the larger the seeing is, the larger are the correction factors that have to be applied. Therefore the observations should be taken under good seeing conditions. A value is considered reasonable if it is smaller than one second of arc. On the other hand, extremely good seeing conditions ($\lesssim 0.5''$) can also be problematic. In superb atmospheric conditions, objects achieve the saturation level at lower magnitudes. Furthermore, if the PSF size is of the order of 1–2 pixels, then the PSF shape can not be well measured anymore. The saturation problem is crucial for objects that appear very bright in the observed image, like stars or galaxies at low redshifts. The latter is not a problem for the weak lensing analysis which the aim is to measure the shape of faint distant objects. The real problem is when stars get saturated, because stars are not only needed for the astrometric correction but also for the lensing analysis, as we shall see in Section 5.3 of Chapter 5. If the seeing conditions are extremely good, images have to be taken with shorter exposure time, but then the readout noise is increased.

Another very important aspect to consider when planing the observations is how the individual exposures are shifted in relation to each other. As it will be discussed, this shift,

also called *dither pattern*, is necessary because there might be pixels which can not collect information properly. Because wide-field cameras normally exhibit large distortions across the field of view, which need to be corrected during the lensing analysis, if objects lie in very different positions of the CCD camera in each exposure, the resulting distortion pattern of a final stacked image might be impossible correct. Therefore, a cautionary dither pattern is the one for which the shift between exposures are small but sufficient to get information of the sky at all pixel positions in the final image.

Bias and Flat-Field Images

The pixels of a camera have intrinsically different sensitivities and also suffer from an inhomogeneous illumination pattern. All these effects have to be eliminated in order to proper study the light distribution of the astronomical targets.

The CCD camera is a particle detector measuring the rate that the photons arrive at the telescope. The detector is subject to instrumental signatures that can generate pixel-to-pixel variations. In order to eliminate this effect, an image with no light in the detector and with a very short integration time is taken and subtracted from the images to be analyzed. This image is taken with the shutter of the camera closed and is called *bias image*, because it carries the information on the electronic noise of the camera and possible systematics.

Another reason to have pixel-to-pixel variation comes from the fact that the pixels of the camera have different sensitivities. By subtracting the bias this effect does not vanish because this is a multiplicative effect. Furthermore, some pixels can collect more light because the telescope does not illuminate the CCD camera homogeneously. These two effects are corrected by the division of a *flat-field image*, which consists of an image taken from a blank field. A flat-field image can be taken from a screen on the wall (domeflats) or from the a region of the sky free from gradients (for instance, during twilight). The latter option is better because it preserves the natural pattern of light in sky.

Bad Pixels and Cosmic Rays

Some pixels do not respond correctly to the flux they receive or are simply dead. In order to produce a final stacked image with the correct information at all pixel positions, a shift between the individual exposures has to be applied.

Pixels can also be hit by cosmic rays. Cosmics are typically much smaller than the PSF and need to be removed from the images. Individual exposures are hit by different cosmics at different positions. There are several ways to remove them. One way is to mask them out in the individual exposures. Another possibility is to identify the cosmic positions in the single frames and assign a null value at these positions in the corresponding weight image.

Astrometric Solution

Individual exposures have to be co-added matching the true positions of celestial objects and not their pixel positions. The mapping between the sky coordinates to the pixel coordinates is called *astrometric solution*. In general, this mapping is not linear. This is specially true for multi-chip cameras with a large field-of-view for which the distortions are larger. If the astrometric solution is not estimated properly, then the co-addition of individual exposures can mimic a shear signal. Astrometric solution is normally done by matching the positions of point sources objects with the positions of an external catalog.

Co-addition

Co-addition is the last step in data reduction and refers to the procedure of resampling and combining the individual exposures into a final image. There are many ways to combine images: taking the average of pixel values, summing, extracting the median value, among others. Since weak lensing analysis consists of the measurements of faint galaxies, it is important to detect and measure these faint sources on properly weighted images. Therefore, it is customary to obtain *weight images* of the individual exposed frames and combine the science images using an weighted mean co-addition. When the weighted mean co-addition is employed the final flux of each pixel is

$$\langle F \rangle = \frac{w_1 f_1 + w_2 f_2 + w_3 f_3 + ... + w_N f_N}{w_1 + w_2 + w_3 + ... + w_N} \tag{4.1}$$

where N is the number of images observed, f_i is the flux value at i-th pixel and w_i is the weight value at the same pixel position. Weight images should contain information on the noise properties of each frame. It is also possible to identify the damaged pixels of each individual exposure and assign them a null value in their corresponding weight frame, so that in the final co-addition, these bad pixels are not considered.

Bad Regions

The final stacked image might have areas that can potentially infer error on the shape measurements. For example, asteroid tracks, cosmics and, in the case of wide-field cameras, off-axis reflections and scattered light from bright stars. Such areas should be masked. Masks are normally produced by a visual inspection of the images. For wide-coverage surveys, it is possible to set automatic programs to search for these regions.

4.2   Subaru

With a diameter of $8.2\,\mathrm{m}$, Subaru is among the world's largest telescopes operating in the optical and near infrared wavelengths. The data set used in our lensing analysis were imaged with Suprime-Cam instrument as part of the COSMOS project (PI: Taniguchi). The Suprime-Cam imager is composed of an array of 2×5 CCDs of 2048×4096 pixels each, with a pixel size of $0.20''$. The field-of-view of the camera is $\sim 34' \times 27'$.

Several pointings were necessary to cover the whole COSMOS area. The observations of i^+ band were taken during two nights in January and February 2004. Two observational strategies were adopted: the first needed 12 pointings to cover the total area, which used a short exposure time; the second needed 9 pointings, for which a longer integration time was employed. There was a third strategy, but the individual exposures taken with it were not included in the final co-added mosaic provided in the COSMOS archive. Nevertheless, these data can be retrieved from the Subaru archive. A sketch of the two proposed dither patterns are show in Figure 4.1, where each rectangle represents one pointing. For these two strategies, for some of the pointings, the data were taken with the camera rotated by 90 degrees. Each of the proposed dither patterns was observed four times, yielding in 8 configurations that covers the entire field-of-view. More details on the strategy of the observations can be found in Taniguchi et al. (2007).
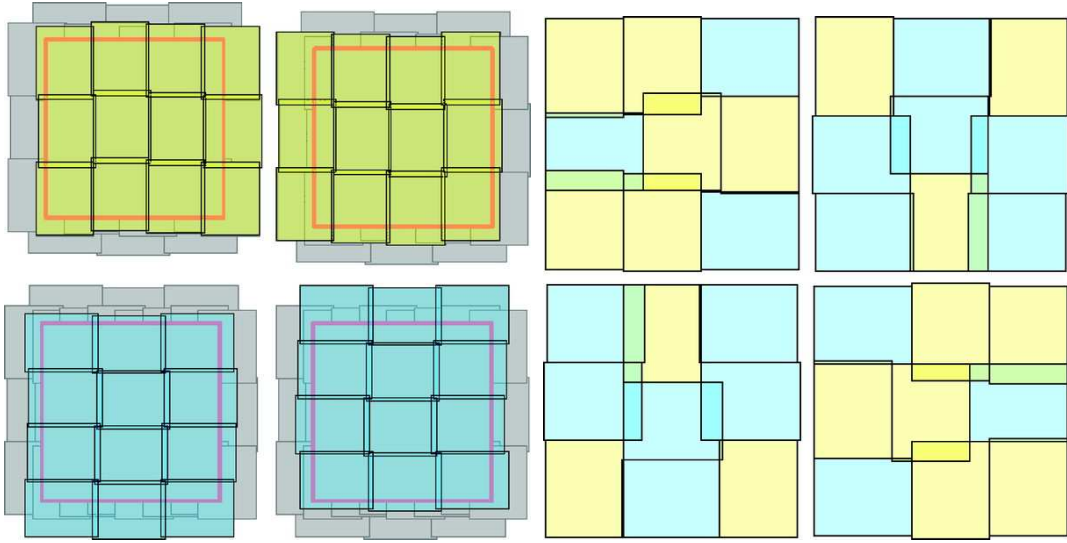
Figure 4.1: Observational strategy designed to cover the COSMOS field. Each of the colored rectangles (green, yellow, light blue) corresponds to one Suprime-Cam pointing, which covers $\sim 34' \times 27'$. The COSMOS total area was observed four times using the patterns on left and four times using the patterns on the right. Both strategies involved the orientation of the camera. Figure taken from Taniguchi et al. (2007).

COSMOS Public Data - Overview

The individual exposures were co-added into a final mosaic and divided in tiles of $10' \times 10'$, totaling 144 tiles. In the COSMOS archive it is possible to retrieve both the full mosaic or the tiled images.

The primary use of Subaru data was the creation of multi-color and photometric redshifts catalogs used to compute photometric redshifts of galaxies. Observations taken with other telescopes were also used to derive multi-color catalogs. The final mosaic of all COSMOS observations, and consequently the tiled images, were convolved with a kernel so that the PSF size of all observations match the image with worst seeing. Hence, the Subaru images that can be downloaded from COSMOS archive have a seeing of $1.6''$. But because Subaru i^+ and r^+ images were taken under superb atmospheric conditions (seeing $< 0.5''$) it is also possible to find in the archive the stacked data obtained only with good seeing exposures in the archive. The quality of both matched-psf and best-psf archival data can be seen on the top panel of Figure 4.9.

The matched-psf and best-psf images are not suitable for a weak lensing analysis for various reasons. One is due to dither pattern adopted. Combining individual exposures that were taken with different camera orientations results in a distortion pattern that can not be modeled. As already discussed, the correction of the distortion of the camera is crucial in the weak lensing analysis. This problem is further addressed and illustrated in the Section 5.3, Figure 5.6. A second reason is because the matched-psf images have a seeing too large. On the other hand, the best-psf images have an excellent seeing, but a large amount of saturated stars, compromising the correction of the camera distortions since this depends on the stars in the field-of-view (FOV). Another problem is that, as can be seen in Figure 4.9, saturated pixels had their values assigned to zero. This is extremely problematic for the detection of objects. For all these reasons, we decided that the best solution was to process the Subaru

data again taking raw images from the Subaru archive.

Data Reduction of the Raw Frames Retrieved from the Subaru Archive

We have retrieved the i^+ band science frames and flat-field images from the Subaru public archive[2]. The data are reduced and processed using the standard Suprime-Cam data reduction package `SDFRED` (Yagi et al., 2002; Ouchi et al., 2004), the Image Reduction and Analysis Facility (`IRAF`)[3] as well as the `AstrOmatic` softwares[4]: `SExtractor` (Bertin & Arnouts, 1996), `SCAMP` (Bertin, 2006), `SWarp`[5] and `Weight Watcher` (Marmo & Bertin, 2008). A pipeline that performs the Subaru data reduction automatically using the mentioned tools was developed. The aim of this hybrid pipeline is to perform the weak lensing data reduction of large amounts of Subaru data. It fulfills requirements such as the creation of weight files, extraction of the astrometric and photometric solutions, that the Subaru pipeline `SDFRED` does not provide. The hybrid pipeline consists of a script mainly written is Bash that invokes the aforementioned tools.

For each CCD frame, we estimate and subtract the bias and correct by flat-field. Master flats used in the flat-field process are constructed using sky-flats observed during the same night as the science images. Since the observations were taken during two different nights, for each night a master flat-field was created using 14 single exposures normalized to the unity and then averaged using a 3 sigma clipping algorithm to reject offset pixels. The master flats are created using the `IRAF` *imcombine* task. After the flat-field correction, a residual scattered light was still visible on the images. This is corrected with a super-flat created out of the already flat-fielded data. The super-flat is obtained out of 25 exposures for one night and 90 exposures for the other. Figure 4.2 shows an example of a raw exposure, its correction for bias and flat-field and the resulting image after the super-flat is applied.

Some CCD chips are affected with an obscuration in few hundred rows of the data. These areas are shaded off by the Acquisition Guiding (AG) of the telescope and need to be masked out. Figure 4.3 shows an example of a CCD chip with obscuration and the mask applied.

For each CCD frame we create a weight and a flag image using the `Weight Watcher`. The weight maps take into account the pixel-to-pixel variation in sensitivity, cosmic rays hits and bad regions (bad and hot pixels). The weight values depend on the pixel sensitivity and damaged pixels are assigned a zero weight. The information on saturated pixels is carried by the flag images. Figure 4.4 shows the flag and weight images corresponding to the exposure shown in Figure 4.2.

The global astrometric solution is computed with `SCAMP`, taking the SDSS-R6 as reference catalog (Adelman-McCarthy et al., 2008). We match the positions of the reference catalog to the positions of the detected objects in our science images. The sources are extracted from the science images with `SExtractor`. The flag and weight images are used in the source extraction to help to filter out blended and corrupted detections. The rms value of the position difference is $\sim 0.22''$ with respect to SDSS-R6 catalogs.

The data are co-added using `SWarp` on a pointing basis. A pointing is defined according to the rotation of the camera and the dither pattern, so that only exposures with the same camera orientation angle and offset less then $3'$ are stacked together. A total of 26 pointings

---

[2]http://smoka.nao.ac.jp/search.jsp

[3]http://iraf.noao.edu/

[4]http://www.astromatic.net/

[5]Bertin, E. 2008, SWarp v2.17.0 User's guide (http://www.astromatic.net/software/swarp/)
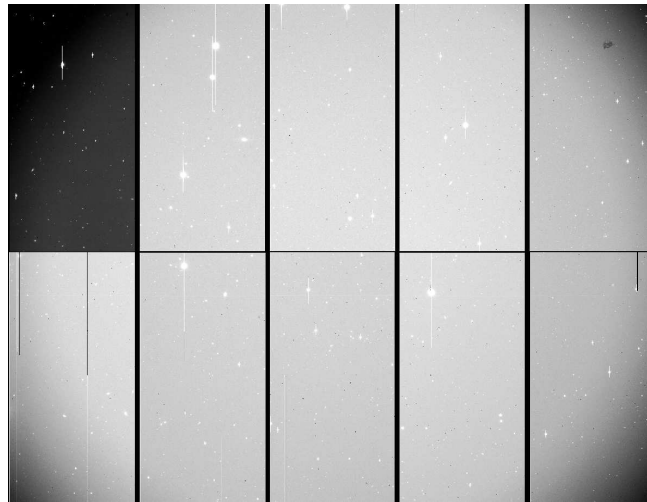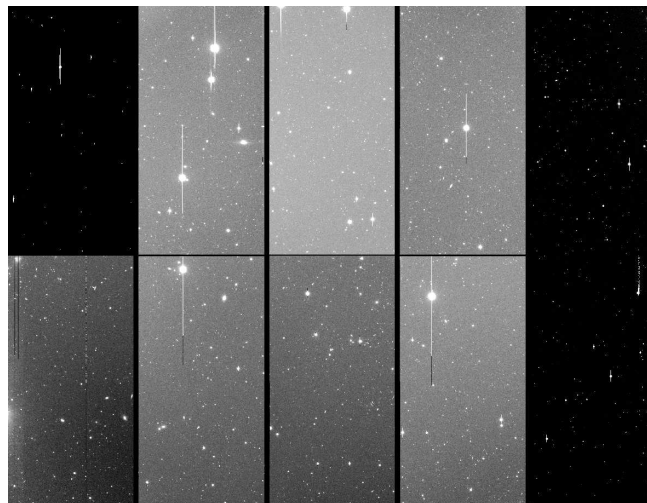
(a) Raw science image

(b) Bias and flat-field corrected image
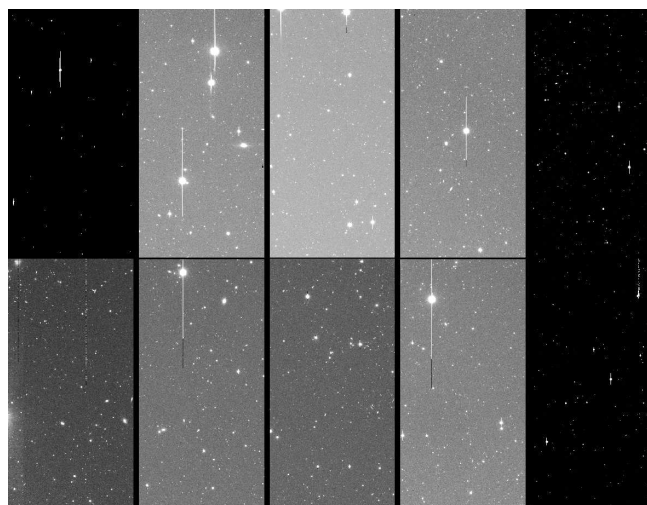
(c) Super flat-field corrected image

Figure 4.2: Panel (a): Raw science image of one Subaru exposure. The raw image shows the different CCD chips sensitivities, the inhomogeneous illumination of the camera and the bad columns of pixels. Panel (b): The same image after the bias and flat-field correction. A gradient from top to bottom of a scattered light is still visible. Panel (c): Image after the super-flat field correction.
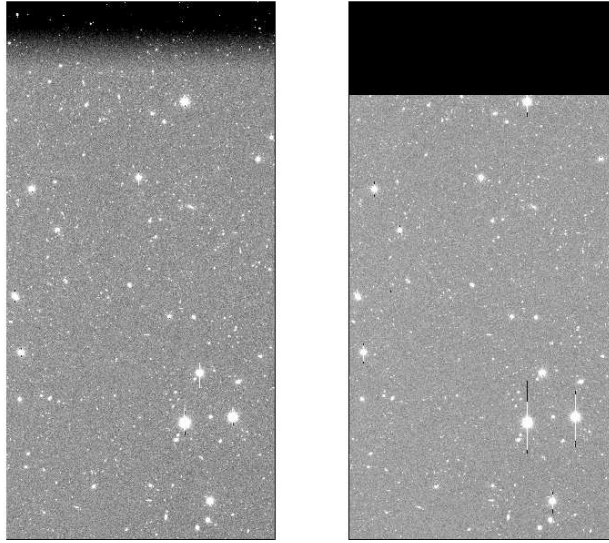
Figure 4.3: CCD chip shaded off by the AG probe of the telescope (left) and the corresponding mask created (right).

is obtained, which are shown in Figure 4.5. We adopt this strategy because, as previously mentioned, the Subaru PSF pattern exhibits large distortions across the field-of-view. By stacking all the data, the resulting PSF pattern can not be corrected to the level required in the lensing analysis. This co-addition strategy results in shallow images. There are, however, two pointings with a higher depth and, therefore, we decided to use only these pointings in our analysis. The position of these two pointings in the field-of-view are shown in blue in the left panel of Figure 4.5.

We use the LANCZOS3 kernel to resample the pixels according to the astrometric solution found. The co-addition is performed using a weighted mean combination. During the stacking process the sky background is also subtracted and the photometric correction is applied. The co-added science images have a pixel size of 0.2″ and are accompanied by a weight map and a flag image, containing information on the noise properties of the final stack and saturated pixels, respectively. Figure 4.6 shows of the final co-added image and its weight map for one of the pointings used in our lensing analysis.

Bright stars halos and diffraction spikes, under-density halos around large galaxies, asteroids tracks and cosmic hits are masked out. This masking procedure is done semi-automatically as described in Erben et al. (2009) and was performed and provided in kind by Michael Lerchster. After that, masks are visually inspected and corrected. Subaru masks cover about ∼ 15% of the total area. Figure 4.7 shows a region of the Subaru image where several masks had to be applied.

4.3 CFHT

The data taken from the Canada-France-Hawaii Telescope (CFHT) used in this work were collected in the framework of the Canada-French-Hawaii-Telescope Legacy Survey (CFHTLS), observed with the MegaPrime/MegaCam instrument. The CFHT is a 3.6 m telescope operating in the optical and infrared bands. The MegaCam instrument is composed of an array

(a) Flag image (b) Weight image
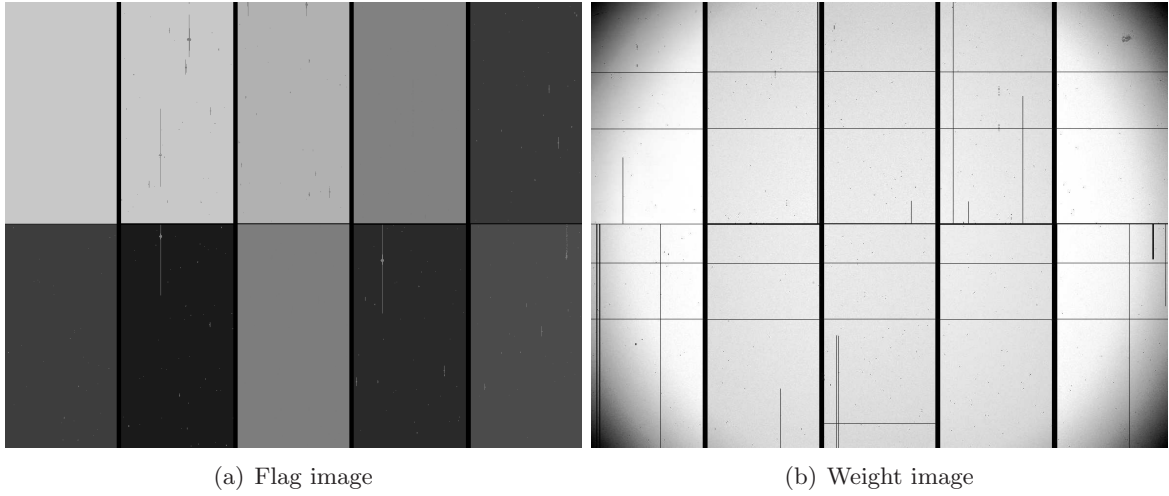
Figure 4.4: The flag image (left) has the pixel values set to 1 in the regions where pixels got saturated in the science images. The other regions of the image have the pixel value set to zero. The weight image (right) has the pixel values varying according to the pixel sensitivity of the detector. Corrupted pixels, such as bad pixels or pixels hit by cosmics, receive a zero weight value.
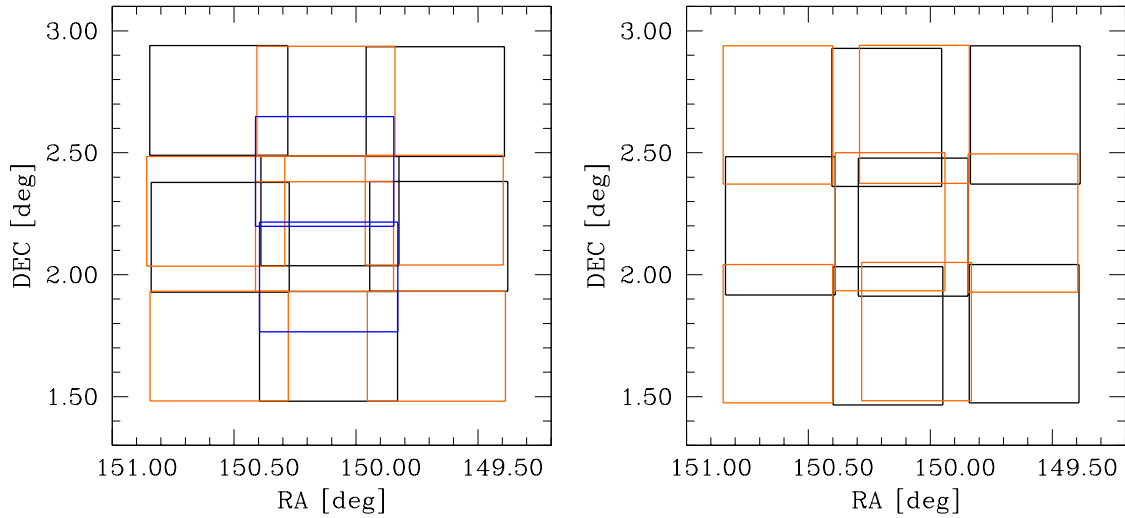
Figure 4.5: Sketch of the Subaru co-added exposures, totaling 26 pointings. The total area covered is 1.9 degrees^2. The left panel shows the pointings for which the camera was not rotated and the right panel shows the pointings for which the camera was rotated by 90 degrees. In the forthcoming lensing analysis, we have only used the two pointings represented in blue.

of 9×4 CCDs of 2048×4612 pixels each, with a pixel size is $0.186''$. The camera has a field of $1\,\text{degree}^2$. The CFHTLS was a 5-year project, which imaged the sky from spring 2003 to 2008. The project consisted of two surveys: the deep synoptic, covering $4\,\text{degrees}^2$, and wide synoptic survey, covering $170\,\text{degrees}^2$. The Deep survey has imaged four independent patches of the sky. The patch D2 is centered in the COSMOS field, covering $1\,\text{degrees}^2$ and it is used in this work. The data reduction is performed with the `GaBoDS/THELI` pipeline which
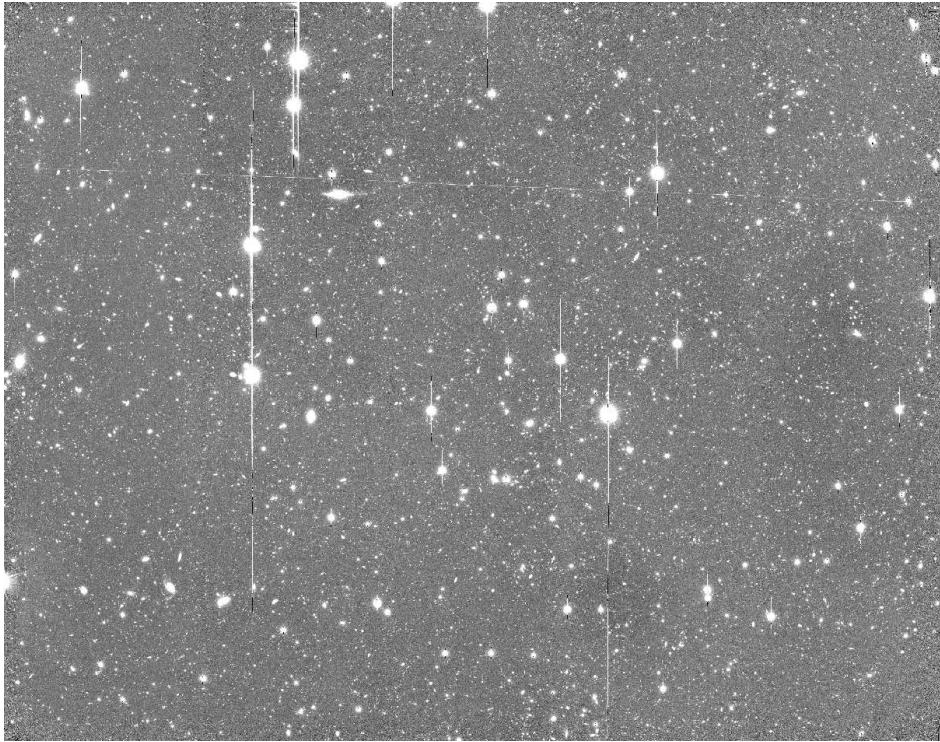
(a) Co-added image
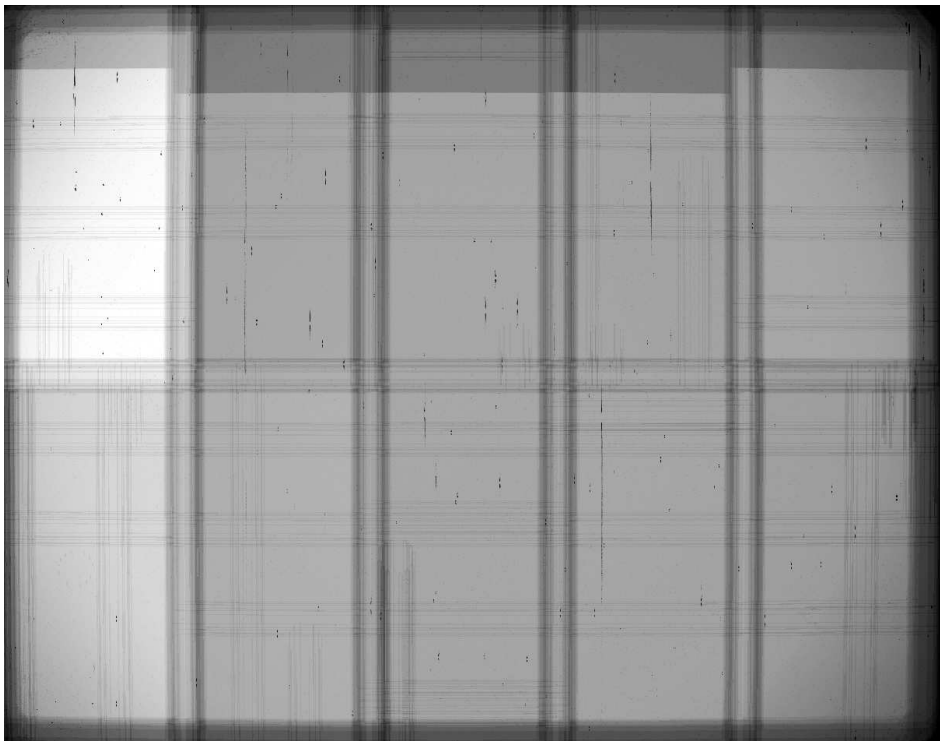
(b) Weight image

Figure 4.6: Final co-added image (top) and corresponding weight frame (bottom) for one of the Subaru pointings.
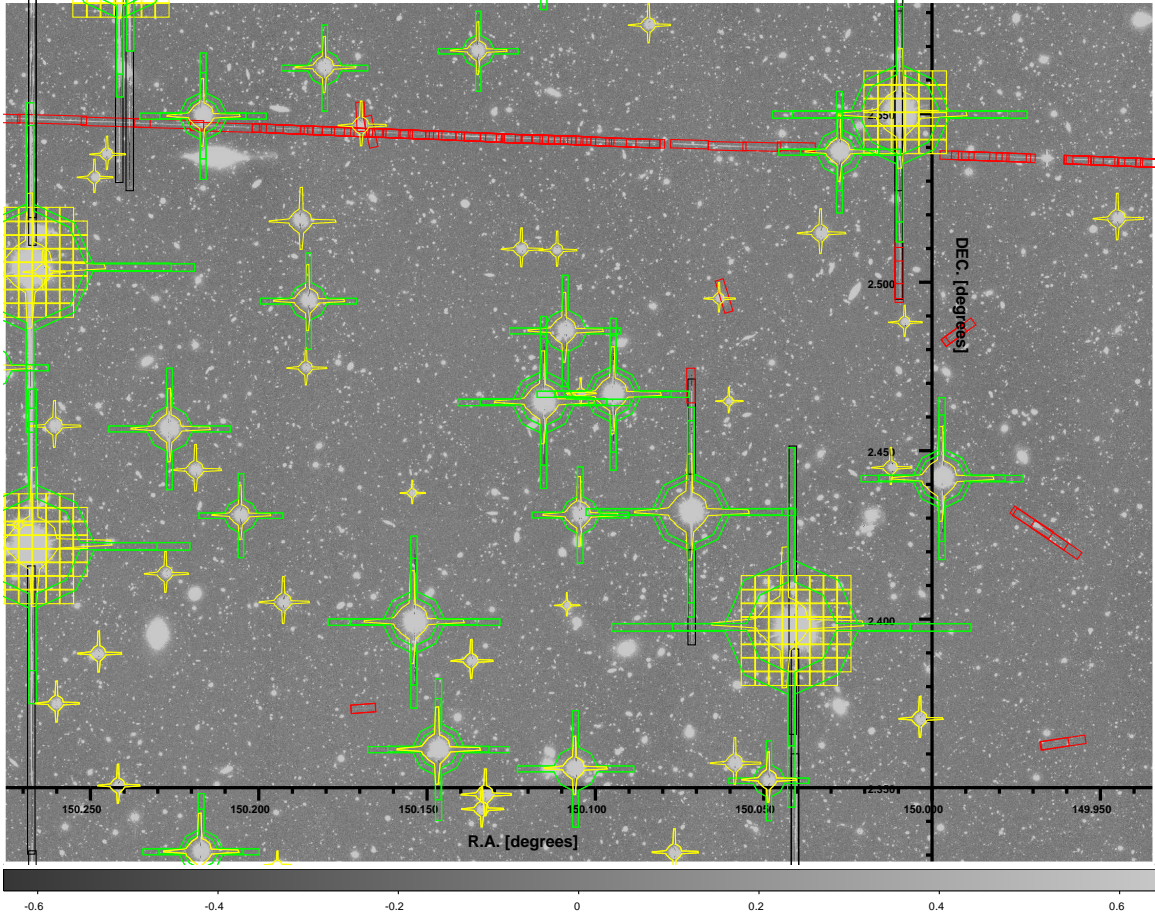
Figure 4.7: The Subaru i^+ band image and its corresponding masks. Red masks mark the asteroid tracks and pixels hit by cosmics. Green masks denote regions with bright stars. Yellow masks mark under-density halos around bright galaxies or stars. Black masks show the diffraction spikes.

is described in details in Erben et al. (2005, 2009) and Hildebrandt et al. (2007). We refer to these publications for further information.

We retrieve u^*, g', r', i' and z' bands data from the CFHT public archive[6] and process in a color basis. The archival data are already preprocessed, being corrected for bias and flat-field. Preprocessing also includes the removal of instrumental signatures from the raw data (such as bad and hot pixels) and removal of fringes in the case of i' and z' bands.

For each CCD chip a weight map containing information on noise properties is created. The weight maps are similar to the ones obtained for Subaru data and are used during the co-addition process. Furthermore, they are helpful to eliminate blended and corrupted detections of the source catalogs used in the astrometric calibration.

The astrometric solution is also obtained with SCAMP pipeline using the sixth data release of the Sloan Digital Sky Survey (SDSS-R6) as a reference catalog. The positional accuracy of the i' band data has an rms of $0.14''$ with respect to the SDSS-R6 catalog. Subaru i^+ band has an rms of the position deviation of $0.05''$ with respect to the CFHT i' image.

Photometric zero-points are derived for each color, bringing all individual images to the

---

[6]http://cadcwww.dao.nrc.ca/cadcbin/cfht/wdbi.cgi/cfht/quick/form

same flux scale. The images observed under photometric conditions had the zero-point corrected by the airmass.

After the astrometric and photometric calibration, the sky background is subtracted and the individual exposures are stacked using a weighted mean combination. The original image pixels are remapped using `SWarp` adopting a LANCZOS3 kernel. The final stacked images have the same pixel size as the original images $(0.186'')$. A weight map image containing the information on the noise properties of the final co-added image and a flag image carrying the information on the saturated pixels are also created. These final co-added images (and their weight and flag maps) are used to generate the multi-catalogs used to compute the photometric redshifts, described in Section 5.2 of Chapter 5.

We analyzed the impact on the PSF homogeneity by co-adding exposures taken during the three different CFHT MegaPrime configuration phases[7] separately. These epochs concern to the phases of investigations on the MegaPrime image quality. The first and second phase consist of data taken before and after November, 24th, 2004 when the lens L3 was accidentally mounted back upside-down. The mirror flipping brought a surprising improvement of the image quality. The third phase consists of the data taken after August, 12th, 2005, when a change in the height of the MegaPrime corrector was made. This final adjustment has improved the image quality in terms of homogeneity over the entire field-of-view. We found that, the stacked image produced using only exposures taken during the third phase of the instrument indeed yields in a more homogeneous PSF pattern, making the correction of stellar ellipticities easier (see Section 5.3 of Chapter 5). Thus, to carry out our lensing analysis, an extra stacked image of the i' band data was produced using only the exposures taken during CFHT MegaPrime phase three.

The same masking procedure adopted for the Subaru images are also applied to the CFHT images. When applying all masks there is a loss of $\sim 19\%$ of the total area. Figure 4.8 shows a region of the final i' band used in the lensing analysis and the corresponding masks.

Figure 4.9 shows a comparison of the Subaru data publicly available in the COSMOS archive, the Subaru reduced in this work and CFHT data.

---

[7]See: http://www.cfht.hawaii.edu/Science/CFHTLS-DATA/cfhtlsgeneralnews.html#0007.
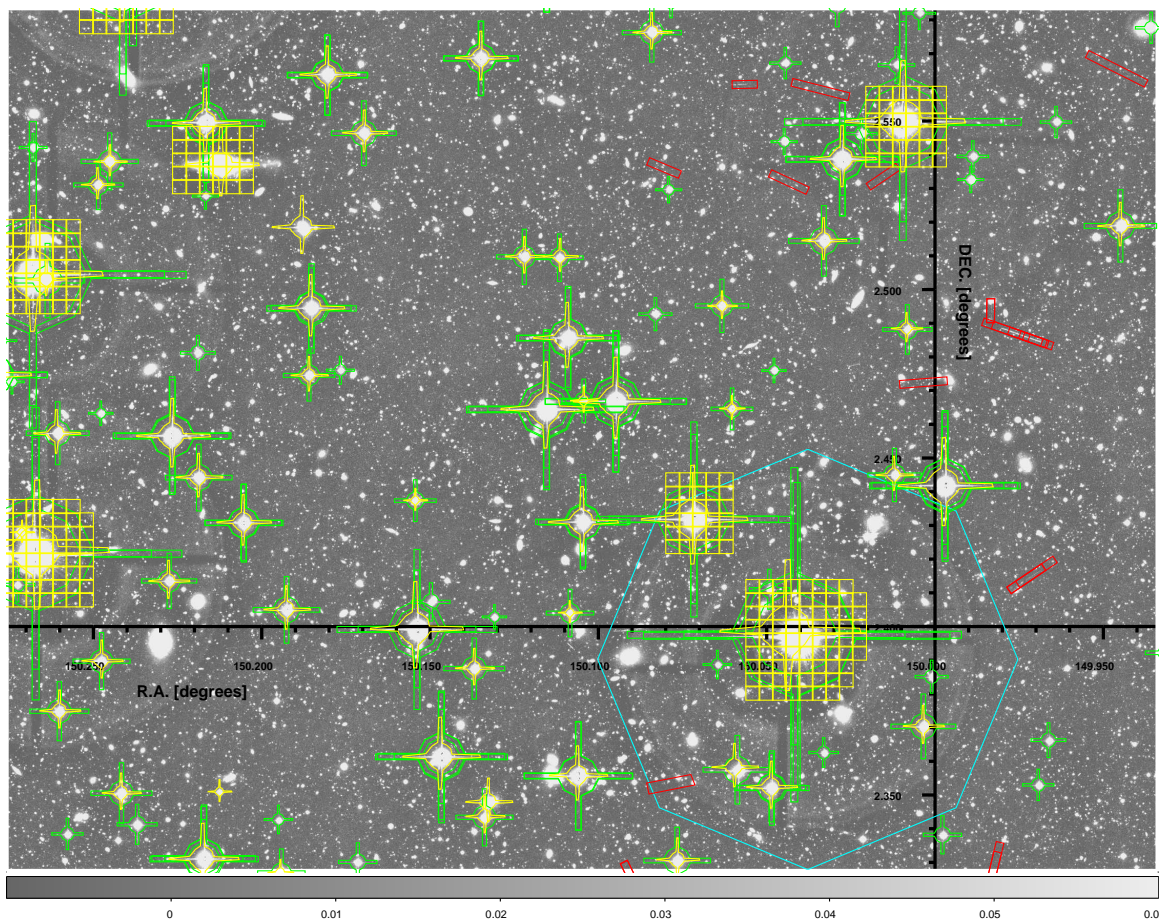
Figure 4.8: CFHT i' band image used in the lensing analysis (only with exposures taken during CFHT MegaPrime phase three are considered) and its corresponding masks. The color of the masks are the same for the Subaru data shown in Figure 4.7. CFHT MegaPrime instrument also exhibit some off-axis reflections. These regions are delimited by the cyan mask.

(a) Subaru matched PSF

(b) Subaru best PSF

(c) Subaru

(d) CFHT
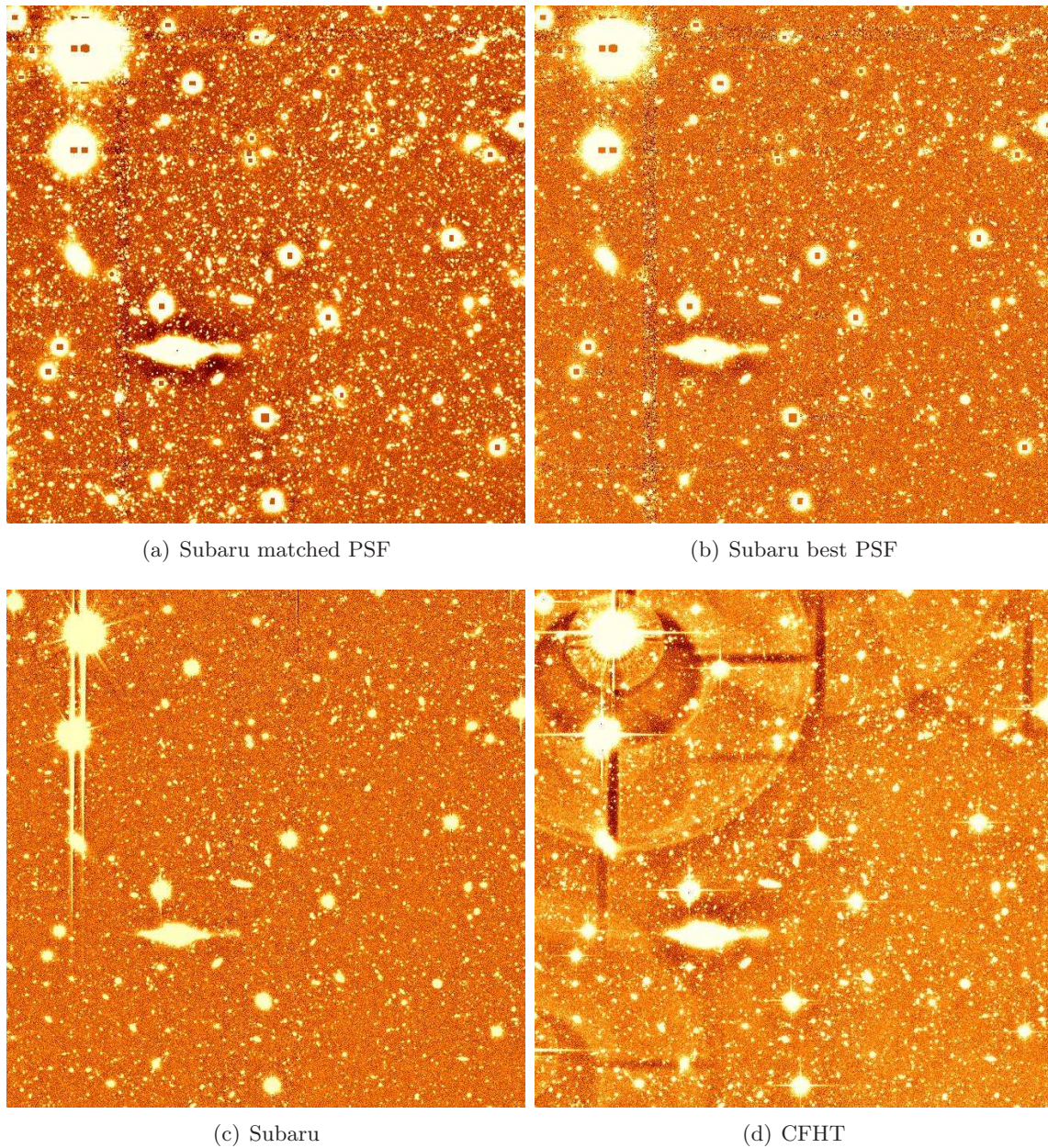
Figure 4.9: Comparison of four different data reductions of the same patch of the sky. The two top panels show the publicly available Subaru data, whereas the bottom panels shows the Subaru (left) and the CFHT data (right) reduced as described in the text. Subaru public images were convolved with a kernel of $1.6''$ (left) or had only exposures taken under extremely seeing conditions (seeing $< 0.5''$) co-added (right). The Subaru public data are deeper than ours because all individual exposures were stacked regardless of the dither pattern adopted. CFHT data achieved the same depth as the Subaru public data, but the large off-axis reflections of stars are problematic, because the affected regions need to be masked out.

Chapter 5

Observational Catalogs

I often think that the night is more alive
and more richly colored than the day.

Vincent Van Gogh

In this chapter, we describe the catalogs obtained from observations: in Section 5.1 we discuss the galaxy group selection from the analysis of the X-ray data, in Section 5.2 we present the photometric redshifts catalog (hereafter called photo-z) which is derived from multi-band optical data, and in Section 5.3 we discuss the shear catalogs, obtained from i' and i^+ data. A final observational catalog containing the positions, redshifts, shear estimates, and magnitudes of the field galaxies is created by combining the photo-z and shear catalogs. This information is subsequently used to create the shear mock catalogs, which are discussed in Chapter 6.

The photometric redshifts and the X-ray catalog used in this work were processed and provided in kind by Fabrice Brimoulle and Alexis Finoguenov, respectively.

We call the attention that the CFHT data cover an area of 1.0 degrees^2, which corresponds to the MegaPrime instrument field-of-view. For the Subaru data, since we only use individual exposures taken with the same camera orientation angle and offset $< 3'$, the resulting coverage is 0.55 degrees^2. Therefore, for the CFHT-like mock data, which will be introduced in Chapter 6, we restrict ourselves to 1.0 degrees^2 of data. For the Subaru-like mocks, we are restricted to 0.55 degrees^2.

5.1 X-rays: Galaxy Group Catalog

We use the COSMOS X-ray catalog of extended sources (Finoguenov et al., 2007, 2011 in preparation) to trace the distribution of the halos in the field. The catalog was obtained from a composite mosaic of the XMM-Newton and Chandra X-ray data and it is an update version of the X-ray catalog presented in Finoguenov et al. (2007). With the usage of both data sets, it was possible to detect and measure the flux of extended sources down to a limit[1]

---

[1]In fact, COSMOS X-ray data have an uniform depth of 10^{-15} erg cm^{-2} s^{-1}. However, in some areas, namely at the central parts, a depth of $4 - 6 \times 10^{-16}$ erg cm^{-2} s^{-1} is measured. The expected performance of the future X-ray mission eROSITA is 2×10^{-14} erg cm^{-2} s^{-1} on individual halos.

of 10^{-15} erg cm^{-2} s^{-1}. The catalog contains a total of 231 systems from $z_d = 0.07 - 1.84$. The derived properties of the systems are based on the X-ray scaling relations.

Halos Properties

The group/cluster candidates are identified through a wavelet detection of the extended X-ray emission.

The the observed X-ray flux F_d is computed using the total counts within the area defined by the detection algorithm, subtracting the contribution from the embedded active galactic nuclei (AGN) point-sources. Then, the total X-ray flux F_t is extrapolated from the measured F_d by assuming a β-profile (see Section 2.3.3 of Chapter 2) which is given by

$$F_t = C_\beta(z, T)\, F_d \tag{5.1}$$

where $C_\beta(z, T)$ is an iterative correction factor (see Finoguenov et al., 2007). Since the procedure that removes the flux from point-sources also removes flux from cool-cores, the total resulting flux is underestimated. Then, a method to compute a cool-core correction factor was developed and applied to flux estimates.

The apparent luminosity in the 0.1–2.4 keV band is calculated from the total flux via

$$L_{\mathrm{X(0.1-2.4keV)}} = 4\pi d_L^2\, C_\beta(z, T)\, F_d\,. \tag{5.2}$$

The rest-frame luminosity is obtained by divining $L_{\mathrm{X(0.1-2.4keV)}}$ by the K-correction factor $K_{corr}(z, T)$.

The temperature T is computed using the $L_{\mathrm{X(0.1-2.4keV)}} - T$ relation from Markevitch (1998)

$$k_B T = 6 \times 10^{\left[\log_{10}\left(L_{\mathrm{X(0.1-2.4keV)}} \times E(z)^{-1}\right) - 44.45\right]/2.1}\,\mathrm{keV} \tag{5.3}$$

where k_B is the Boltzmann's constant and $E(z)$ is given by equation (2.20).

The mass estimate is based on the self-similar scaling relation derived from the weak lensing analysis presented in Leauthaud et al. (2010), where

$$M_{200} \propto L_{\mathrm{X}}^\alpha \tag{5.4}$$

with a slope of $\alpha = 0.66 \pm 0.14$.

Redshifts of the X-ray systems are assigned by calculating the mean value of the photometric redshifts of the red sequence galaxies within the X-ray extended region. The photometric redshifts used were taken from Ilbert et al. (2009).

Selected Groups

All extended X-ray sources receive a quality flag. We select only objects with X-ray quality Flag=1–3. Flag 1 is a zone free of projections, which the significance of the X-ray detection is high. For these systems the center corresponds to the X-ray peak of the detection. Flag 2 systems are subject to contamination (mainly due to unresolved AGN), whose center corresponds to a weighted optical center of the system. The X-ray detections for which Flag 1 and 2 are assigned are spectroscopically confirmed systems. Flag 3 systems are similar to Flag 1 and 2 but without the spectroscopic confirmation. Selecting only Flags=1–3 and the X-ray detections that are in the CFHTLS-D2 field (1.0 degrees^2), our sample is comprised of 165 systems.
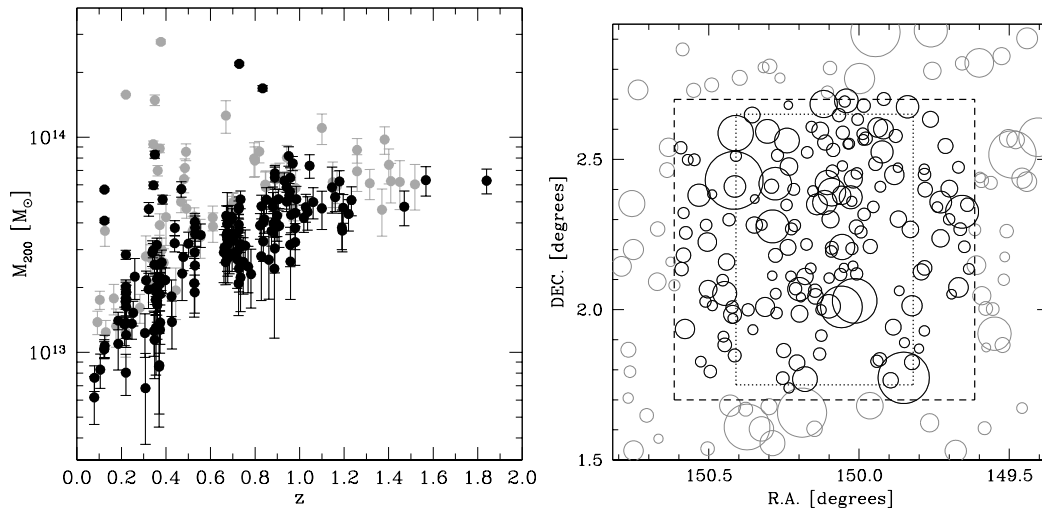
Figure 5.1: Left: Masses of the X-ray luminous halos as a function of redshift. The black points show the selected systems whereas the gray points show the other systems that are out of our field-of-view. Right: Positions of the X-ray detected halos in the COSMOS field. The black circles show the systems used in this work. The gray circles show the remaining detected systems in the COSMOS field which were excluded from our sample. The size of the circles gives the characteristic radius r_{200} of the groups. The inner dotted line delimits the Subaru FOV and the external dashed line delimits the CFHTLS-D2 FOV.

The selected galaxy groups have masses between $M = 0.6 - 21.9 \times 10^{13} \, \mathrm{M_\odot}$ with median mass of $M = 3.1 \times 10^{13} \, \mathrm{M_\odot}$. The groups are spread over the redshift range $z = 0.07 - 1.84$ with a median value of $z = 0.68$. Table A in the Appendix A provides information on the properties of the selected galaxy groups. The left panel of Figure 5.1 shows the mass M_{200} of the groups as a function of the redshift z. The right panel of Figure 5.1 shows the positions of the galaxy groups in the field-of-view.

Due to the high depth of the X-ray catalog, it is possible to detect a high number of groups and, therefore, they have a small angular separation between them. As we shall in what remains of this thesis, this is a problem for the weak lensing analysis of individual halos. Figure 5.2 shows the distribution of the distance to closest neighboring system θ_{close} seen in projection.

5.2 Multi-band Data: Photometric Redshift Catalog

Photometric redshifts are estimations of redshifts of galaxies by means of their photometric information, obtained from the observation in several passbands. With the photometric information, the spectrum emitted by galaxies can be reconstructed by fitting template spectra. From the known features of the spectrum (e.g. emission or absorption lines) the redshift of the galaxies can be inferred. Since this technique makes many assumptions about the emission nature of galaxies, it is subject to errors and, therefore, photometric redshifts are less accurate than spectroscopic redshifts. Nevertheless, this technique has been proved to be very valuable to obtain the redshift information of the hundreds of thousands of galaxies imaged in large surveys, that would otherwise be impossible to obtain spectra for all of them.

In order to estimate the photometric redshifts of galaxies, it is first necessary to detected
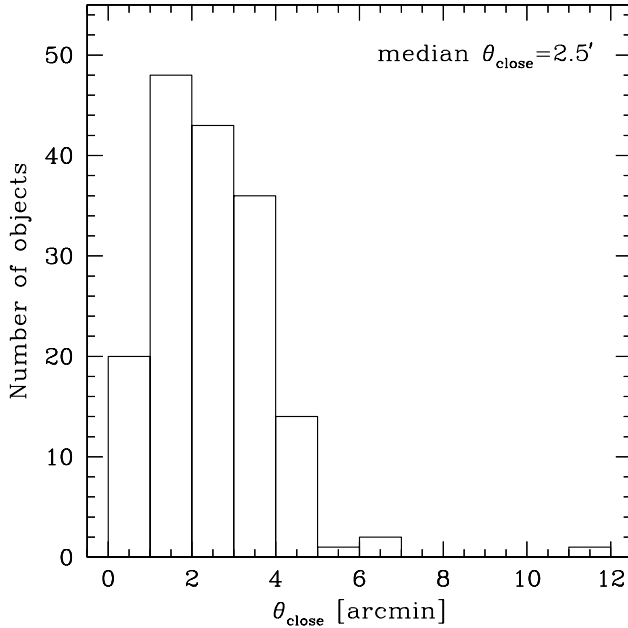
Figure 5.2: Distribution of the projected distance to the closest neighboring halo. Half of the sample has a secondary halo within $\theta_{\mathrm{close}} < 2.5'$.

the objects and estimate the flux of these objects within an aperture, using the same aperture size to all the observed bands. These *photometric catalogs* are thus used as input to the photo-z pipeline.

We create the photometric catalogs using the CFHT reduced images. In addition to the CFHT data, we also use H band imaged with the NIR wide-field camera OMEGA2000, operating at the prime focus of the CAHA 3.5 m telescope. We further use K_s band observed with KPNO 4 m telescope using the FLAMINGOS instrument and ISPI camera mounted on the CTIO 4 m telescope. Data from these instruments are combined to obtain a single K_s band image, which was retrieved from the COSMOS archive. Further details on the H band data can be found in Gabasch et al. (2008) and on the K_s band in Capak et al. (2007).

We measure the seeing in all bands and convolve them with a Gaussian kernel to match to the K_s band, which had the worst seeing ($1.5''$). Thus, we proceed to the creation of multi-color catalogs. In order to assure that the center of the objects are the same in all observed bands, objects are detected running `SExtractor` in dual-image mode on the unconvolved i' band image. The flux is measured within an aperture with diameter size of $1.86''$. Table 5.1 provides a summary of the data used to produce the photometric catalogs.

The photometric redshifts are computed in the same way as presented in Brimioulle et al. (2008), using the Bayesian `PHOTO-Z` code from Bender et al. (2001). Hereafter we provide a brief summary of the method.

The templates of the spectral energy distribution (SED) used are described in Bender et al. (2001) and Gabasch et al. (2004a,b). A total of 31 templates are used: 18 default templates plus 13 from Ilbert et al. (2006). The SED templates can be seen in the right panel of Figure 12 of Lerchster et al. (2011). For each SED template, the code computes the full redshift likelihood function. The step-size for the redshift grid is 0.01.

We compare the measured photo-z with the zCOSMOS sample of spectroscopic redshifts (Lilly et al., 2007). We retrieve redshifts for 2715 galaxies, spread over the area for which there was also H band. The accuracy of the photo-z is $\sigma_{\Delta z/(1+z)} = 0.031$, with a fraction of

catastrophic outliers of $\eta = 1.3\%$ and redshift scatter $\Delta z/(1+z) = 0.029$, where $\Delta z = |z_{\mathrm{spec}} - z_{\mathrm{phot}}|$. In the top panel of Figure 5.3 we show a comparison of the zCOSMOS spectroscopic redshifts to the ones computed in this work.

In order to get a catalog free of insecure photo-z estimates all the objects received a quality Flag. Stars, saturated objects and objects with high photo-z error have their Flag value greater than 3. We kept only objects with good photo-z quality Flags (Flag≤ 3). The meaning of these Flags can be found in Table A.1. of Brimioulle et al. (2008). The bottom panel of Figure 5.3 shows the distribution of the redshifts of our final catalog.

5.3 Weak Lensing: Shear Catalog

The weak lensing analysis consists in measuring the ellipticity of the galaxies observed in a data set, which as shown in Section 3.2.2 of Chapter 3, are directly related to the (reduced) shear. In order to perform this analysis, the pipeline takes an image as input and delivers as an output a catalog containing positions, the components of the ellipticity, error of the measurements and other properties of the detected galaxies.

The primary goal of our weak lensing analysis is to obtain a realistic density and distribution of galaxies for the COSMOS field. This is important because the shear pipelines tend to discard many of the detected objects, either because they are too bright to be considered as background sources, either because they are too faint and noisy that shape measurements fail. As a secondary goal, we want to compare the results obtained from observations with the results obtained from the shear mock catalogs (see Chapter 6) whenever it is possible.

The shear catalogs are obtained using the KSB pipeline, introduced by Kaiser, Squires and Broadhurst in 1995 and subsequently improved by Luppino & Kaiser (1997) and Hoekstra et al. (1998). The KSB version used in this work (also called KSB+) is described in detail in Erben et al. (2001) and Schrabback et al. (2007). In this section we summarize the method focusing on the subtle choices made to create our shear catalogs. An extended description of this method can be found in the review from Bartelmann & Schneider (2001).

The detection of sources is performed with SExtractor, using the i' and i^+ wavelength bands. The weight and flag maps of the final stacked images are used to detect the objects. This allows a more precise evaluation of the signal-to-noise ratio of the detected objects. The detection threshold chosen is 1.6. Only objects with a minimum of 4 pixels with signal-to-noise ratio above the established threshold are considered valid.

For each extracted object, SExtractor computes the second moments of the surface

Filter	EXP_TIME	Seeing
u^*	6.9 h	$0.95''$
g'	9.3 h	$0.85''$
r'	25.5 h	$0.74''$
i'	53 h	$0.73''$
z'	14.1 h	$0.71''$
H	0.80 h	$1.08''$
K_s	0.84 h	$1.50''$

Table 5.1: Summary of the data used to compute the photometric redshifts.

$N_{gal} = 2715$

$\eta = 1.3~\%$

$\sigma_{\Delta z/(1+z_{spec})} = 0.031$

$\Delta z/(1+z) = 0.029$
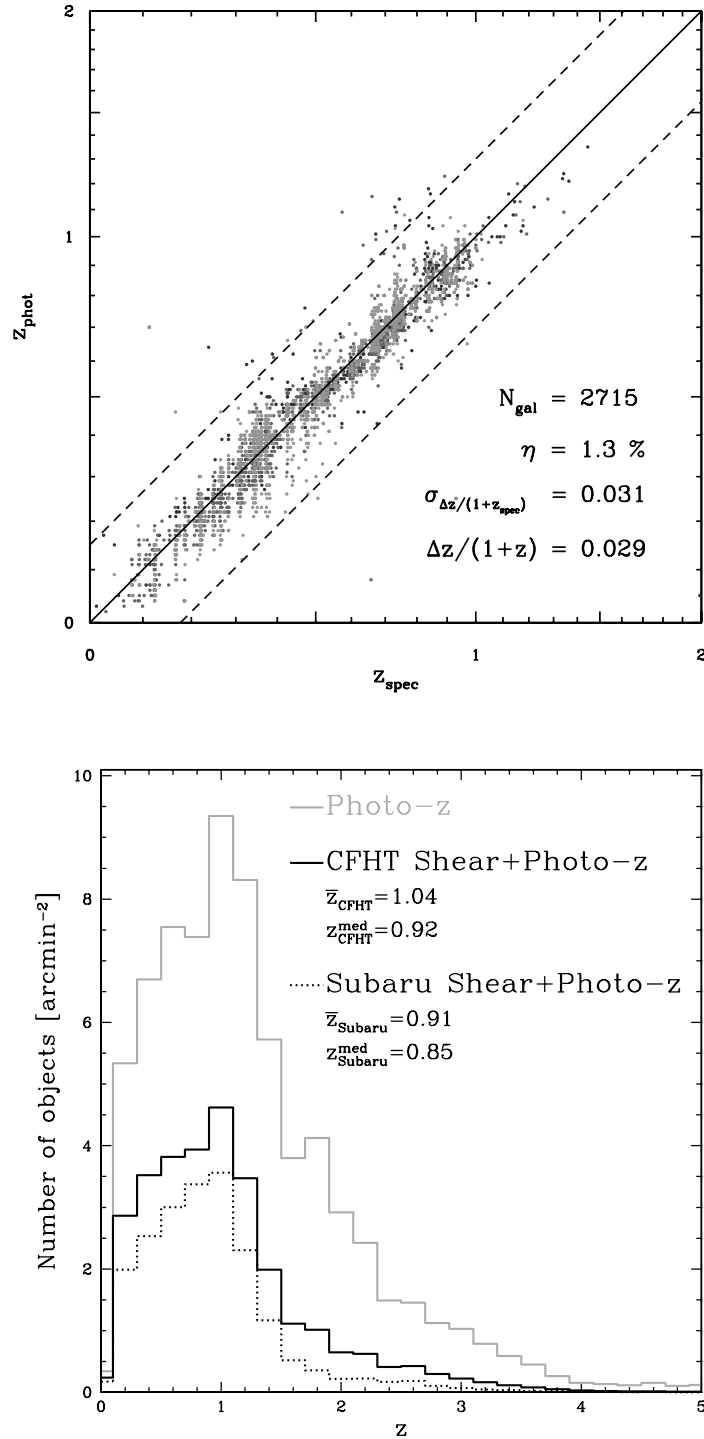
Figure 5.3: Top: photometric redshifts of non-stellar objects against spectroscopic redshifts from the zCOSMOS sample. Dotted lines are for $z_{phot} = z_{spec} \pm 0.15 \times (1 + z_{spec})$. The fraction η of catastrophic outliers is defined as a fraction of galaxies for which $|z_{spec} - z_{phot}|/(1 + z_{spec}) > 0.15$ holds. Bottom: Distribution of the computed photometric redshifts. The gray solid histogram shows the distribution for all the objects with photometric redshifts. The black solid histogram shows the redshift distribution of the redshifts of the galaxies in the final CFHT catalog (shear plus photo-z) and black dashed histogram shows the same but for the Subaru final catalog.

brightness distribution $Q_{\alpha\beta}$, which were introduced in equation (3.28). We use a Gaussian filter function, with a window r_g equal to the half-light radius r_h of the detected objects.

From the second moments of the surface brightness distribution $Q_{\alpha\beta}$, the observed ellipticity is derived according to equation (3.31), so that

$$
\begin{aligned}
\mathbf{e}^{\mathrm{obs}} &= \frac{Q_{11} - Q_{22} + 2\mathrm{i}\, Q_{12}}{Q_{11} + Q_{22}} \\
&= e_1 + \mathrm{i}\, e_2 \,.
\end{aligned}
\tag{5.5}
$$

Because the light distribution of the measured objects pass through the telescope (and atmosphere in the case of ground-based facilities), the observed ellipticity is a combination of several factors: intrinsic ellipticity, PSF shearing, PSF anisotropy and gravitational lensing. The KSB approach assumes that the PSF can be described as an anisotropic contribution convolved with an isotropic kernel that mimics the seeing (assumed to be circularly symmetric), thus each component of the observed ellipticity can be split as

$$
e_{\alpha}^{\mathrm{obs}} = e_{\alpha}^{\mathrm{s}} + P_{\alpha\beta}^{\mathrm{g}} g_{\beta} + P_{\alpha\beta}^{\mathrm{sm}} q_{\beta} \,, \quad \alpha, \beta \in \{1, 2\} \,,
\tag{5.6}
$$

where q is the term that accounts for the PSF anisotropy, P^{sm} is the smear polarizability calculated from the galaxy brightness distribution and the Gaussian weight function and g is the pre-seeing gravitational (reduced) shear. The factor P^{g} is the pre-seeing shear polarizability which is calculated as

$$
P^{\mathrm{g}} = P^{\mathrm{sh}} - P^{\mathrm{sm}} \frac{P^{\mathrm{sh}*}}{P^{\mathrm{sm}*}}
\tag{5.7}
$$

where P^{sh} is the shear polarizability tensor and the asterisk * denotes quantities measured from stars. P^{sh} can be interpreted as the response of the galaxy ellipticities to gravitation if there are no PSF effects.

Since stars are intrinsically round $e_{\alpha}^{\mathrm{s}*} = 0$, and since their shapes are not gravitationally distorted $g_{\alpha}^{*} = 0$, thus the equation (5.6) yields

$$
q_{\beta} = q_{\beta}^{*} = (P^{\mathrm{sm}*})_{\alpha\beta}^{-1} e_{\alpha}^{\mathrm{obs}*} \,.
\tag{5.8}
$$

The spatial variation of q across the field-of-view is usually well described by a polynomial function. The detected stars are used to model the PSF anisotropy across the field, including at the position of galaxies. Since the catalog of the detected objects processed by KSB contains both stars and galaxies, stars are selected by visual inspection of the mag-r_h diagram as illustrated in Figure 5.4. This way to select star is possible because stars occupy a very specific position in this diagnostic plot: stars have a constant size given by the width of the PSF.

For the CFHT catalog, stars are selected in the range of $0.35'' < r_h < 0.43''$ and $17.9 < \mathrm{mag} < 21.5$. We also exclude the stars close to CCD borders yielding ~ 2100 stars used to fit a polynomial function of order 5 (cf. left column of Figure 5.6). For the Subaru data the PSF modeling was more complicated than for CFHT, because the pattern varies discontinuously across the field-of-view (cf. middle column of Figure 5.6). We found that a polynomial function could not model proper the PSF across the entire field. Thus, we perform the correction on a chip basis, where only stars belonging to the region imaged by one CCD chip are used. Subaru stars are then selected in the range of $0.28'' \lesssim r_h \lesssim 0.36''$ and $19.8 \lesssim \mathrm{mag} \lesssim 21.7$, yielding on average ~ 72 stars per chip with a minimum of 56 and a
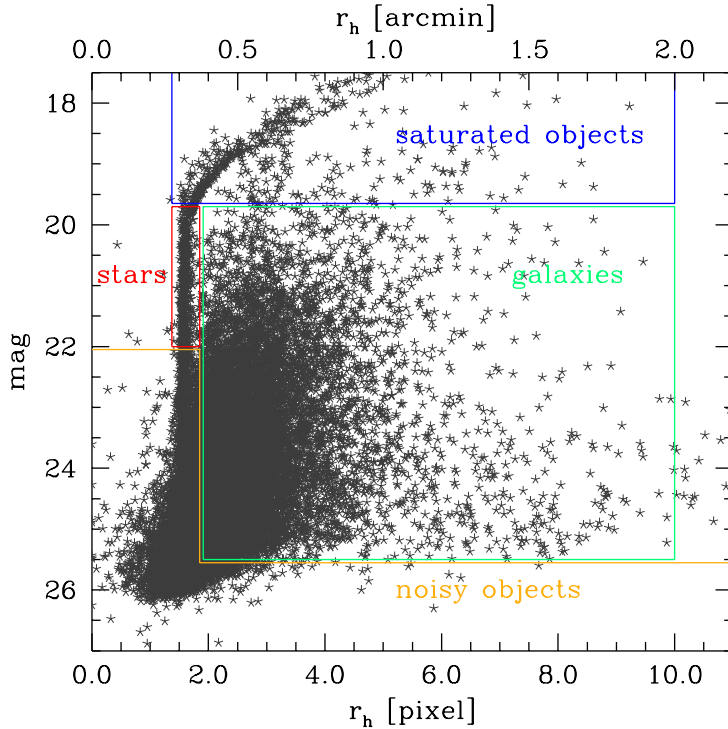
Figure 5.4: Stars can be selected from the visual inspection of the mag-r_h diagram, since they occupy a very specific location in this plot. Potential stars for the PSF modeling are those located in the region delimited by red. Galaxies used in the weak lensing analysis are the objects within the region delimited by green. Other objects are eventually discarded because either they are saturated (blue region) or they are too faint and noisy (yellow region). This plot is obtained using the objects detected in the Subaru i^+ band.

maximum of 87 stars. Yet, the diagnostic plots (like the ones shown in Figure 5.5) were not sufficient to justify which was the best polynomial order to fit Subaru data. Thus, we make use of the diagnostic proposed by Rowe (2010) to help in the identification of the optimal polynomial order. We find that polynomial order 3 underfits the data whereas order 5 overfits, though there is a variation with the Gaussian window r_g used to measure stellar quantities. We conclude that a polynomial order of 4 yields the best performance.

Eventually, after the PSF modeling, the observed ellipticities are corrected by calculating

$$e_\alpha^{\mathrm{corr}} = e_\alpha^{\mathrm{obs}} - P_{\alpha\beta}^{\mathrm{sm}*} q_\beta^*. \tag{5.9}$$

Figure 5.5 shows the ellipticity components of stars before and after the correction for PSF anisotropy. For the CFHT, the PSF model is excellent, with a stellar ellipticity dispersion of $\sigma_{e_i^{\mathrm{corr}*}} \sim 0.0028$ per each component. For the Subaru data, the residual ellipticities have a higher but satisfactory dispersion of $\sigma_{e_i^{\mathrm{corr}*}} \sim 0.0057$. Figure 5.6 shows a visual impression of the stellar ellipticities across the field-of-view for CFHT data (left column), Subaru data (middle column) and Subaru-COSMOS best-psf archival data (right column), which were introduced in Section 4.2 of Chapter 4. For the three data sets, we plot the observed ellipticities (top row) of the stars used to fit the PSF model, the ellipticities of the best-fit model (middle row) and the final corrected or residual ellipticities (bottom row). It is worth noting that different data sets cover different areas, but the scale of an object with $|\mathbf{e}| = 0.1$ is always shown in each panel. The CFHT data show some gaps because stars lying close to CCD borders were excluded. The Subaru data reduced for this work shows a complex observed PSF pattern across the field-of-view, but for which a model can be computed. The Subaru archival data exhibit a chaotic PSF pattern due to the co-addition strategy, which it turns out too difficult to be modeled.
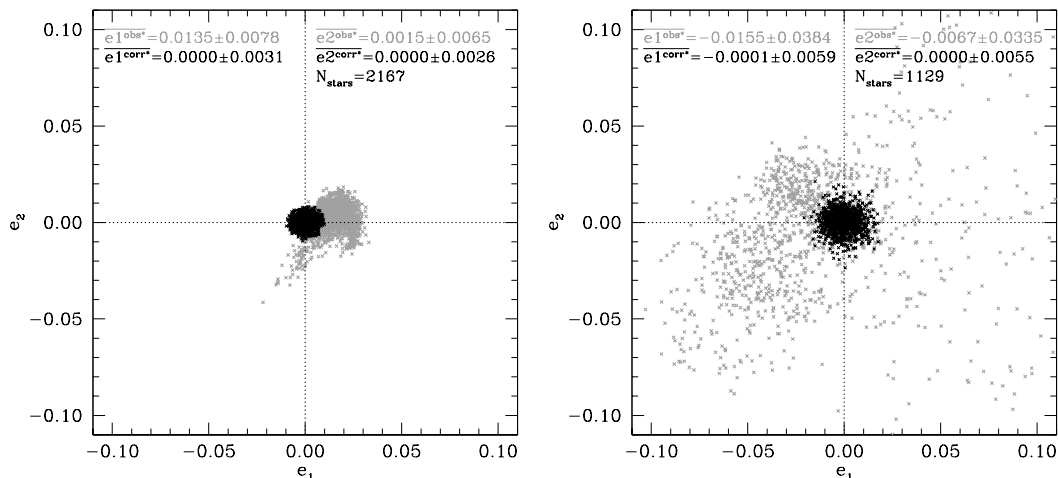
Figure 5.5: Observed ellipticity components (gray dots) and corrected values (black dots) after the PSF model subtraction. The left panel shows the CFHT data for which the entire FOV is modeled with a polynomial function of order 5. The right panel shows the same but for the Subaru data. For Subaru, the PSF is modeled in a chip-wise basis using a polynomial order of 4. The plotted quantities are measured with a Gaussian window of $r_g = 3 \times r_h$.

Since the stars are used to predict the PSF anisotropy at the position of the galaxies, it is important to transfer the stellar quantities to the galaxies measured with the same Gaussian window (Hoekstra et al., 1998). Then, after the PSF modeling, the KSB pipeline computes stellar quantities again but using several sizes of Gaussian windows. According to the size of the galaxies, the correct stellar quantity to be transferred is the one measured with a compatible Gaussian window.

Eventually, since $\langle \mathbf{e} \rangle / 2 = \mathbf{g}$, thus

$$\langle g_\alpha \rangle = \langle (P^{\mathrm{g}})^{-1}_{\alpha\beta} e^{\mathrm{corr}}_\alpha \rangle \tag{5.10}$$

is an unbiased estimate for the reduced gravitational shear at the galaxy positions. Hereafter we will also assume $\mathbf{g} \simeq \boldsymbol{\gamma}$ since $\kappa \ll 1$.

According to Schrabback et al. (2007) the KSB+ implementation requires, on average, calibration factor of $c_{cal} = 1/0.91$ so that $\langle \gamma_\alpha \rangle = \langle e_\alpha \rangle / 0.91$. This calibration factor was derived from STEP1 simulations (Heymans et al., 2006).

We apply a final cut in the catalog to select only galaxies with relative high signal-to-noise ratio. For the CFHT data we follow the criteria: signal-to-noise of the detection $\nu > 5$, $17.9 < \mathrm{mag} < 26$, $r_h > 0.43''$ and $|\mathbf{e}| < 1$. The final catalog has density of galaxies $n_{shear} = 32.8$ galaxies arcmin^{-2}. For the Subaru data the criteria is similar: signal-to-noise of the detection $\nu > 5$, $19.7 < \mathrm{mag} < 25$, $r_h > 0.37''$ and $|\mathbf{e}| < 1$, resulting in a catalog with density of $n_{shear} \sim 23.7$ galaxies arcmin^{-2}.

We match the CFHT shear and photo-z catalogs, producing a final catalog with a density of $n_{eff} = 29.7$ galaxies arcmin^{-2}, mean redshift of $\bar{z} = 1.04$ and two-component ellipticity dispersion of galaxies of $\sigma_{\mathbf{e}^s} = 0.47$. For the Subaru, the shear plus photo-z final catalog has $n_{eff} = 21.7$ galaxies arcmin^{-2}, mean redshift of $\bar{z} = 0.91$ and two-component ellipticity dispersion of galaxies of $\sigma_{\mathbf{e}^s} = 0.42$. Hereafter we call these catalogs *shear-photo-z*. The values of the ellipticity dispersion of both CFHT and Subaru data are in agreement
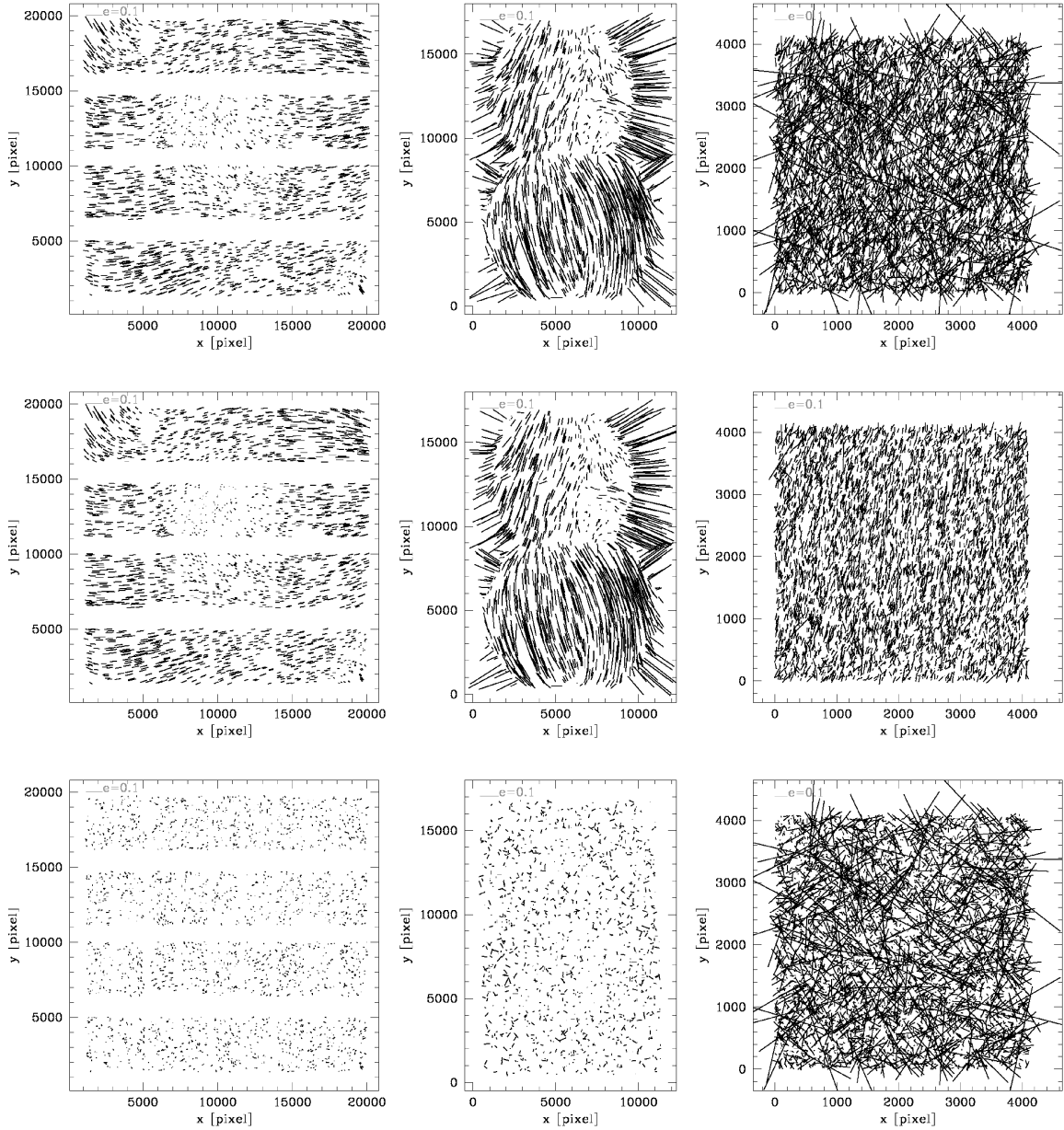
Figure 5.6: Visual impression of the observed (top row), modeled (middle row) and residual (bottom row) ellipticities of stars. Each stick represents a star in the field used to model the PSF pattern. The size and the orientation of the sticks give the strength and the direction of the distortion introduced by the telescope optics and atmosphere. The scale of an object with $|e| = 0.1$ is shown in each panel. The left column shows the CFHT data, the middle column shows the Subaru data, and the right column shows the Subaru archival data. The plotted quantities are measured with a Gaussian window of $r_g = 3 \times r_h$. See the text for more details.

with values previously found in the literature (e.g. Schirmer et al., 2007; Umetsu et al., 2010; Schrabback et al., 2010). Table 5.2 summarizes the properties of the derived shear catalogs and compares with previously published results on shear measurements in the COSMOS field.

Telescope (1)	$\sigma_{e_1^{res*}}$ (2)	$\sigma_{e_2^{res*}}$ (3)	n_{det} (4)	n_{shear} (5)	n_{eff} (6)	$\sigma_{e_1^s}$ (7)	$\sigma_{e_2^s}$ (8)	$\sigma_{\mathbf{e}^s}$ (9)	$\bar{z}$ (10)	z^{med} (11)	Ref. (12)
CFHT	0.0031[c]	0.0026[c]	52.3	32.8	29.7	0.33[b]	0.34[b]	0.47[b]	1.04[b]	0.92[b]	This work
Subaru	0.0059[c]	0.0055[c]	40.3	23.7	21.7	0.30[b]	0.30[b]	0.42[b]	0.91[b]	0.85[b]	This work
CFHT	0.0040[d]	0.0040[d]		30.6		~0.23[f]	~0.233[f]	0.333[f]	0.92		G07
HST			71.0								K08
HST				66.0	34.0	~0.273[a]	~0.27[a]	0.38[a]	1.0[b]		L07, L10
HST				80.0	76.0[e]	~0.31[b]	~0.31[b]	0.44[b]			S10
Subaru				37.1							M07
Subaru			42.0								K08
Subaru				42.0							B11, M07

Table 5.2: Summary of the lensing catalogs computed in this work and the previously published catalogs of the COSMOS field. Columns (1): Telescope; (2) and (3): one-component dispersion of the stellar ellipticities after the PSF correction; (4) number of detected galaxies per arcmin^2; (5) number of galaxies per arcmin^2 in the shear catalog; (6) number of galaxies per arcmin^2 in the shear-photo-z matched catalog; (7) and (8): one-component ellipticity dispersion of galaxies; (9): two-component ellipticity dispersion of galaxies, which is defined as $\sigma_{\mathbf{e}^s}^2 = \sigma_{e_1^s}^2 + \sigma_{e_2^s}^2$; (10): mean redshift; (11): median redshift; (12): References. G07: Gavazzi & Soucail (2007); K08: Kasliwal et al. (2008); L07: Leauthaud et al. (2007); L10: Leauthaud et al. (2010); S10: Schrabback et al. (2010); M07: Miyazaki et al. (2007); K08: Kasliwal et al. (2008); B11: Bellagamba et al. (2011).

[a] Quantity measured using the shear catalog.
[b] Quantity measured using the shear-photo-z matched catalog.
[c] Quantity measured using a Gaussian window of $r_g = 3 \times r_h$.
[d] Unknown Gaussian window size used to measure the quantity.
[e] Real photo-z catalog with density of ~ 30 galaxies arcmin^{-2} was used. The distribution of the photo-z was used to estimate the redshifts of the remaining galaxies.
[f] Quantity measured using observed dispersion of ellipticities over the 40 nearest neighbors in the r_h-mag plane.

Chapter 6

Shear Mock Catalogs

In this chapter we describe how the shear mock catalogs are derived using the information obtained from the data catalogs described in Chapter 5.

In order to create shear mock catalogs, we use the position and the number of galaxies from the shear-photo-z catalogs. This means that galaxies are placed on the exact same positions as in the CFHT i' and Subaru i^+ band data. Redshifts of the galaxies in the mock catalogs are the same as the computed photo-z. The distribution of the galaxy groups and their masses are taken from the X-ray catalog. We call the attention that the simulations could have been set without the need of obtaining a shear and photo-z catalog. Simulations could have set, for instance, using a known redshift distribution and by assigning random positions to the galaxies. However, we opt for obtaining the shear and photo-z catalogs because current pipelines used to estimate these quantities tend to suppress the observed density of galaxies. This is specially true for the shear pipelines, for which shape measurements fail for certain types of galaxies, or for galaxies lying close to bright stars. Obtaining the shear and the photo-z catalogs guarantees a more realistic density distribution of galaxies as well as a direct comparison with results obtained from the observational catalogs.

As shown in equation (3.14), calculating the shear distortion imprinted by a halo in the shape of a background galaxy implies that the lensing potential is known. Therefore we need a mass model that describes the halo. Numerical studies performed by Navarro, Frenk, & White (1997) using CDM cosmology have shown that halos collapse to a nearly universal form, which on average, are spherically symmetric. The so-called NFW density profile is given by

$$\rho(r) = \frac{\delta_c \rho_{crit}}{\frac{r}{r_s}\left(1 + \frac{r}{r_s}\right)^2} \tag{6.1}$$

where $\delta_c \rho_{crit}$ and the scale radius r_s are parameters which vary from halo to halo. Since the total mass obtained from an NFW profile is divergent, it is useful to define the edge of the halo as the virial radius r_{vir}, which is related to the *concentration parameter c* and the *scale radius r_s* via $r_{vir} = c\, r_s$.

The NFW profile has its pros and cons. In the first place, the corresponding circular velocity profile is nearly flat, but it slowly decreases as $r \to \infty$. This characteristic is in agreement with the observed rotation curves of spiral galaxies (e.g. Sofue & Rubin, 2001; Klypin et al., 2002). Secondly, the NFW profile has a steep central cusp. However such

a cuspy profile does not explain the rotation curves of dwarf galaxies, which rise slowly as $r \to \infty$ (e.g. Salucci & Burkert, 2000; de Blok et al., 2001).

Assuming that each galaxy group in our sample acts as a lens, we calculate the shear imposed by each lens on each background galaxy. The mass distribution of an isolated lens is thus described by an NFW density profile, where ρ_{crit} is the critical density of the Universe at the redshift of the lens z_d calculated using equation (2.12). The Hubble's parameter $H(z_d)$ of equation (2.12) is calculated according to equation (2.19) also at the redshift of the lens. Depending on the mass definition used, the scale radius r_s can be expressed in other combinations of the concentration c and the radius which characterizes the edge of the halo. We have used the definition in which the mass density is equal $\rho = 200\rho_{crit}$. Therefore $c_{200} = r_{200}/r_s$, and $M_{200} \equiv M(r_{200})$, so that

$$M_{200} = 200\rho_{crit}\frac{4\pi}{3}r_{200}^3 \,. \tag{6.2}$$

The density contrast $\delta_c \equiv \delta_{c_{200}}$ of equation (6.1) is thus defined as

$$\delta_{c_{200}} = \frac{200}{3}\frac{c_{200}^3}{\ln(1 + c_{200}) - \frac{c_{200}}{(1+c_{200})}} \,. \tag{6.3}$$

The concentration of each galaxy group is calculated using a $c_{200}(M_{200}, z_d)$ relation presented in Duffy et al. (2008)

$$c_{200} = \frac{5.71}{(1 + z_d)^{0.47}} \times \left(\frac{M_{200}}{2.0 \times 10^{12}\,h^{-1}\mathrm{M}_\odot}\right)^{-0.084} \,, \tag{6.4}$$

with $h = 0.72$. This relation was measured from N-body simulations assuming WMAP5 cosmology and the same M_{200} mass definition as we use in this work. This $c_{200}(M_{200}, z_d)$ relation was found as the best fit for all halos in the simulation (relaxed and unrelaxed) between $z_d = 0 - 2$. The left panel of Figure 6.1 shows the concentration c_{200} as a function of redshift z_d for the galaxy groups in our sample. The concentration values span from $2.7 - 5.1$. The right panel of Figure 6.1 shows the shear profile of a group with $M_{200} = 2.5 \times 10^{13}\,\mathrm{M}_\odot$ located at $z_d = 0.30$, but for which different concentration values are arbitrarily assumed. As we can see from this figure, the value of the concentration changes the steepness of the shear profile in the innermost regions.

Gravitational lensing measures the projected mass inside of a disk of radius $R^2 = r^2 - z^2$, which in angular units is defined as $R = \theta \times D_d$ (see the definition of angular distance given by equation 2.22). The analytic expression for the shear of a lens characterized by an NFW density profile as a function of a dimensionless radius $x = R/r_s$, is given by Bartelmann
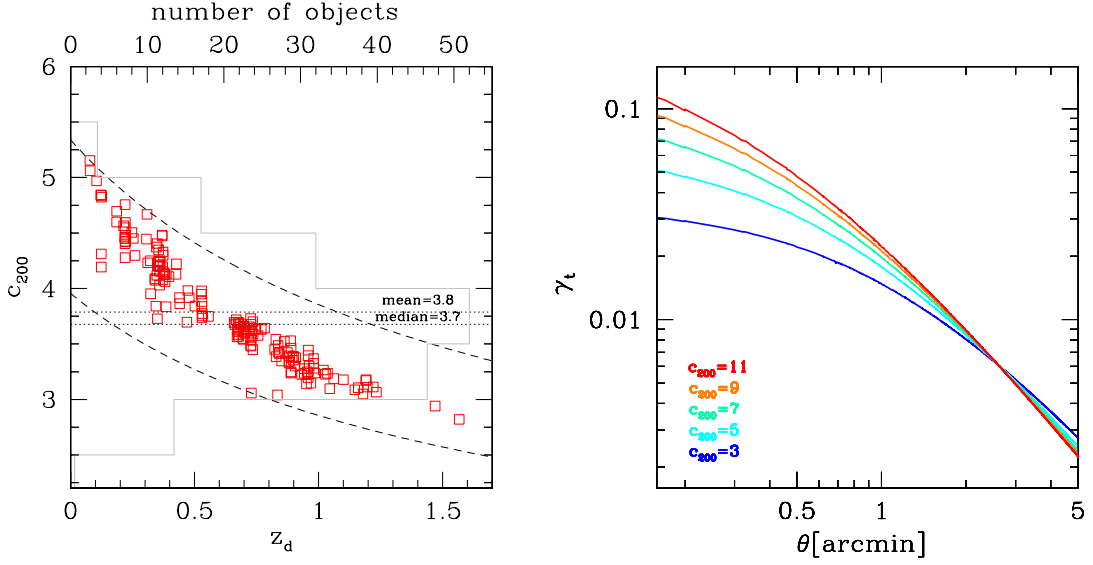
Figure 6.1: On the left panel, the red squares show the concentration c_{200} of the galaxy groups as function of redshift z_d. Dashed lines delimit the lower and upper limits for our sample. The horizontal gray histogram is the distribution of the concentration where the number of objects in each bin is indicated by the upper axis. On the right panel, the tangential shear profile of a group with $M_{200} = 2.5 \times 10^{13}$ M$_\odot$ at $z_d = 0.30$ is shown, where colors represent the profile for different concentration values.

(1996) and Wright & Brainerd (2000):

$$\gamma(x) = \begin{cases} \frac{r_s \delta_c \rho_{crit}}{\Sigma_{crit}} \left[\frac{8 \operatorname{atanh}\sqrt{(1-x)/(1+x)}}{x^2\sqrt{1-x^2}} + \right. \\ \left. \frac{4}{x^2}\ln\left(\frac{x}{2}\right) - \frac{2}{(x^2-1)} + \frac{4\operatorname{atanh}\sqrt{(1-x)/(1+x)}}{(x^2-1)(1-x^2)^{1/2}} \right] & \text{if} \quad x < 1\,, \\[2ex] \frac{r_s \delta_c \rho_{crit}}{\Sigma_{crit}} \left[\frac{10}{3} + 4\ln\left(\frac{1}{2}\right) \right] & \text{if} \quad x = 1\,, \\[2ex] \frac{r_s \delta_c \rho_{crit}}{\Sigma_{crit}} \left[\frac{8 \arctan\sqrt{(x-1)/(1+x)}}{x^2\sqrt{x^2-1}} + \right. \\ \left. \frac{4}{x^2}\ln\left(\frac{x}{2}\right) - \frac{2}{(x^2-1)} + \frac{4\arctan\sqrt{(x-1)/(1+x)}}{(x^2-1)^{3/2}} \right] & \text{if} \quad x > 1 \end{cases} \qquad (6.5)$$

where Σ_{crit} is the critical surface mass density calculated according to equation (3.12).

The prediction for each shear component γ_1 and γ_2 for a circularly symmetric distribution is given by

$$\gamma_1 = \gamma \frac{\theta_2^2 - \theta_1^2}{|\boldsymbol{\theta}|^2} \quad \text{and} \quad \gamma_2 = -\gamma \frac{2\theta_1 \theta_2}{|\boldsymbol{\theta}|^2}\,, \qquad (6.6)$$

where θ_1 and θ_2 are the components of the angular position $\boldsymbol{\theta}$ of the source galaxy relative to the halo (see Figure 3.6).

With the above set of equations it is possible to calculate the shear imposed by each lens on each background galaxy. Thus, for all galaxy groups in our sample, a shear mock catalog is generated, assuming that the groups are isolated in the sky. Field galaxies with redshift

smaller than the redshift of the lens had their shear value set to zero. Hereafter, we call these catalogs *isolated-pure-shear*, which are in total 165, each one of them corresponding to one galaxy group of the sample. The "pure-shear" refers to the fact that galaxy shape noise is not included at this point.

In reality, groups are not isolated but immersed in the field and what is measured is the shear caused by all lenses. The total shear of the j-th galaxy is thus calculated by summing the shear over all the lenses/groups

$$\boldsymbol{\gamma}_{\mathrm{total}_j}(\boldsymbol{\theta}) = \sum_{j=1}^{N_{\mathrm{Lens}}=165} (\gamma_{1_j} + \mathrm{i}\,\gamma_{2_j}). \tag{6.7}$$

From this point on, we call this catalog *multiple-lens-pure-shear*. For each data set (CFHT and Subaru), isolated-pure-shear catalogs and a multiple-lens-pure-shear catalog are generated.

Finally, the intrinsic ellipticity of galaxies has to be taken into account. The observed shape of the j-th galaxy is given by the sum of the intrinsic ellipticity $\mathbf{e}_j^s$ and the induced shear $\boldsymbol{\gamma}_j$, so that

$$\mathbf{e}_j = e_{1_j} + \mathrm{i}\,e_{2_j} = (e_{1_j}^s + \gamma_{1_j}) + \mathrm{i}\,(e_{2_j}^s + \gamma_{2_j}). \tag{6.8}$$

As previously discussed in Section 3.2.2 of Chapter 3, the orientation of the intrinsic ellipticity of galaxies is random. The distribution of each ellipticity component can be approximated to a Gaussian, as shown in Figure 6.2. We assign an intrinsic ellipticity to each galaxy drawn at random with a Gaussian probability distribution (Numerical Recipes, Press, 2002). The width of the Gaussian distribution is equal to the observed ellipticity dispersion obtained from the shear-photo-z catalogs. The values are $\sigma_{e_1^s} \sim \sigma_{e_2^s} = 0.34$ for the CFHT data and $\sigma_{e_1^s} \sim \sigma_{e_2^s} = 0.30$ for the Subaru. We generate 100 sets of random ellipticities and add to the shear according to equation (6.8) to both isolated-pure-shear and multiple-lens-shear catalogs. Hereafter, we call these catalogs *isolated-shape-noise* and *multiple-lens-shape-noise*.

To summarize, for each galaxy group in our sample there is:

- 1 isolated-pure-shear catalog;
- 100 isolated-shape-noise catalogs;
- 1 multiple-lens-pure-shear catalog;
- 100 multiple-lens-shape-noise catalogs.

Figure 6.3 shows the schematic of the shear mock catalogs.

To conclude, Figure 6.4 shows the impact of multiple lenses on the shape of background galaxies and on the tangential and cross shear profiles. The upper left panel shows the shear field in the vicinity of a galaxy group with mass $M_{200} = 2.6 \times 10^{13}\,\mathrm{M_\odot}$ and redshift $z_d = 0.35$. The group is centered at the position marked by the star. The upper right panel shows the total shear field, i.e., the shear originating from all galaxy groups. The positions of the surrounding groups are marked by the crosses. The black dots in the left panel show the tangential and cross shear profiles if the group was isolated in the sky, whereas the gray dots show the real profiles one measures in reality, which are slightly perturbed in comparison to the isolated lens context.
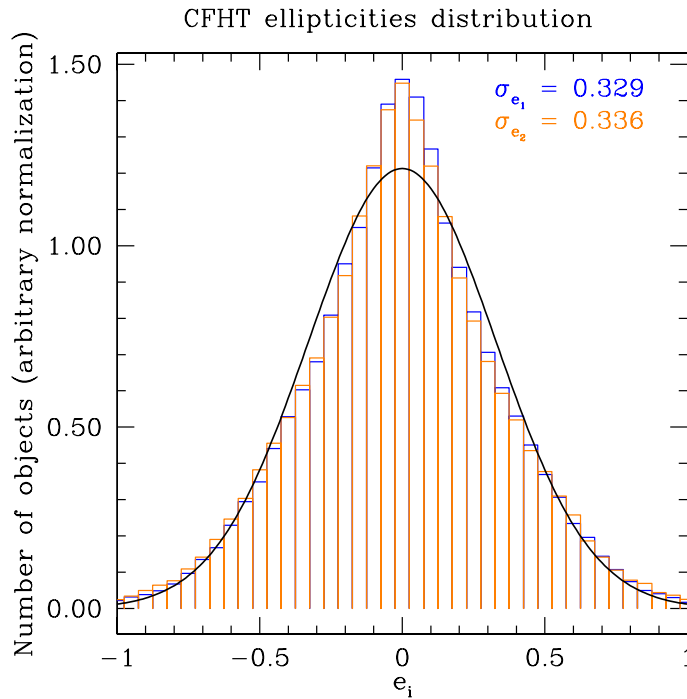
Figure 6.2: Distribution of the ellipticity components of galaxies. Each ellipticity component (blue is for e_1^s and orange is for e_2^s) has a probability distribution close to a Gaussian (black solid line). The Gaussian width used is equal to the to observed ellipticity dispersion. In this example, the ellipticities are taken from the CFHT shear-photo-z catalog. The observed ellipticity dispersion for each component is of the order of $\sigma_{e_i^s} = 0.34$.
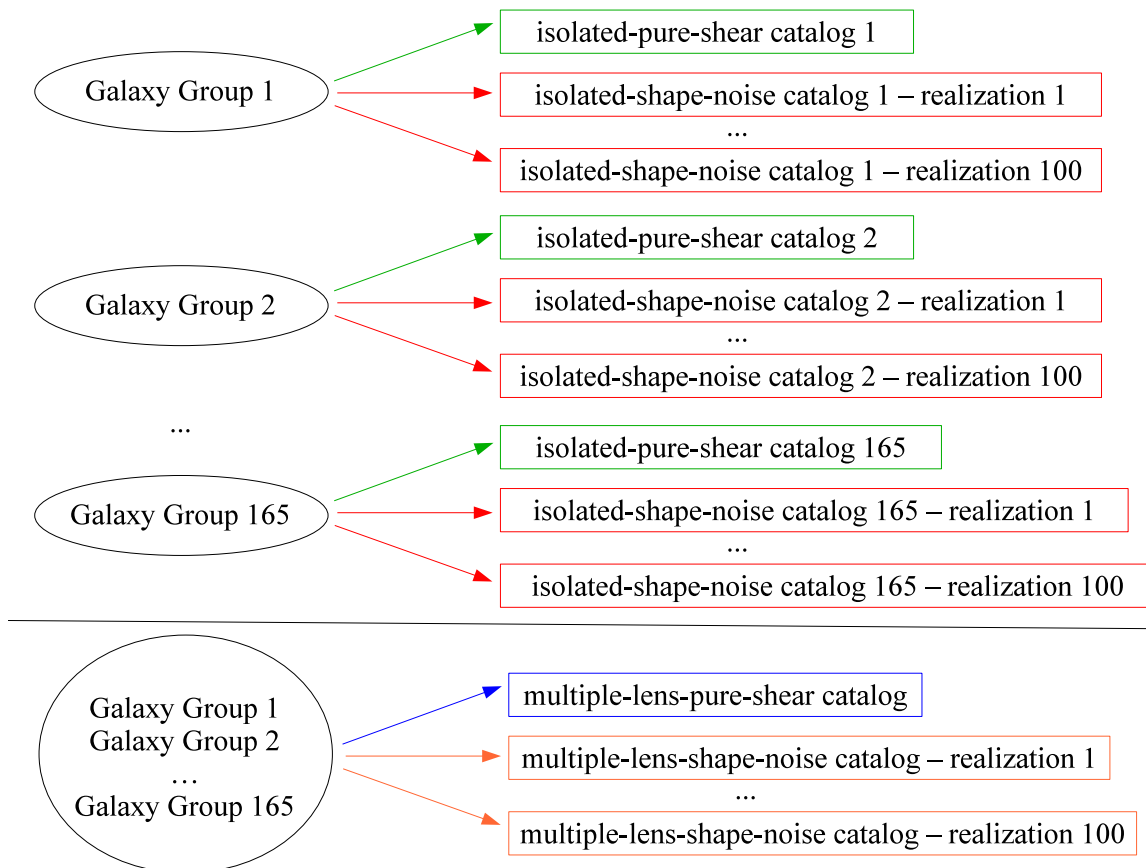
Figure 6.3: Schematic of the shear mock catalogs.
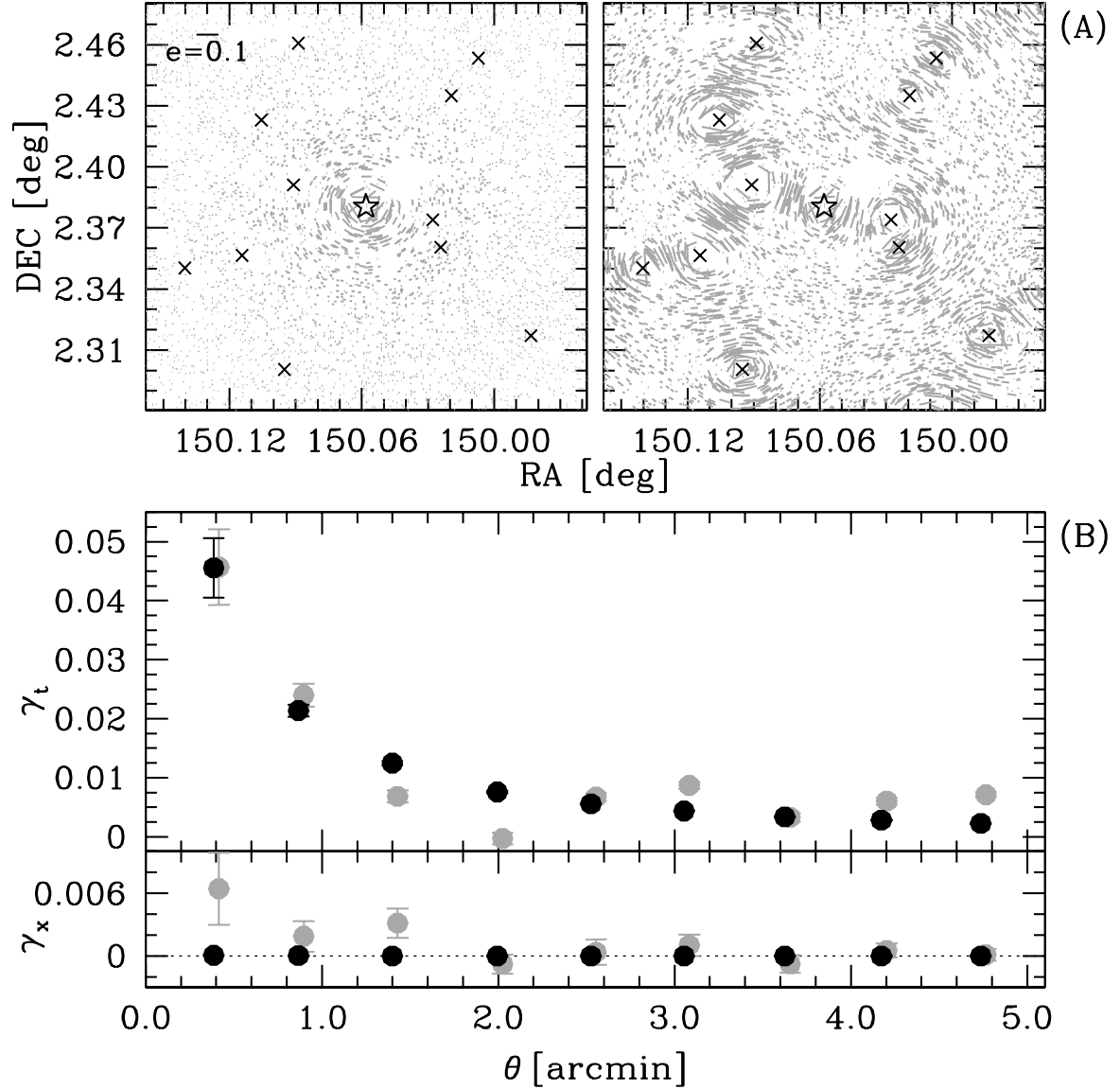
Figure 6.4: Panels (A): Visual impression of the shear field. Each stick corresponds to a background galaxy ($z_s > z_d + 0.05$ and $z_s \geq 0.4$). The orientation and the size of the sticks indicate the magnitude and the direction of the shape distortion. Panels (B): Tangential γ_t and cross γ_x shear profiles. The profiles are slightly offset along the abscissa for clarity. The intrinsic ellipticity is not taken into account in this plot. Illustrated Case: Top panels show the induced shape distortion in background galaxies by a group of mass $M_{200} = 2.6 \times 10^{13}\,\mathrm{M}_\odot$ and $z_d = 0.35$, located at the position marked by the star. If the group was isolated in the sky, the shear field would be the one shown in the upper left panel and the averaged tangential and cross shear profiles would be the ones shown by the black dots in the panels (B). However, halos are not isolated in the sky and have neighbors. The position of the neighbors are indicated by the crosses in the panels (A). The actual shear field one observes is the one shown in the upper right panel, and the actual measured tangential and cross shear profiles are the ones shown by the gray dots of panels (B).

Chapter 7

Weak Lensing Analysis

If you experiment needs statistics, you ought
to have done a better experiment.

Ernest Rutherford

The shape distortion is sensitive to all the matter along the line-of-sight. From the bottom panel of Figure 5.2 we notice that more than half of the groups in the field have at least one neighboring halo in a distance $\theta_{\text{close}} < 2.5'$. The proximity of the halos will likely perturb the shear field of each single halo. In this chapter, we investigate how the proximity of halos with masses in the group regime modifies the shear field. By using the mock catalogs, we can disentangle the shear contribution of individual lenses and check whether the detection of halos and density profile estimates are affected by multiple lensing.

7.1 Halo Detection via Weak Lensing Signal

The detectability of halos by their weak lensing signal depends on how much the coherent distortion is significant in comparison to the local shape and shot noise. The aperture mass statistics (M_{ap}), firstly introduced by Schneider (1996), has been broadly used to search for halos and measure their masses. In this method, the tangential shear contribution of all sources that fall inside a circular aperture of a radius θ_0 is summed up with a weight function. By definition the mass aperture mass M_{ap} is related to the convergence κ (see equation 3.11) via

$$M_{ap} = \int \kappa(\boldsymbol{\theta}) \, U(\boldsymbol{\theta}, \theta_0) \, d^2\theta \,, \tag{7.1}$$

where $U(\boldsymbol{\theta}, \theta_0)$ is chosen to be a radially symmetric continuous weight function. What is wanted is to measure the mass excess within the aperture, regardless of the uniform mass sheet which the halos are embedded. Such a *compensated* filter function $U(\boldsymbol{\theta}, \theta_0)$ satisfies

$$0 = \int_0^{\theta_0} U(\boldsymbol{\theta}, \theta_0) \, \boldsymbol{\theta} \, d^2\theta \,. \tag{7.2}$$

It has been shown by Schneider (1996) that the M_{ap} value can be associated directly to the tangential shear γ_t (see equation 3.26) via

$$M_{ap} = \int Q(\boldsymbol{\theta}, \theta_0)\, \gamma_t(\boldsymbol{\theta})\, d^2\theta \,, \tag{7.3}$$

where $Q(\boldsymbol{\theta}, \theta_0)$ is the *shear weight* function, related to the compensated filter $U(\boldsymbol{\theta}, \theta_0)$ through

$$Q(\theta) = \frac{2}{\theta^2} \int_0^{\theta} \left[U(\theta') - U(\theta) \right] \theta'\, d\theta' \,. \tag{7.4}$$

Hereafter, we shall use the notation θ for the absolute value of $\boldsymbol{\theta}$, i.e., $\theta = |\boldsymbol{\theta}| = \sqrt{\theta_1^2 + \theta_2^2}$.

In practice, when applying the M_{ap} statistics to images, the integral of equation (7.3) is expressed by a discrete sum over the observed tangential ellipticities of galaxies $e_{\rm t}$. Thus, the M_{ap} signal is defined as

$$M_{ap} = \frac{1}{N_{\theta_0}} \sum_{i=1}^{N_{\theta_0}} e_{{\rm t}_i}(\theta_i)\, Q_i(\theta_i, \theta_0) \tag{7.5}$$

with N_{θ_0} being the number of sources within an aperture. The M_{ap} value is usually calculated by placing the aperture on a grid that covers the data region. The distance θ_i is the projected angular distance between the aperture center θ_c and the i-th source galaxy. The observed tangential shear $e_{\rm t}$ is defined as $e_{\rm t}(\theta) = -\Re[\mathbf{e}(\theta) \times \exp(-2{\rm i}\phi_c)]$, with ϕ_c being the polar angle between the horizontal axis and the position θ of the source galaxy relative to the aperture center θ_c. Since the M_{ap} value estimated for the cross component of the shear, defined as $e_{\rm x}(\theta) = -\Im[\mathbf{e}(\theta) \times \exp(-2{\rm i}\phi_c)]$, has expectation value equals zero, it will be used as tool to search for systematics errors. The cross component of the mass aperture statistics $(M_{ap_{\rm x}})$ is calculated by the substitution of $e_{\rm t}$ by $e_{\rm x}$ in equation (7.5).

In the absence of lensing effects, the variance of M_{ap} within the aperture is given by

$$\sigma_{M_{ap}}^2 = \frac{\pi \sigma_{\mathbf{e}^{\rm s}}^2}{N_{\theta_0}} \int_0^{\theta_0} Q^2\left(\boldsymbol{\theta}, \theta_0\right) \boldsymbol{\theta}\, d\theta \,, \tag{7.6}$$

where $\sigma_{\mathbf{e}^{\rm s}}$ is the two-component ellipticity dispersion of galaxies. The discrete formulation of the variance is defined as

$$\sigma_{M_{ap}}^2 = \langle M_{ap}^2 \rangle - \langle M_{ap} \rangle^2 \,, \tag{7.7}$$

but $\langle M_{ap} \rangle = 0$ in the absence of lensing effects, thus

$$\sigma_{M_{ap}}^2 = \frac{1}{N_{\theta_0}^2} \sum_{i,j=1}^{N_{\theta_0}} \langle\, e_{{\rm t}_i}(\theta_i)\, e_{{\rm t}_j}(\theta_j)\, Q_i(\theta_i, \theta_0)\, Q_j(\theta_j, \theta_0) \,\rangle \tag{7.8}$$

and because $e_{{\rm t}_i}(\theta_i)$ and $e_{{\rm t}_j}(\theta_j)$ are mutually independent for $i \neq j$, the variance is given by

$$\sigma_{M_{ap}}^2 = \frac{1}{N_{\theta_0}^2} \sum_{i=1}^{N_{\theta_0}} \langle e_{{\rm t}_i}^2 \rangle\, Q_i^2(\theta_i, \theta_0) \tag{7.9}$$

where $\langle e_{\rm t}^2 \rangle = \sigma_{\mathbf{e}^{\rm s}}^2 / 2$.

The significance of the detection is computed via the signal-to-noise ratio

$$\text{S/N} = \frac{M_{ap}}{\sigma_{M_{ap}}} = \frac{\sqrt{2}}{\sigma_{\mathbf{e}^s}} \frac{\sum_{i=1}^{N_{\theta_0}} e_{\text{t}_i}(\theta_i) Q_i(\theta_i, \theta_0)}{\sqrt{\sum_{i=1}^{N_{\theta_0}} Q_i^2(\theta_i, \theta_0)}}. \tag{7.10}$$

It should be noted that, for several times in previous works, when an arbitrary choice of $\sigma_{\mathbf{e}^s}$ is made, this quantity is set to 0.30. However, for most of the cases, this value is consistent with the dispersion of only one component. If such a wrong value is used, then S/N can be incorrectly improved by a a factor $\sim 30\%$. We refer to Bartelmann & Schneider (2001) for further information on the M_{ap} statistic technique.

Several types of filter functions $Q(\boldsymbol{\theta}, \theta_0)$ have been used in the literature. In Schneider et al. (1998) a family of polynomial filters was proposed

$$Q(\chi) = \frac{(1+l)(2+l)}{\pi \theta_0^2} \chi^2 (1 - \chi^2)^l \tag{7.11}$$

where $\chi = \theta/\theta_0$ and l gives the polynomial order. Although this filter was extensively used in the past, it is not optimal because halos do not have a density profile that follows a polynomial function. Therefore, a filter that has the shape similar to an NFW profile[1] and enhances the signal-to-noise was proposed by Schirmer (2004)

$$Q(\chi) = \frac{1}{1 + \exp(\text{a} - \text{b}\chi) + \exp(-\text{c} + \text{d}\chi)} \left[\frac{\tanh\left(\frac{\chi}{x_c}\right)}{\pi \theta_0^2 \left(\frac{\chi}{x_c}\right)} \right]. \tag{7.12}$$

We take these two filter functions to study the weak lensing signal-to-noise ratio of the selected galaxy groups. We use $l = 1$ for the polynomial filter. For the NFW filter function we use $a = 6$, $b = 150$, $c = 47$, $d = 50$ and $x_c = 0.15$. The motivation for choosing these values is found in Hetterscheidt et al. (2005): a and b set with these values make an exponential drop of Q in $\chi = 0$; c and d make an exponential cut-off in $\chi = 1$ and $x_c \sim 0.15$ maximizes the S/N for several aperture sizes; polynomial order $l = 1$ also makes the Q function drop sharply so that $Q(\chi = 1) = 0$. Figure 7.1 shows the behavior of these two filters Q as function of the dimensionless radius χ.

It has been pointed out by Maturi et al. (2005, 2010) that weak lensing cluster detection can be significantly improved if NFW-like filters are adapted in such a way that the LSS signal contribution is suppressed. Gruen et al. (2011) performed a study showing that their simple strategy are not always successful, in particular when the background density of galaxies is high (as it is for the COSMOS space data). This is because pure LSS filters place higher weights in the innermost regions of the halos, where variations of the shear profile due to correlated structures are more important, and thus, the virial mass estimates can become more insecure if a LSS filter is used. We therefore restrict ourselves to pure NFW and polynomial filters in this work.

The signal-to-noise ratio of a weak lensing detection depends on the aperture size θ_0. In order to calculate the aperture size θ_{opt} that maximizes the signal-to-noise S/N for each lens and filter, we place several aperture sizes on the position of the halos, checking the aperture

---

[1] Although this filter is not strictly an NFW filter, we called it NFW in agreement with previous works, like Schirmer (2004).
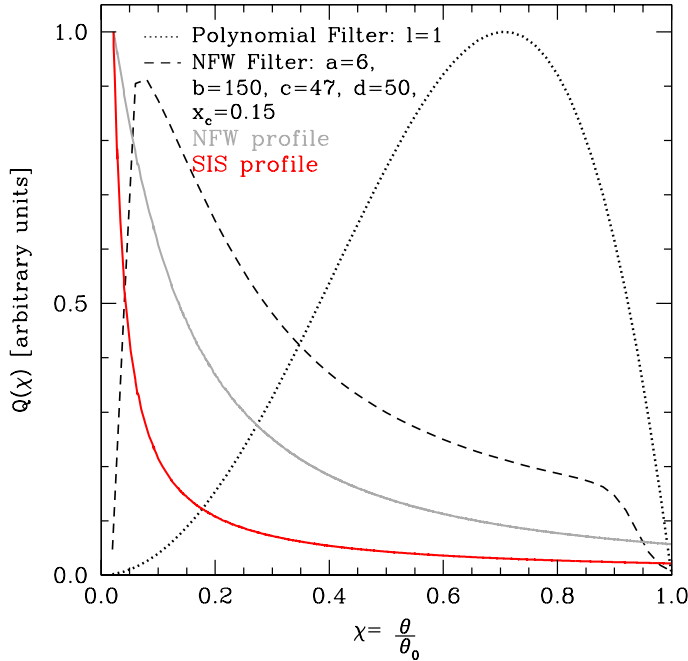
Figure 7.1: The filter Q as a function of the dimensionless radius χ. Black lines show the shape of the Q function for the set of parameters described in the text. The dotted line shows the polynomial and the dashed line shows the NFW filter function. The solid gray line shows the tangential shear profile of a group with $M_{200} = 2.5 \times 10^{13}$ $M_\odot$ at $z_d = 0.30$, assuming that the halo is described by an NFW density profile. The solid red line shows the tangential shear profile of a group with $\sigma_v = 310$ km s^{-1}, also at $z_d = 0.30$, but which is described by singular isothermal sphere (SIS) profile. The tangential shear profile is scaled to match the peak of the filter function.

value for which the signal-to-noise S/N is maximized. Only galaxies with $z_s > z_d + 0.05$ and $z_s \geq 0.40$ are taken into account. The signal-to-noise S/N of each galaxy group is calculated using the isolated-pure-shear catalog with a CFHT-like configuration. The input value of the ellipticity dispersion in equation (7.10) is $\sigma_{\mathbf{e}^s} = 0.47$. We call the attention that, calculating the signal-to-noise S/N using the isolated-pure-shear catalogs results in the mean expected signal-to-noise $\langle$S/N$\rangle$, i.e., the mean value of the S/N distribution obtained from different realizations of random samples of intrinsic ellipticity. Figure 7.2 illustrates this for a test-case halo: we calculate the S/N ratio of a halo (labeled with ID=106 in Table A) using the 100 isolated-shape-noise catalogs with a CFHT-like configuration. The mean expected value of the signal-to-noise distribution $\langle$S/N$\rangle$ is marked in red. The same result is obtained by directly calculating the signal-to-noise S/N from the isolated-pure-shear catalog of the halo. Of course if the number of random realizations of intrinsic ellipticity is small, there is a mismatch between the mean expected signal-to-noise of the distribution and the value directly calculated from the isolated-pure-shear catalog.

Figure 7.3 shows the distribution of the optimal apertures sizes for the galaxy groups in our sample. We find a median value of $\bar{\theta}_{\mathrm{opt}} = 2.0'$ for the polynomial filter and $\bar{\theta}_{\mathrm{opt}} = 4.6'$ for the NFW filter function. In general, the NFW filter requires larger aperture sizes than the polynomial filter. Using a Subaru-like configuration, the distribution of optimal apertures changes a bit but the median values for the two filter functions remain the same.

A comparison of the mean expected signal-to-noise $\langle$S/N$\rangle$ between the two filter functions evaluated in the isolated-lens context is shown on the top panel of Figure 7.4. In this plot, we use three apertures sizes to calculate the signal-to-noise ratio: the value which corresponds to the optimal aperture θ_{opt} of each halo and filter, $3'$ and $5'$. The comparison in the multiple-lens context is shown on the bottom panel of the Figure 7.4. Once again, we calculate the signal-to-noise using the CFHT-like configuration with the described criteria to select background

NFW filter function
$\theta_0 = 5'$

$\langle S/N \rangle$

Cluster ID=106
$M=2.19 \times 10^{14}\ M_\odot$
$z_d = 0.729$

Number of ellipticity realizations

S/N

computed from different ellipticity realizations
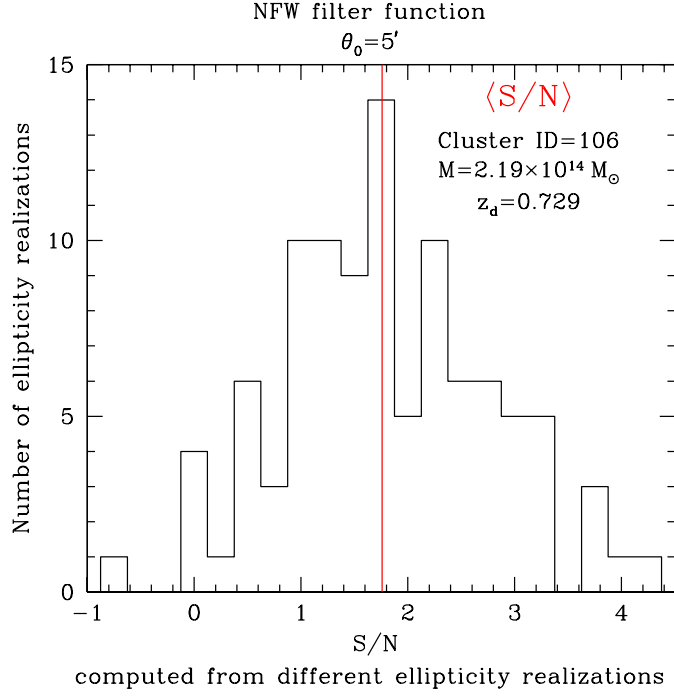
Figure 7.2: Distribution of the signal-to-noise ratio of a halo calculated using 100 realizations of intrinsic ellipticities. In this example, we calculate the S/N of the cluster labeled with ID=106 in Table A. The S/N is computed using the NFW filter, an aperture size of $\theta_0 = 5'$ and a CFHT-like configuration. The mean expected value of the signal-to-noise distribution $\langle S/N \rangle$ is marked by the red line and can also be obtained by using the isolated-pure-shear catalog of the object.

NFW
Polynomial

Number of objects

median $\theta_{\mathrm{opt}} = 2.0'$

median $\theta_{\mathrm{opt}} = 4.6'$

θ_{opt} [arcmin]
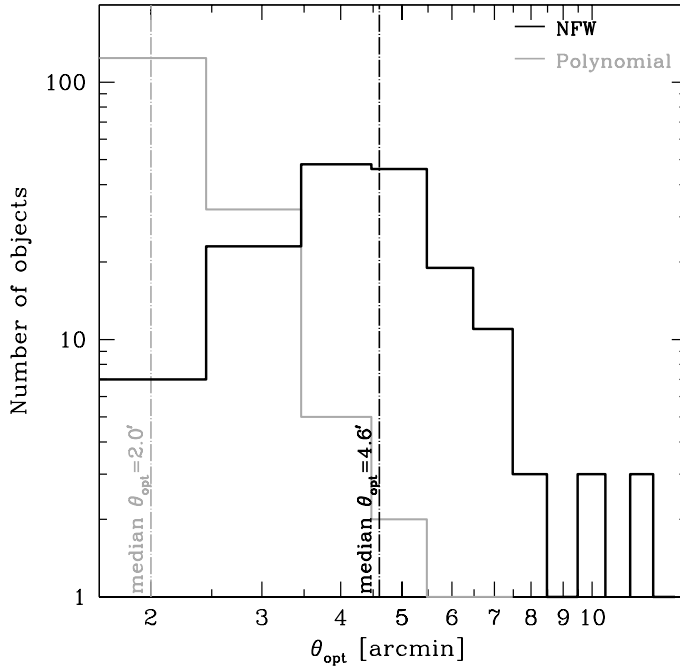
Figure 7.3: Distribution of aperture sizes that maximize the $\langle S/N \rangle$ of each isolated galaxy group. The gray histogram shows the optimal sizes for a polynomial filter function and the black histogram shows the same but for an NFW filter function. The median value of the distribution is $\theta_{\mathrm{opt}} = 2.0'$ for the polynomial filter and $\theta_{\mathrm{opt}} = 4.6'$ for the NFW filter.

Telescope	Isolated Lens		Multiple lenses	
	Polynomial	NFW	Polynomial	NFW
CFHT	1.30	1.87	1.77	2.25
Subaru	1.08	1.59	1.07	1.54

Table 7.1: Maximum of the S/N expectation values for the COSMOS halos.

galaxies. Figure 7.4 shows that if lenses are treated as isolated, the mean expected signal-to-noise using an NFW filter is always higher, even when the optimal aperture $\theta_{\rm opt}$ of each halo and filter is used.

Figure 7.5 shows the difference of the mean expected signal-to-noise $\langle S/N \rangle$ obtained for the isolated and multiple lens calculations as a function of the projected distance $\theta_{\rm close}$ between the galaxy groups and their closest neighbor. Multiple halos along the line-of-sight can both give rise to a larger shear signal or suppress it. The root mean square (rms) values of the difference in the signal-to-noise $\langle S/N \rangle$ are: 0.13, 0.23 and 0.12 for the polynomial filter ($3'$, $5'$ and $\theta_{\rm opt}$ respectively) and 0.09, 0.16 and 0.17 for the NFW filter (also $3'$, $5'$ and $\theta_{\rm opt}$ respectively). It is worth noting that for one galaxy group the difference in the signal-to-noise $\langle S/N \rangle$ is up to a factor of 0.8-1, depending on the aperture size used. We can generalize these results to an arbitrary background galaxy density n_{gal}, obtaining

$$\Delta S/N \approx 15\% \times \sqrt{\frac{n_{gal}}{30}} \quad \text{and} \quad \Delta S/N_{\rm max} \approx 90\% \times \sqrt{\frac{n_{gal}}{30}}\,. \qquad (7.13)$$

The polynomial filter shows more scatter in the difference of $\langle S/N \rangle$ than the NFW filter, which can be explained by the steepness of the NFW filter function. Figure 7.5 also shows that the difference in the signal-to-noise is larger when the closest halo falls within the aperture or, in other words, the difference is larger when the closest halo has a distance smaller than the aperture size used. A Subaru-like configuration does not change the results shown in Figures 7.4 and 7.5, it only yields in smaller values of the signal-to-noise due to lower density of background galaxies.

Table 7.1 shows the maximum value of the signal-to-noise $\langle S/N \rangle$ which can be obtained for the selected galaxy groups using optimal aperture sizes in the measurements. As expected, the maximum signal-to-noise is very low due to the low mass range of the halos studied. It is unlikely that the galaxy groups investigated in this work can be detected by their weak lensing signal with the Subaru- and the CFHT-like configurations.

We conduct the M_{ap} statistics of the whole field area by splitting it into a grid with $12''$ of resolution and evaluate the mean signal-to-noise $\langle S/N \rangle$ at each grid point. An array of 300×300 grid points is necessary to cover the CFHTLS-D2 field and 185×270 to cover the Subaru imaged area. An aperture of $\theta_{0_{\rm poly}} \equiv \bar{\theta}_{\rm opt} = 2.0'$ is used to evaluate the signal-to-noise with the polynomial filter and $\theta_{0_{\rm NFW}} \equiv \bar{\theta}_{\rm opt} = 4.6'$ with the NFW filter. We make a cut in the catalogs to select only source galaxies with $z_s \geq 0.40$. Any other information on the redshift of source galaxies is not taken into account so that all galaxies lying within the aperture are used to evaluate the signal. This is done because when blind searches are conducted to detect halos, the redshift of the halos z_d are not known a priori, making background galaxy selection not possible. When galaxy redshifts are available, it is possible to carry out the analysis using redshifts slices, but this goes beyond the aim of this work. We calculate the signal-to-noise at each grid point using the 100 multiple-lens-shape-noise catalogs and evaluate the
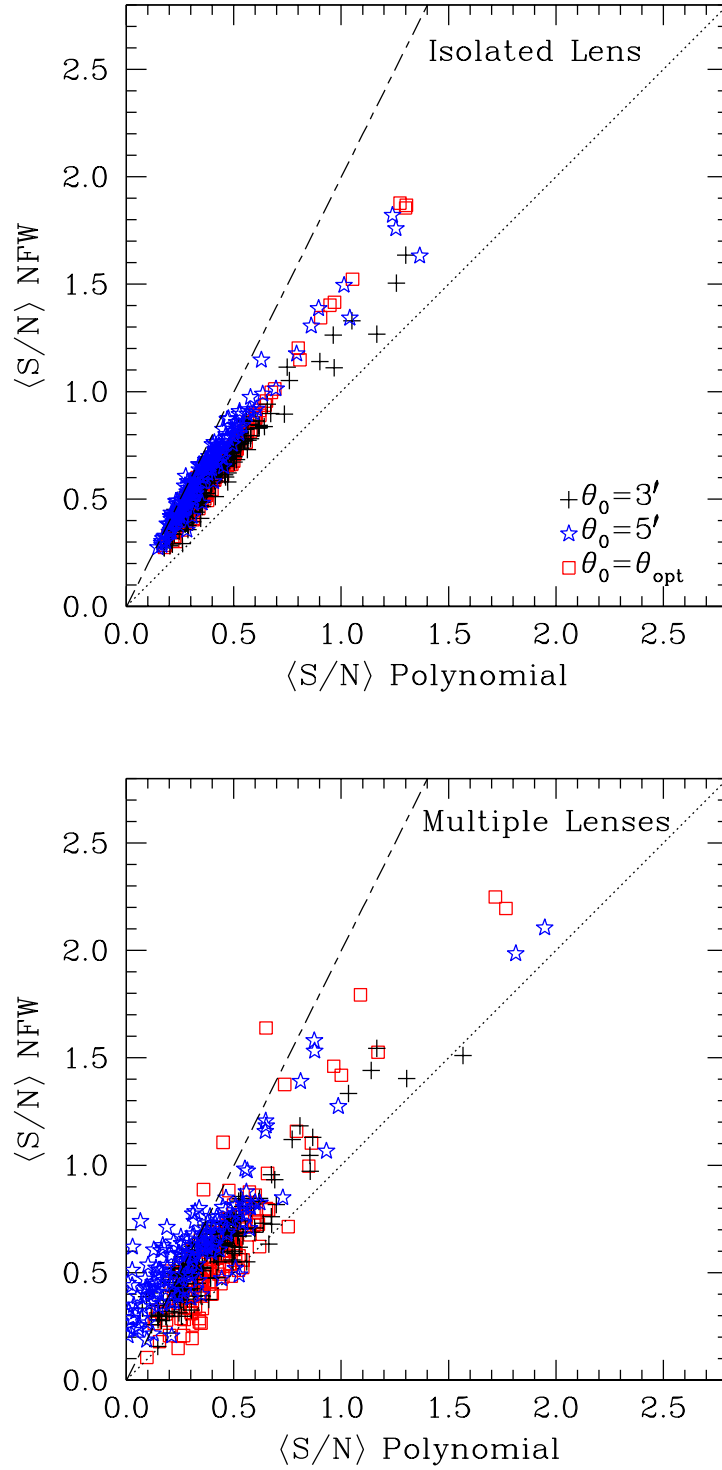
Figure 7.4: Mean expected signal-to-noise $\langle S/N \rangle$ calculated using the M_{ap} statistics for an NFW filter versus a polynomial filter function. The signal-to-noise is obtained from a CFHT-like galaxy distribution for 3 different aperture sizes: $3'$ (black crosses), $5'$ (blue stars), and the aperture value which maximizes the signal-to-noise (red squares) for each halo and filter. The top panel shows the values computed when the lenses are considered isolated in the sky. The bottom panel shows the values calculated considering the contribution of all lens in the FOV. The dotted line has unitary slope and the short-dashed line twice the unity. Both lines are shown for guiding purpose.
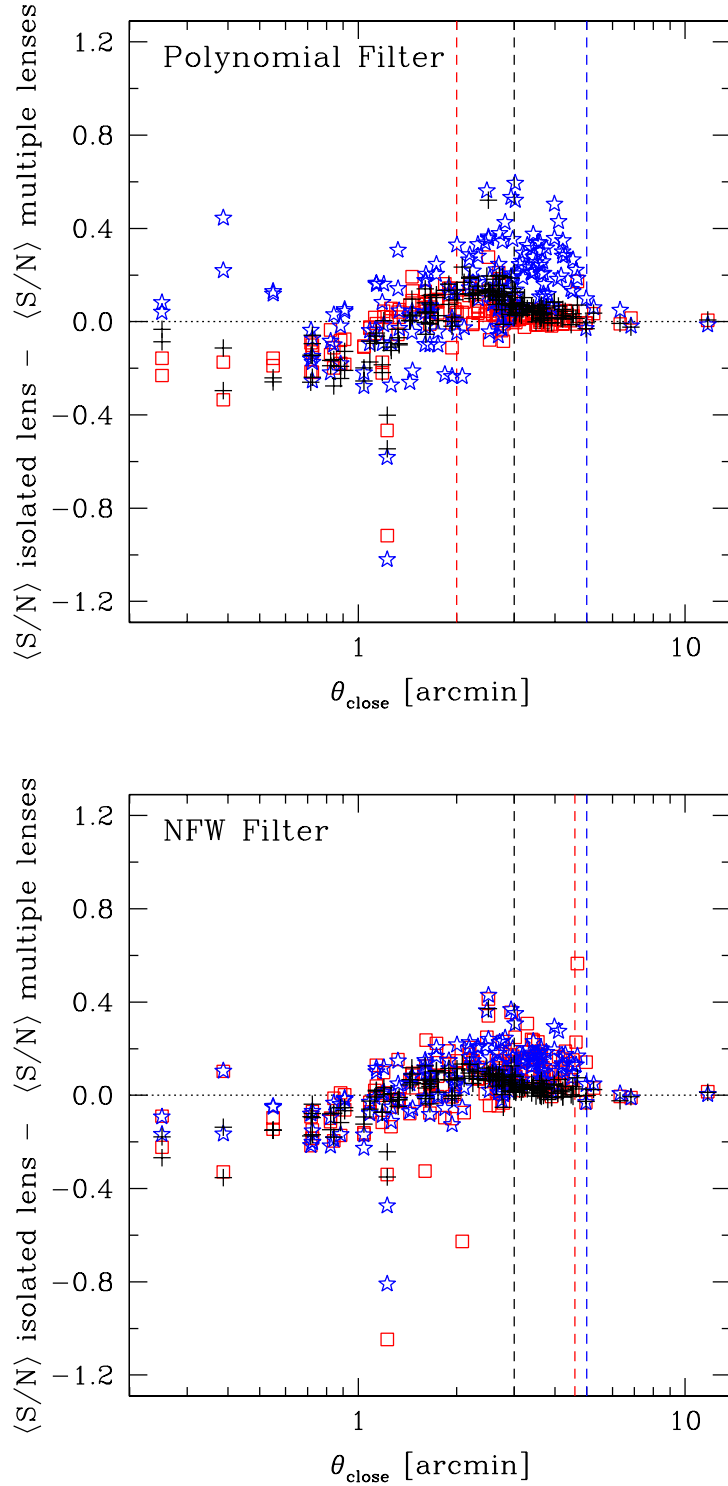
Figure 7.5: Difference of the mean expected signal-to-noise $\langle S/N \rangle$ obtained for the isolated and multiple lens calculations as a function of the distance of the closest neighboring halo θ_{close}. On the top panel we show the difference of the $\langle S/N \rangle$ calculated using the polynomial filter and on the bottom panel we show the same, but for the NFW filter function. Symbols follow the same convention as in Figure 7.4. Vertical lines show the size of the apertures used to calculate the signal-to-noise, except for the red line, which shows the median value of the optimal aperture, being $\bar{\theta}_{\mathrm{opt}} = 2.0'$ for the polynomial and $\bar{\theta}_{\mathrm{opt}} = 4.6'$ for the NFW filter. The rms values of the difference in the signal-to-noise $\langle S/N \rangle$ are: 0.13, 0.23 and 0.12 for the polynomial filter ($3'$, $5'$ and θ_{opt} respectively) and 0.09, 0.16 and 0.17 for the NFW filter function (also $3'$, $5'$ and θ_{opt} respectively).

mean. Figure 7.6 shows the mean expected signal-to-noise $\langle S/N \rangle$ map using the CFHT-like configuration. Figure 7.7 shows the same, but for the Subaru-like distribution. We check the influence of the grid position to the signal-to-noise by displacing the grid points by $6''$, i.e., half of the grid size. The maximum change in $\langle S/N \rangle$ is 0.24 and 0.27 for the polynomial and NFW filters respectively, with an rms of the difference equals 0.02.
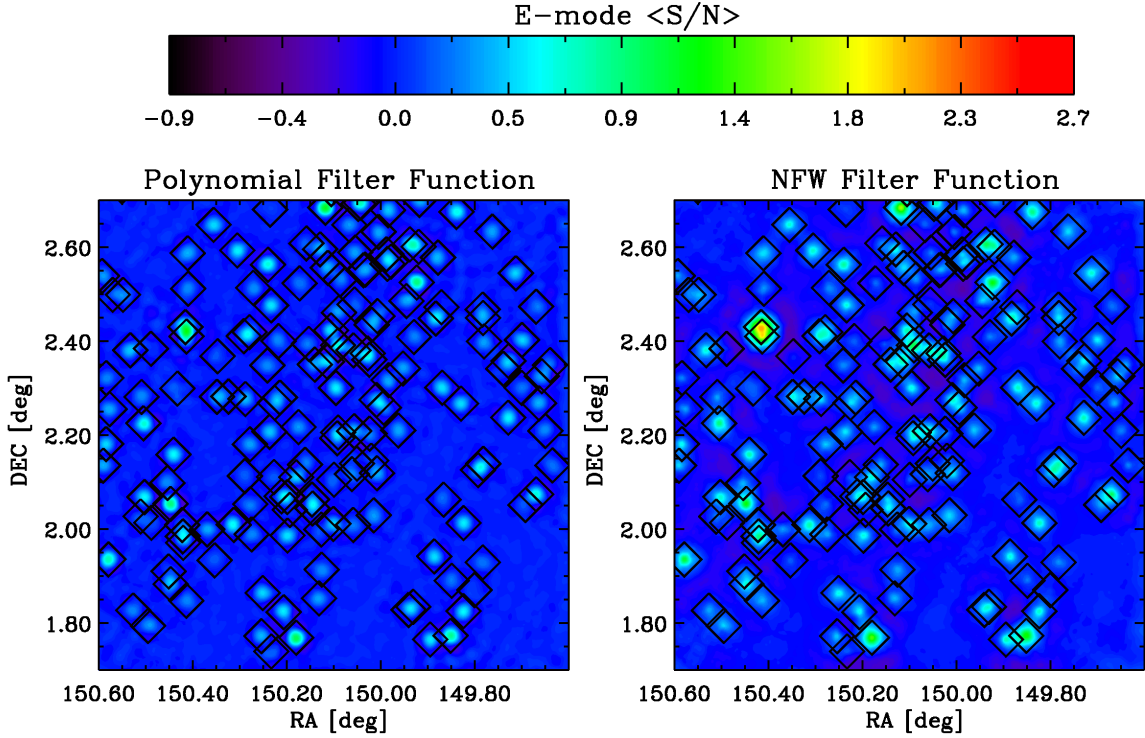
Figure 7.6: Mean expected signal-to-noise $\langle S/N \rangle$ calculated using a COSMOS simulated catalog which have a CFHT-like distribution of galaxies. On the left panel is shown the $\langle S/N \rangle$ map computed with an aperture of $\theta_{0_{\mathrm{poly}}} = 2.0'$ and a polynomial filter. On the right panel is shown the $\langle S/N \rangle$ map computed with an aperture of $\theta_{0_{\mathrm{NFW}}} = 4.6'$ and an NFW filter. Diamonds mark the positions of the selected galaxy groups. If the grid points are shifted by $6''$, the maximum change in $\langle S/N \rangle$ is 0.24 for the polynomial and 0.27 for the NFW filter, with $\Delta\langle S/N \rangle_{\mathrm{rms}} = 0.02$ for both filters.

Likewise, we perform the M_{ap} statistics of the field using a pure intrinsic ellipticity realization and check how the S/N distribution of this *pure-shape-noise* catalog compares to the one obtained from the multiple-lens-pure-shear catalog. Once again, we use an aperture of $\theta_{0_{\mathrm{poly}}} = 2.0'$ for the polynomial filter and $\theta_{0_{\mathrm{NFW}}} = 4.6'$ for the NFW filter function. The S/N distributions of the multiple-lens-pure-shear and pure-shape-noise catalogs with the CFHT-like configuration are shown in Figure 7.8. The same is shown in Figure 7.9 but for the Subaru-like configuration. Only grid points falling inside an aperture that fully lies inside of the data fields are considered, yielding 260×257 grid points for the CFHT and 125×223 grid points for the Subaru configuration. As we can see in Figures 7.8 and 7.9, the pure intrinsic ellipticity follows a Gaussian probability distribution, centered at zero and width $\sigma \sim 1$, i.e., consistent to the S/N units. Therefore, independently of intrinsic ellipticity dispersion of the data, it is possible to have positive and negative E-modes (and also B-modes) originating from the intrinsic ellipticity in a various range of S/N: $|S/N| \leq 1$ accounts for about 68% of
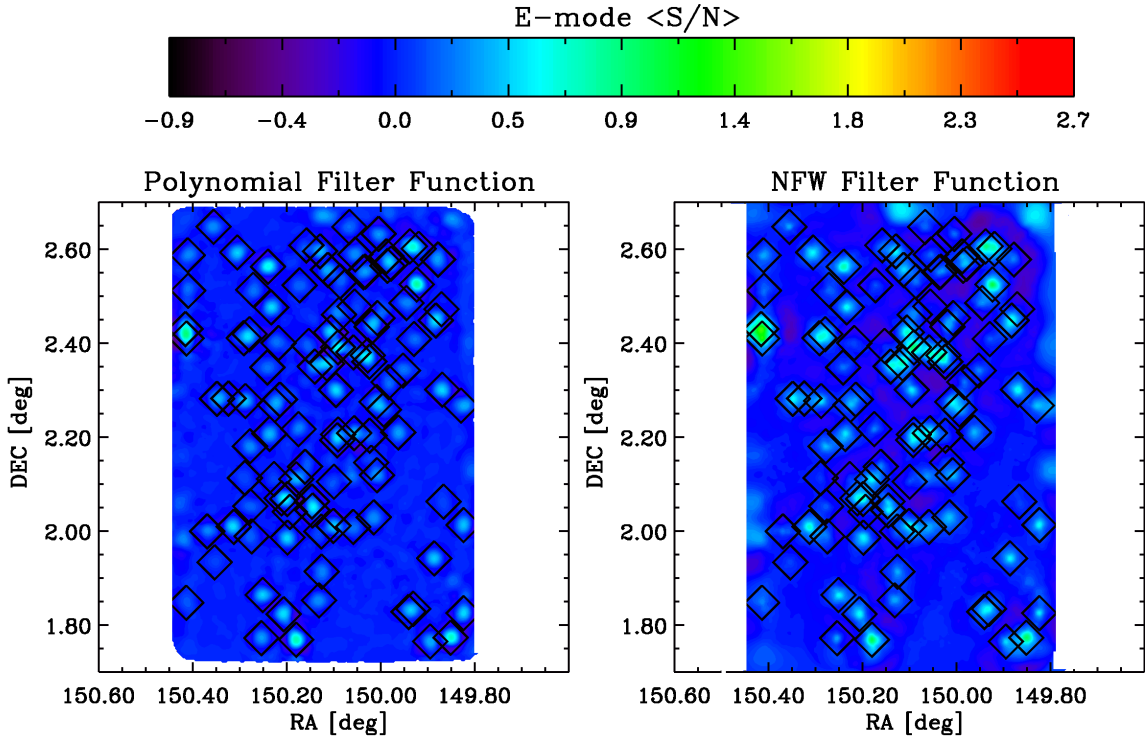
Figure 7.7: The same as Figure 7.6 but for the Subaru-like distribution of galaxies.

the set of the grid points, $|S/N| \leq 2$ accounts for 95%, $|S/N| \leq 3$ for 99.7%, $|S/N| \leq 4$ for 99.99%, and so on. Thus, for the CFHT described grid configuration, this means that ~ 200 grid points are expected to have $|S/N| \geq 3$ originating from intrinsic alignments. On the other hand, the gravitational shear originating from the galaxy groups in our sample result in a signal-to-noise smaller than 3, meaning that neither a CFHT nor a Subaru-like configuration are sufficient to detect COSMOS-like halos without contamination generated by false peaks.

Finally, we perform the same analysis but using the observed CFHT and Subaru shear-photo-z catalogs and plot the S/N distribution of the grid points. We evaluate the S/N of E-modes and B-modes and show in Figures 7.10 and 7.11. These two figures demonstrate that the observed shear-photo-z catalogs yield in similar S/N distributions to the ones obtained from the pure-shape-noise catalogs. Furthermore, the S/N distribution of E-modes and B-mode are almost the same. Once more, this shows that the galaxy groups in our sample can not be detected by their weak lensing signal without being contaminated by the false peaks generated by intrinsic ellipticity.

7.2   Previous Halo Detections in the COSMOS Field

In this section we present previously published results on shear measurements in the COSMOS field. Table 5.2 summarizes the results that are discussed in this section.

Our conclusion that COSMOS halos can not be detected at a significant level ensuring low false detections using CFHT and Subaru-like configurations also holds for an HST-like
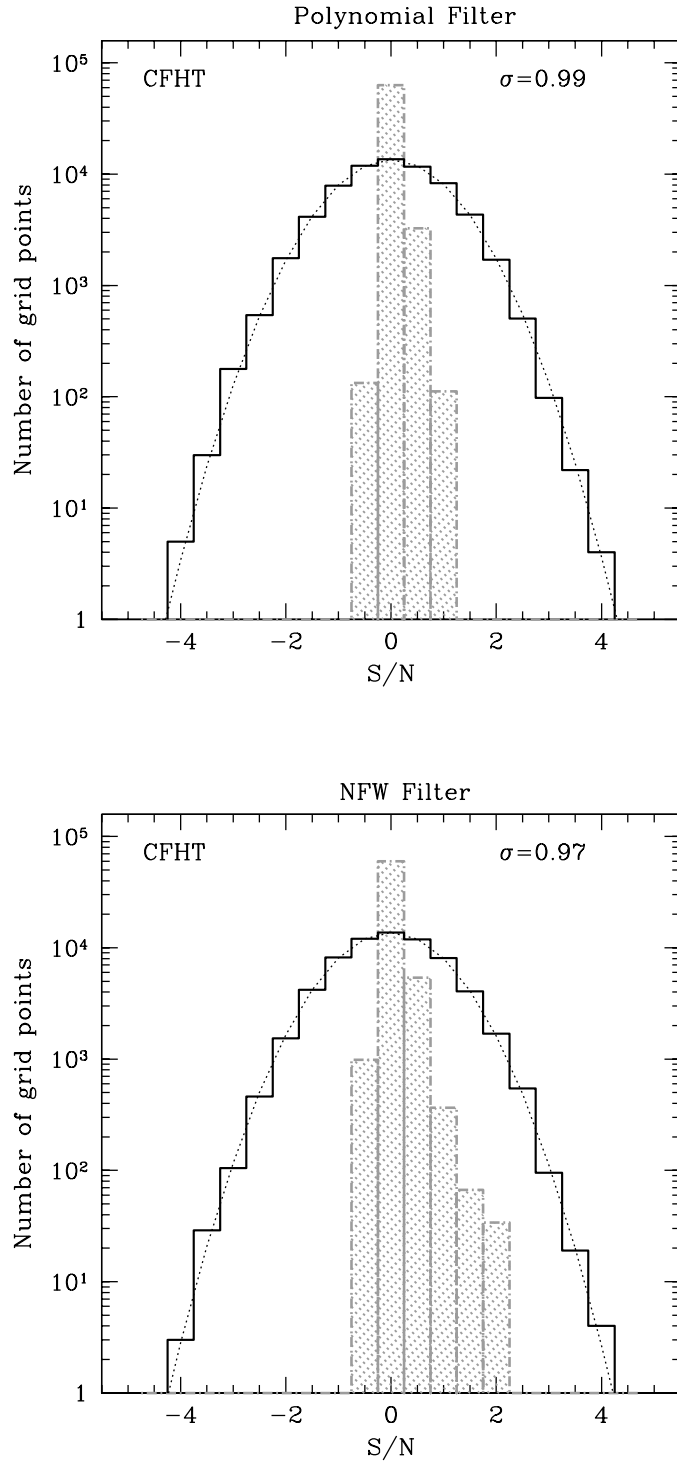
Figure 7.8: Signal-to-noise S/N distribution of the grid points. The grid covers the CFHTLS-D2 field in an array of 300×300 grid points with a step-size of $12''$. Only grid points within an aperture lying totally inside of the field are plotted, yielding 260×257 grid points. The hatched histogram shows the distribution of the mean expected signal-to-noise $\langle S/N \rangle$ obtained from the CFHT multiple-lens-pure-shear catalog. Thick black histogram shows the distribution of S/N obtained from shape noise only, assuming an intrinsic ellipticity dispersion equal to the CFHT configuration, i.e., $\sigma_e^s = 0.47$. The thin dotted line shows the best-fit of a Gaussian function to the intrinsic ellipticity distribution. The fitted sigma σ is written on the plot and is consistent with 1.
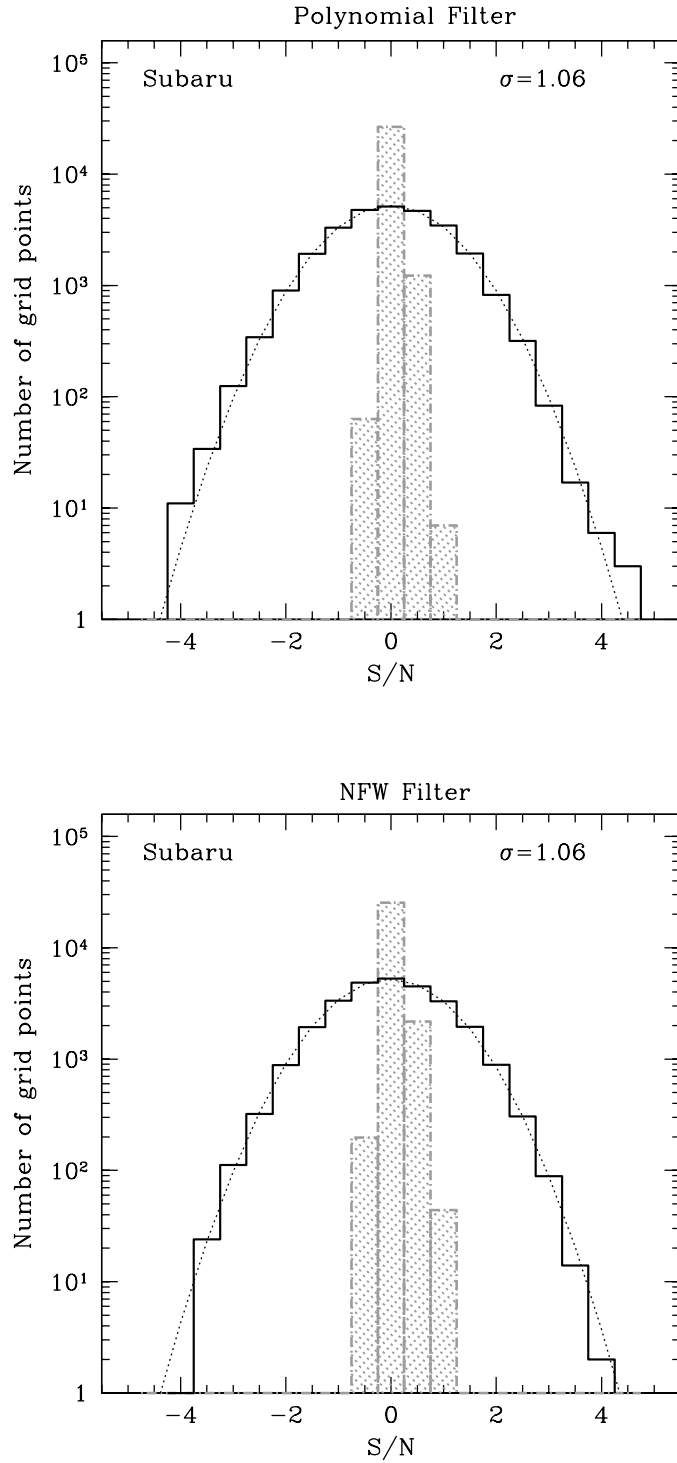
Figure 7.9: The same as Figure 7.8 but for a Subaru-like configuration. An array of 185×270 grid points was necessary to cover the data, but plotted here are just the grid points that fully lie on the data field, yielding 125×223 grid points. The hatched histogram shows the distribution of the mean expected signal-to-noise $\langle S/N \rangle$ obtained from the Subaru multiple-lens-pure-shear catalog. Thick black histogram shows the distribution of S/N obtained from shape noise only, assuming an intrinsic ellipticity dispersion equal to the Subaru configuration, i.e., $\sigma_e^s = 0.42$.
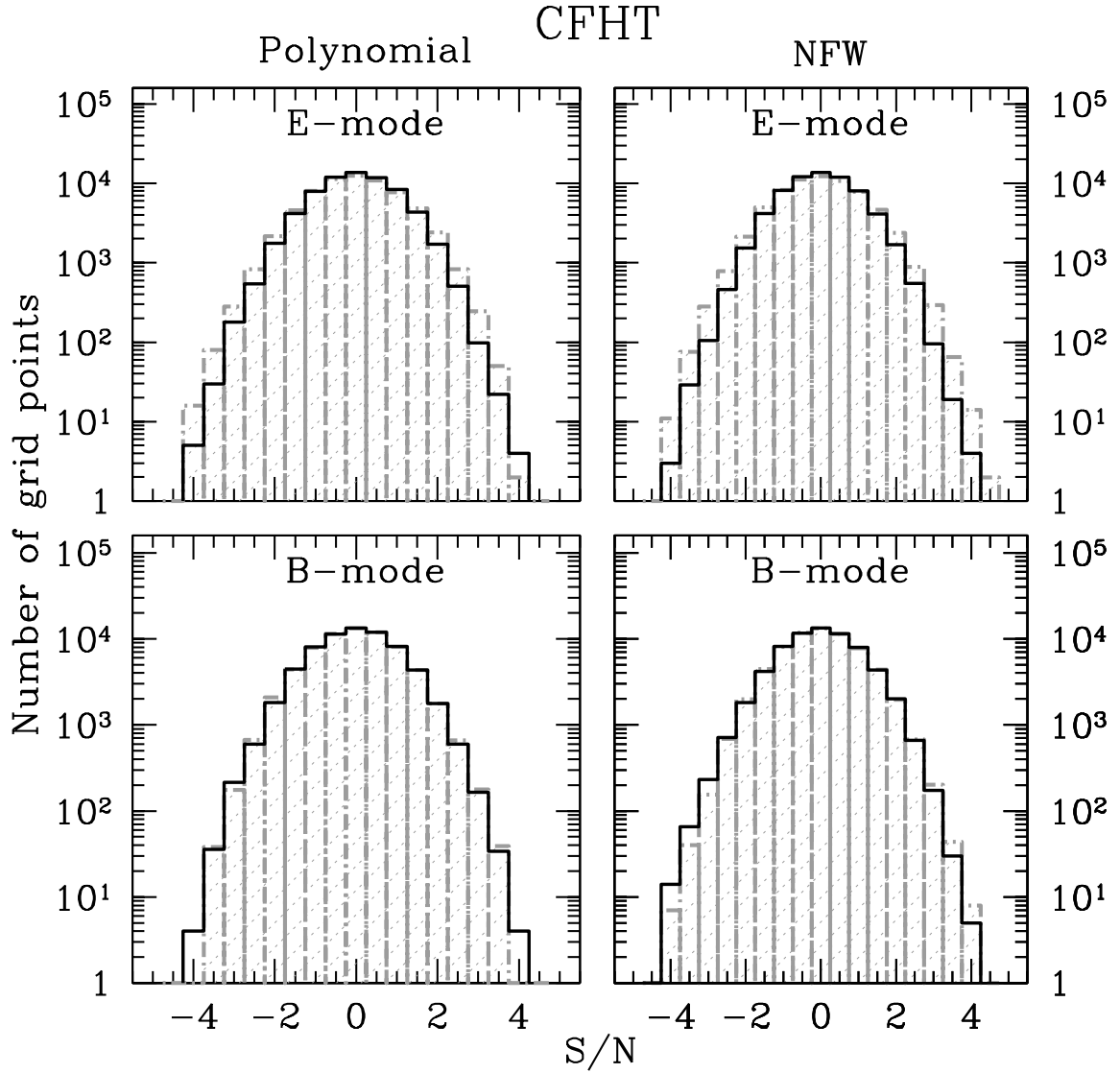
Figure 7.10: Same as Figure 7.6 but for the observed CFHT shear-photo-z catalog. Upper panels show the distribution of E-modes and lower panels the distribution of B-modes. The hatched histogram shows the distribution of the signal-to-noise S/N obtained from the CFHT shear-photo-z catalog. Thick black histogram shows the distribution of S/N obtained by shape noise only, assuming an intrinsic ellipticity dispersion equal to the CFHT configuration, i.e., $\sigma_e^s = 0.47$.
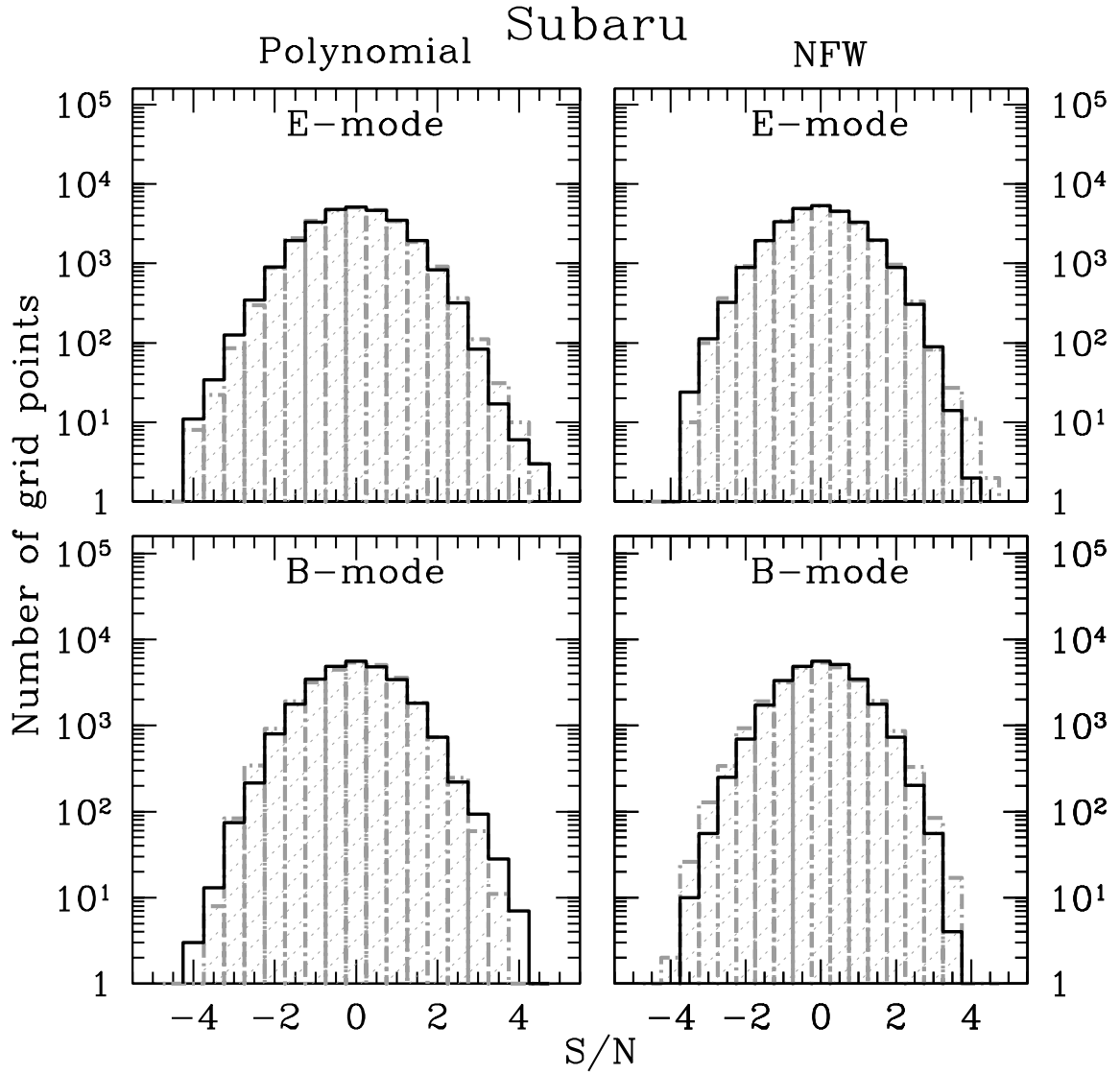
Figure 7.11: Same as Figure 7.6 but for the observed Subaru shear-photo-z catalog. The hatched histogram shows the distribution of the signal-to-noise S/N obtained from the Subaru shear-photo-z catalog. Thick black histogram shows the distribution of S/N obtained by shape noise only, assuming an intrinsic ellipticity dispersion equal to the Subaru configuration, i.e., $\sigma_e^s = 0.42$.

configuration, as it was shown by Leauthaud et al. (2010). They used the approach introduced by Hamana et al. (2004) to predict the signal-to-noise ratio of the same halos studied in this work but for an HST-like galaxy distribution, with $n_{shear} = 66$ galaxies arcmin^{-2}. Their ellipticity dispersion includes shape noise ($\sigma_{e_i^s} \sim 0.27$) and shape measurement errors yielding $\sigma_{e_i^{total}} = \sigma_{e_i^s} + \sigma_{e_i^{err}} = 0.31$ per component. Following Hamana et al. (2004), they computed the convergence map convolved with a Gaussian kernel. They found that even with an HST-like galaxy distribution, COSMOS systems can not be detected individually, except for nine halos that have S/N > 4 (see Figure 1 from Leauthaud et al., 2010). From these nine systems, only two of them are in our field-of-view. These two halos have 4 < S/N < 5 with an HST-like configuration. We check the S/N of these systems with a Subaru and CFHT-like configurations using the Hamana et al. method and the same parameters choices as presented in Leauthaud et al. (Gaussian kernel $\theta_G = 1'$ and background galaxies fixed at $z_s = 1$). The signal-to-noise ratios are related through

$$\text{S/N} = \text{S/N}_{\text{Ham+04}} \times \left(\frac{0.40}{\sigma_{\mathbf{e}^s}}\right) \sqrt{\frac{n_{shear}}{30}} \left(\frac{D_{ds}}{D_s}\right) \left[\left(\frac{D_{ds}}{D_s}\right)\Big|_{z_s=1}\right]^{-1}, \qquad (7.14)$$

which yields S/N$_{\text{Leau+10}}$ = S/N$_{\text{Ham+04}}$ × 1.35, S/N$_{\text{CFHT−this work}}$ = S/N$_{\text{Ham+04}}$ × 0.89 and S/N$_{\text{Subaru−this work}}$ = S/N$_{\text{Ham+04}}$ × 0.84, using the galaxy density of the CFHT and Subaru shear catalogs given in Table 5.2 (n_{shear} = 32.8 galaxies arcmin^{-2} and n_{shear} = 23.7 galaxies arcmin^{-2}). We visually inspect the Figure 3 of Hamana et al. (2004) work and conclude that the galaxy groups in our sample would have a maximum S/N $\sim$ 3 using their approach. Therefore, for these very same halos, the S/N would not be greater than 2.7 for the CFHT-like configuration and 2.5 for the Subaru-like configuration. Since the HST-like configuration yields a S/N $\sim$ 1.52 higher than the CFHT-like, it is possible to detect some of these halos with deep space-based observations as shown in Leauthaud et al. (2010).

Nevertheless there are weak lensing detections in the COSMOS field claimed in the literature. Kasliwal et al. (2008) detected 3 systems using both HST and Subaru data. The E-mode peaks were measured using the convergence map with a kernel $\theta_G = 1'$, and only detections with S/N> 4 were considered as safe. The detection named as A is a real cluster with an X-ray counterpart at $z_d = 0.73$. The detection named as B matches an X-ray peak at $z_d = 0.83$ but the signal is claimed to be originating from a group at $z_d \sim 0.3$. Within a region of $\sim 4'$ around the detection B there are two X-rays peaks at $z_d \sim 0.3$ and three X-rays peaks at $z_d \sim 0.85$. Hence, this could be a case where five structures along the line-of-sight act together to produce a signal that is interpreted to be originating from one of these five structures alone. The detection named as C is also real with an X-ray counterpart at $z_d = 0.22$ but it lies outside of both CFHTLS-D2 and Subaru field. This cluster is one of those that could be detected with high S/N in Figure 1 of Leauthaud et al. (2010). The number of the detected galaxies in Kasliwal et al. work is n_{det}=42 galaxies arcmin^{-2} for Subaru[2] and n_{det}=71 galaxies arcmin^{-2} for HST data.

Gavazzi & Soucail (2007) performed a study of the four CFHTLS Deep fields. Using also the convergence map to detect E-mode peaks, with kernel $\theta_G = 1'$, n_{shear}=30.6 galaxies

---

[2]The reason why previous works that used Subaru observations of the COSMOS field show a much higher density of galaxies than we have found in this work is due to stacking strategy used to co-add individual exposures. While we have chosen only exposures taken with similar dither pattern, previous works have stacked all the exposures, regardless of the shift between them and the camera orientation. When combining all the exposures into a final mosaic using the data reduction procedure described in the Section 4.2 of Chapter 4, we are also able to get $n_{shear} \sim 40$ galaxies arcmin^{-2}.

arcmin^{-2}, $z_s \sim 1$ and $\sigma_{\mathbf{e}^s} \sim 0.33$, they found 3 peaks with S/N~ 3.6 in the CFHTLS-D2 field. Detections with S/N> 3.5 were classified as safe. The peak called Cl-08 matches the detection A from Kasliwal et al., although the redshift computed using shear tomography $z_d = 0.44$ does not match the actual redshift of the cluster. The peaks called Cl-09 and Cl-13 have no X-ray association in a distance of $\sim 2.5'$. Also, the redshifts found with the shear tomography do not match the redshift of the nearest galaxy groups at this distance.

In a recent paper Bellagamba et al. (2011) presented an optimal linear filtering technique for optical and weak lensing data. The weak lensing detection was performed in a similar way to the M_{ap} statistics, but using the filter function proposed by Maturi et al. (2005, 2010). This filter function was designed specifically to suppress the contribution from the large-scale structure. The input shear catalog was taken from Miyazaki et al. (2007), which used Subaru data with a density of $n_{shear} = 42$ galaxies arcmin^{-2} and assumed mean redshift of background galaxies of $\bar{z}_s = 0.8$. Using weak lensing solely, they detected 82 peaks with S/N> 3 but 40% of the detections are expected to be spurious. The matched optical and weak lensing catalog reduces the number of detections to 27 systems, where only detections with S/N≥ 3.5 were considered as safe. We check for the X-ray counterparts of these 27 systems and calculate the percentage of spurious detections as a function of signal-to-noise provided in Table 1 of Bellagamba et al. (2011). We make use of the full COSMOS field, since both Bellagamba et al. and the COSMOS X-ray catalogs cover more or less the same area (slightly larger than the CFHTLS-D2 field). In order to calculate the percentage of spurious detections, we split the signal-to-noise into three bins: $3.5 < $ S/N ≤ 4, $4 < $ S/N ≤ 5 and $5 < $ S/N ≤ 9, covering the S/N range of the 27 systems. Then, we check for the X-ray counterpart, matching the spatial position and redshift of the systems to the X-ray halos. When it is not possible to find the match, the system is classified as spurious. Figure 7.12 shows the result: the percentage of spurious detections drops with the increase of signal-to-noise. For systems with S/N > 5 the percentage is zero. For the 12 systems within the bin $4 < $ S/N ≤ 5, 11 have an X-ray peak associated. The positions of the X-ray COSMOS catalog and the positions found using the optical plus weak lensing filtering technique of Bellagamba et al. (2011) are in very good agreement, apart from one system, where the offset is $\sim 2'$. This result makes this technique very promising for searches of groups and clusters of galaxies with a low rate of spurious detections, if a threshold in S/N of 4 is used.

7.3   Tangential Shear Dispersion

In this section we investigate the tangential shear dispersion that the halos in the field introduce in the tangential shear profile of individual groups. The aim of this analysis is to understand the relevance of this "large-scale structure" noise to the total error budget of the shear measurements.

Hoekstra (2001, 2003) investigated the effect of the large-scale structure on mass measurements and how it perturbs the tangential shear profile. By splitting the observed shear into the components

$$\gamma_t(\theta) = \gamma_t^{\text{halo}}(\theta) + \gamma_t^{\text{LSS}}(\theta) \qquad (7.15)$$

one conclusion obtained was that the distant large-scale structure does not affect the mass estimates of clusters of galaxies but does contribute to the uncertainty of the measurement. The work proposed by Hoekstra (2001, 2003) considered a massive cluster ($M_{200} \geq 5 \times 10^{14}$ h^{-1} M$_\odot$) at $z_d = 0.3$ plus a power spectrum of the density fluctuations. Our sample can
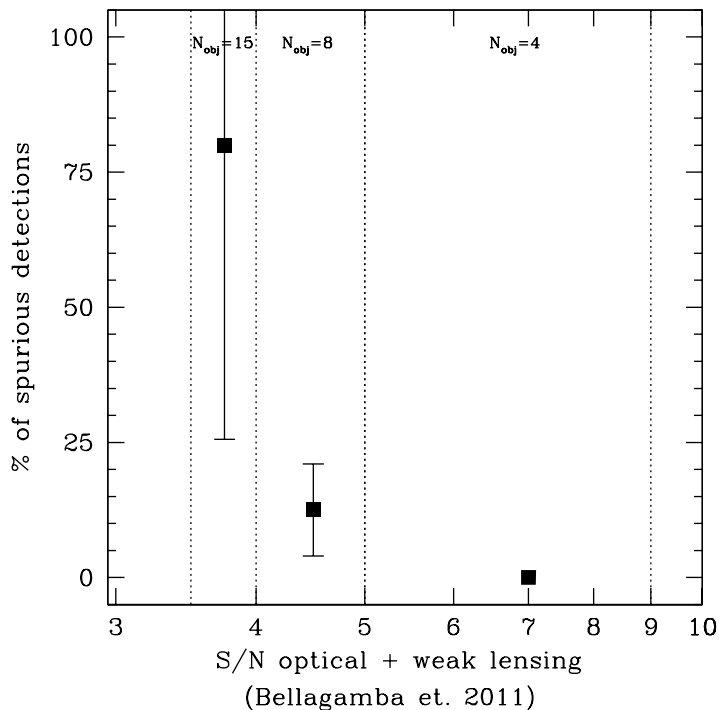
Figure 7.12: Percentage of spurious detections as a function of signal-to-noise of the detected systems in Bellagamba et al. (2011). The signal-to-noise is divided into three bins, which in the figure is delimited by the dashed vertical lines. For each bin, the percentage of spurious detections is calculated from the total number of objects N_{obj} within the bin. The percentage is shown as points with 1σ error bars.

not be treated in the same way, because the field is populated by several lenses. Following Hoekstra (2001, 2003), we split the observed shear in components but also subdivide the shear due to LSS into two components, in a way that

$$
\begin{aligned}
\gamma_{t}(\theta) &= \gamma_{t}^{halo}(\theta) + \gamma_{t}^{LSS}(\theta) \\
&= \gamma_{t}^{halo}(\theta) + \gamma_{t}^{close-halos}(\theta) + \gamma_{t}^{distant-halos}(\theta) \,,
\end{aligned}
\tag{7.16}
$$

where the component $\gamma_{t}^{close-halos}$ includes the shear introduced by all halos with a maximum distance of $5'$ from the center of the main halo. The shear signal introduced by the other halos in the field is taken into account by the $\gamma_{t}^{distant-halos}$ term. The motivation for choosing $5'$ as the dividing line between *close-halos* and *distant-halos* is: (1) the optimal aperture value for detections of the individual halos using an NFW filter is $\theta \sim 5'$ (see Figure 7.3) and; (2) the nearest halo separation peaks at $\theta \sim 2.5'$ dropping almost to zero at $\theta \sim 5'$ (see Figure 5.2). Using a dividing line of $5'$ implies that all constellations have at least one extra halo in addition to the main one. Consequently the *close-halos* term can be interpreted as a second-halo term seen in projection.

A good approximation for the dispersion in the averaged tangential shear within a measured radius θ is

$$
\sigma_{\gamma_{t}}^{obs^{2}}(\theta) \sim \frac{\sigma_{\mathbf{e}^{s}}{}^{2}}{2N}(\theta) + \sigma_{\gamma_{t}}^{close-halos^{2}}(\theta) + \sigma_{\gamma_{t}}^{distant-halos^{2}}(\theta)
\tag{7.17}
$$

since the correlation between $\gamma_{t}^{close-halos}$ and $\gamma_{t}^{distant-halos}$ is small. In this equation, N is the number of galaxies for which the tangential shear is measured.

Next, we investigate how the tangential shear of the main halo is affected by the presence of the other galaxy groups in the field. For this analysis we use the CFHT shear simulations due

to larger sky coverage than the Subaru simulations. Using the isolated-pure-shear catalogs of each group, we compute the tangential shear within an aperture for the three terms of equation (7.16). In order to quantify $\gamma_t^{\text{close}-\text{halos}}$ and $\gamma_t^{\text{distant}-\text{halos}}$ for each main halo, we first identify the galaxy groups matching the *close-halos* and *distant-halos* criteria. Then, the total shear of the j-th galaxy is calculated by summing the shear over all the groups classified as close and distant separately. This procedure is similar to what we did to generate the multiple-lens-pure-shear catalog using equation (6.7), but now the number of *close-halos* and *distant-halos* is different for each galaxy group.

The tangential shear dispersion is measured for two aperture sizes: $R = r_{200}$ of the main galaxy group and $R = r_{200} \times 4$, which is equivalent $\sim 5'$ or ~ 2 Mpc for COSMOS halos. We have only used the groups for which the measured radii are fully inside the data field. Figure 7.13 shows the terms $\sigma_{\gamma_t}^{\text{close}-\text{halos}}(R)$ and $\sigma_{\gamma_t}^{\text{distant}-\text{halos}}(R)$ as a function of the redshift of main galaxy group z_d and as a function of the projected distance to closest neighbor θ_{close}. On the top panel, the measurements are performed for $R = r_{200}$ and on the bottom panel for $R = r_{200} \times 4$.

From Figure 7.13, for the measurements within r_{200} we conclude that: (1) the shear dispersion of the *close-halos* term is a steep function of the closest halo proximity; (2) the shear dispersion of the *distant-halos* term is smaller than the *close-halos* term. The mean values of the tangential shear dispersion are: $\sigma_{\gamma_t}^{\text{close}-\text{halos}}(r_{200}) \sim 0.006$ and $\sigma_{\gamma_t}^{\text{distant}-\text{halos}}(r_{200}) \sim 0.004$. For measurements within $r_{200} \times 4$ we conclude that: (1) the contribution of *close-halos* and *distant-halos* are of the same order of magnitude, meaning that they can be treated together as a single source of external noise. The mean values of the tangential shear dispersion are: $\sigma_{\gamma_t}^{\text{close}-\text{halos}}(r_{200} \times 4) \sim 0.006$ and $\sigma_{\gamma_t}^{\text{distant}-\text{halos}}(r_{200} \times 4) \sim 0.007$.

On average $\sigma_{\gamma_t}^{\text{LSS}} \sim 0.006$ per component. This value corresponds to $\sim 1.8\%$ of the intrinsic ellipticity value of one component, and is consistent with the values found in Hoekstra et al. (2011): $\sigma_{\gamma_t}^{\text{LSS}} = 0.0060 - 0.0045$ for $\theta < 5'$. We briefly investigate how $\sigma_{\gamma_t}^{\text{LSS}}$ varies with the aperture size. We measure the azimuthally averaged tangential shear as a function of the distance from 100 random positions spread over the field. The dispersion of the azimuthally averaged tangential shear is measured within several apertures and annuli, with a step-size equals $0.5'$. The result is shown in Figure 7.14: the black squares are the measurements within apertures whereas cyan squares are the measurements within annuli. Annuli measurements yield in a noisier profile than for apertures due to small number of sources for each the tangential shear is averaged. We find that our $\sigma_{\gamma_t}^{\text{LSS}}$ estimate is a factor of two higher for large aperture sizes ($\theta = 5 - 15'$) than it is in comparison to Hoekstra et al. (2011) results and to Gruen et al. (2011) results. This can be explained by the overdense region that the COSMOS field lies, which causes a higher cosmic shear signal (e.g. McCracken et al., 2007, which found higher clustering amplitudes in the COSMOS field than for other sky patches).

Since $\sigma_{\gamma_t}^{\text{LSS}} \sim 0.006$ and $\sigma_{e_i^s} \sim 0.33$ for our data, it is possible to calculate the number of galaxies N for which the LSS and intrinsic ellipticity noises reach the same order of importance. From equation (7.17) we can infer

$$\frac{\sigma_{e_i^s}^2}{N} = \sigma_{\gamma_t}^{\text{LSS}\,2} \tag{7.18}$$

yielding $N \sim 3000$. This corresponds to a density of ~ 26 galaxies arcmin^{-2} if an aperture of $6'$ is considered. Therefore, for a survey like the COSMOS, it is already possible to achieve the density of galaxies for which the LSS noise error becomes equal to the intrinsic ellipticity noise.
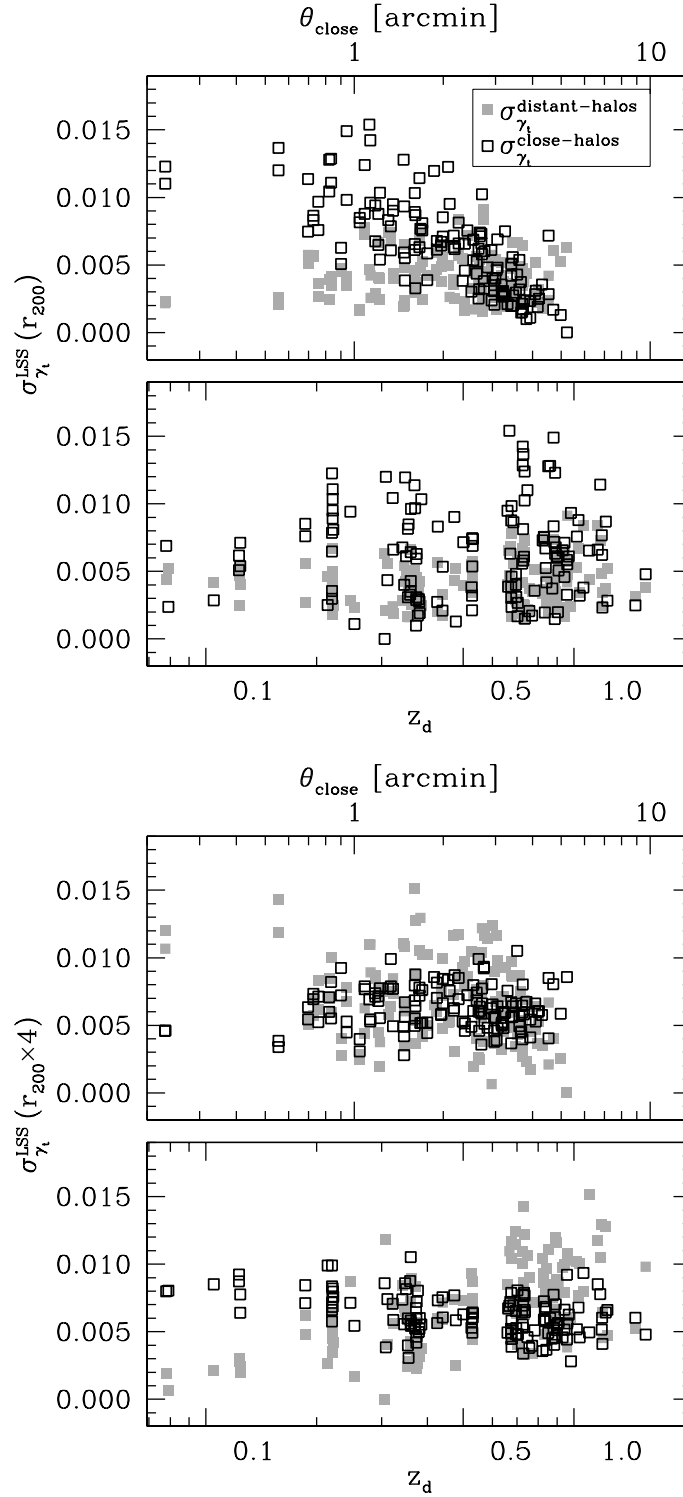
Figure 7.13: Dispersion in the averaged tangential shear measured within two radii: $R = r_{200}$ (upper) and $r_{200} \times 4$ (bottom). The dispersion is shown as a function of redshift of main lens z_d and as a function of distance to the nearest lens θ_{close}. The tangential shear dispersion introduced by halos that are close in projection to the main galaxy group is shown by the black open squares, whereas the tangential shear dispersion introduced by distant halos is shown by the filled gray squares. See the text for details.
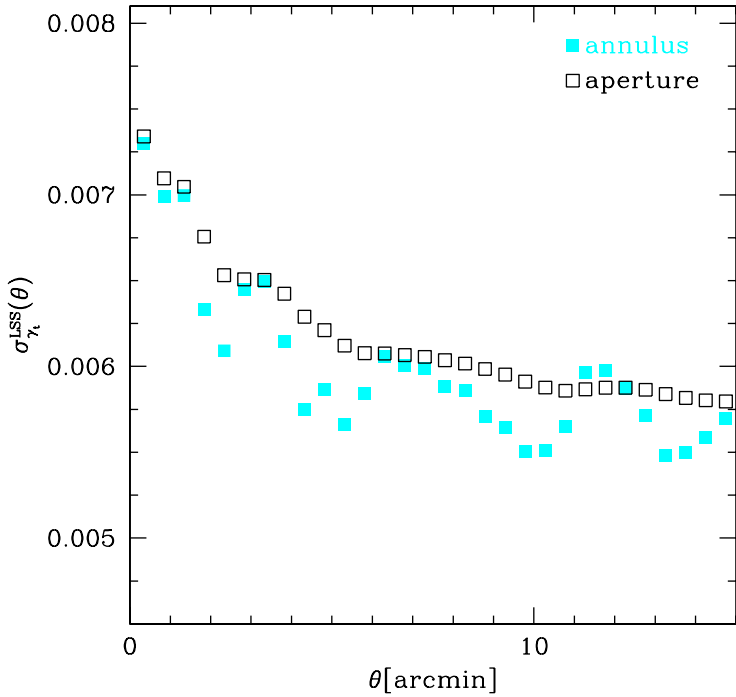
Figure 7.14: Dispersion of the azimuthally averaged tangential shear $\sigma_{\gamma_t}^{\mathrm{LSS}}$ as a function of the radius θ. The tangential shear is calculated relative to 100 random positions of the image. The black squares show measurements performed within circular apertures, for which the the aperture size is increased by $5'$. The cyan squares show the measurement performed within circular annuli, where the step-size between two annuli is also equals $5'$.

7.4   Density Contrast Profiles

In this section we present an analysis of the density contrast profiles of the galaxy groups of our sample.

As discussed in the Section 7.1, the detection of low mass systems via weak lensing is limited to shape noise contamination. One way to overcome this problem is by averaging the shear signal of several galaxy groups with similar properties. The density contrast $\Delta\Sigma(R)$ (Miralda-Escude, 1991) is an estimator often used to stack the shear profile of halos. It is defined as

$$\Delta\Sigma(R) \equiv \bar{\Sigma}(< R) - \langle\Sigma(R)\rangle = \gamma_{\mathrm{t}}(R) \times \Sigma_{crit}\,, \qquad (7.19)$$

where $\bar{\Sigma}(< R)$ is the mean surface density interior a radius R and $\langle\Sigma(R)\rangle$ is the azimuthal average of $\Sigma(R)$ at radius R. The critical density Σ_{crit} is given by equation (3.12). Since the tangential shear in equation (7.19) is multiplied by Σ_{crit}, the density contrast $\Delta\Sigma$ is a redshift independent quantity. The density contrast is related to the mass of the halo via

$$M(R) = \int_0^R \Sigma(R)dR^2 \sim \bar{\Sigma}(< R) \times \pi R^2\,, \qquad (7.20)$$

and therefore the M_{200} mass is given by

$$M_{200} = \pi r_{200}^2(\Delta\Sigma(r_{200}) + \langle\Sigma(r_{200})\rangle)\,. \qquad (7.21)$$

The surface mass density Σ as a function of the dimensionless radius $x = R/r_s$ for an

NFW profile is given by (Wright & Brainerd, 2000, see also Chapter 6):

$$\Sigma(x) = \begin{cases} \frac{2r_s\delta_c\rho_{crit}}{(x^2-1)}\left[1 - \frac{2}{\sqrt{(1-x^2)}}\text{atanh}\sqrt{(1-x)/(1+x)}\right] & \text{if} \quad x < 1, \\[3mm] \frac{2r_s\delta_c\rho_{crit}}{3} & \text{if} \quad x = 1, \\[3mm] \frac{2r_s\delta_c\rho_{crit}}{(x^2-1)}\left[1 - \frac{2}{\sqrt{(x^2-1)}}\arctan\sqrt{(x-1)/(1+x)}\right] & \text{if} \quad x > 1 \end{cases} \qquad (7.22)$$

The stacking technique has been adopted in the literature few times: Hoekstra et al. (2001) used CNOC2 data and made use of the shear signal of an ensemble of 50 groups at $z_d = 0.12 - 0.55$ and velocity dispersion ranging from $\sigma_v = 50 - 400$ km s^{-1}. The averaged velocity dispersion obtained from the stacked profiles was $\sigma_v = 274^{+48}_{-59}$ km s^{-1}. Parker et al. (2005) adopted the same technique as Hoekstra et al. (2001), but using a sample of 116 CNOC2 groups with median redshift of $z_d = 0.33$. Both works have stacked the tangential shear profile of groups, which is not a redshift independent quantity. A remarkable achievement was presented by Johnston et al. (2007) who did use the density contrast profile of 130,000 SLOAN systems between $z_d = 0.1 - 0.3$. The systems were divided in 12 bins of optical richness and 16 bins of i band luminosity. Then, an averaged density contrast was obtained for each bin. For the first time, the stacking technique of an ensemble of systems at higher redshifts was presented by Leauthaud et al. (2010). This study consisted of the analysis of 127 galaxy groups with $z_d \leq 1$, which were also selected from the COSMOS X-ray catalog. The galaxy groups were split in nine bins of redshift and X-ray luminosity. The obtained density contrast of each bin was used to estimate M_{200}, which was eventually used to derive a $L_{X(0.1-2.4\text{keV})}-M_{200}$ relation.

In this section, we also make use of the stacking technique to analyze the density contrast profiles of the galaxy groups in our sample. One disadvantage of this method is that, in order to constrain physical parameters of the systems investigated, it is necessary to average the density contrast of galaxy groups with similar properties. Hence, such properties should be known a priory (e.g. mass, richness, luminosity). We stack the lensing signal of the galaxy groups in our sample using the same binning system as proposed by Leauthaud et al. (2010). Table 7.2 shows the properties of the seven bins of redshift and X-ray luminosity used. Moreover, as it was done in Section 7.3, we also split the density contrast into the contribution originating from the main galaxy group to the contribution originating from the LSS (*close-* and *distant-halos* terms). If the latter is not zero, then mass estimates from the density contrast profiles are not reliable. Therefore, we study the density contrast profiles of the individual groups as well as the averaged density contrast profiles obtained from the ensembles of groups. We check how the contribution originating from the LSS affects the density contrast of the groups if they were isolated in the sky and the averaged density contrast obtained from the ensembles.

From equations (7.16) and (7.19), we can infer that the density contrast written in terms of the LSS components is given by

$$\Delta\Sigma^{\text{obs}}(R) = \Delta\Sigma^{\text{halo}}(R) + \Delta\Sigma^{\text{close-halos}}(R) + \Delta\Sigma^{\text{distant-halos}}(R) \qquad (7.23)$$

where the dividing line between *close-halos* and *distant-halos* is kept the same as in Section

7.3. The uncertainty of the measurement is given by

$$
\begin{aligned}
\sigma_{\Delta\Sigma}^{\mathrm{obs}\,2}(R) &= \sigma_{\Delta\Sigma}^{\mathrm{halo}\,2}(R) + \sigma_{\Delta\Sigma}^{\mathrm{close-halos}\,2}(R) + \sigma_{\Delta\Sigma}^{\mathrm{distant-halos}\,2}(R) \\
&= \Sigma_{cr}^2 \left[\frac{\sigma_{\mathbf{e}^s}^2}{2N} + \sigma_{\gamma_{\mathrm{t}}}^{\mathrm{close-halos}\,2}(R) + \sigma_{\gamma_{\mathrm{t}}}^{\mathrm{distant-halos}\,2}(R) \right]
\end{aligned} \tag{7.24}
$$

assuming that there are no errors on the redshift estimates.

Bin[a]	N_{halos}	z	M_{200} $[10^{13}\,\mathrm{M}_\odot]$	r_{200}^{b} [arcmin]	$L_{\mathrm{X}(0.1-2.4\mathrm{keV})}E(z)^{-1}$ $[10^{42}\,\mathrm{erg\,s^{-1}}]$	$\theta_{\mathrm{close}}^{\mathrm{c}}$ [arcmin]	Scale[d] $[10^{-3}\,\mathrm{kpc\,arcmin^{-1}}]$
A2	2	0.35	4.9	2.3	5.5	1.9	3.433
A3	8	0.36	2.5	1.8	2.0	2.7	3.370
A4	12	0.22	1.6	2.3	0.9	2.2	4.792
A5	15	0.36	1.7	1.6	1.1	2.2	3.370
A6	9	0.50	3.3	1.5	3.4	2.9	2.767
A7	24	0.70	3.4	1.2	4.1	2.2	2.352
A8	20	0.86	4.4	1.2	7.8	2.4	2.179

Table 7.2: Average properties of the binning system.

[a] Naming convention as used in Leauthaud et al. (2010). Bins named as A0 and A1 had no elements and were excluded from the table.
[b] Calculated using the averaged mass M_{200} and the adopted cosmology at the averaged redshift z.
[c] Calculated by averaging out the value θ_{close} of each group in a bin.
[d] Calculated using the averaged redshift and the adopted cosmology.

For this analysis we have also used the CFHT shear simulations due to larger sky coverage than the Subaru simulations. Using the isolated-pure-shear catalogs of each group, we compute the density contrast within an aperture for the three terms of the equation (7.23). In order to calculate the density contrast terms due to external halos, we proceed in a similar way to what we did in Section 7.3: (1) we identify the galaxy groups matching the *close-halos* and *distant-halos* criteria; (2) we compute the total shear of the *j*-th galaxy by summing (the shear) over all the groups classified as close and distant separately; (3) we calculate the tangential shear of each galaxy for the *close-halos* and *distant-halos* terms and; (4) we calculate the density contrast of each term using equation (7.19). Figure 7.15 illustrates the density contrast profiles originating from the three contributors (main, close, distant-halos) for a galaxy group in our sample (labeled with ID=142 in Table A).

The stacked density contrast profiles of each bin is calculated by averaging the density contrast profiles of all galaxy groups belonging to the bin. This is done for each term of equation (7.23) separately.

Next, the density contrast is measured for two aperture sizes: $R = r_{200}$ and $R = r_{200} \times 4$. Again, we have only used the groups for which the measured radii are fully inside the data field. Figure 7.16 shows the ratio of $\Delta\Sigma^{\mathrm{close-halos}}(R)$ and $\Delta\Sigma^{\mathrm{distant-halos}}(R)$ over $\Delta\Sigma^{\mathrm{halo}}(R)$ as a function of the redshift of main halo z_d and as a function of the projected distance to closest neighbor θ_{close}. The ratio can be either positive or negative. This happens because the shear field is perturbed by the extra lenses along the line-of-sight and, depending on the configuration of the lenses, the additional tangential shear can become negative or positive. The consequence of a negative value for the tangential shear is an underestimation of the parameters obtained from this quantity.

Figure 7.16 shows that, when measured within r_{200}, the contamination of the *close-halos* term scatters around zero, with an rms equals 0.15. However, there are several cases for which
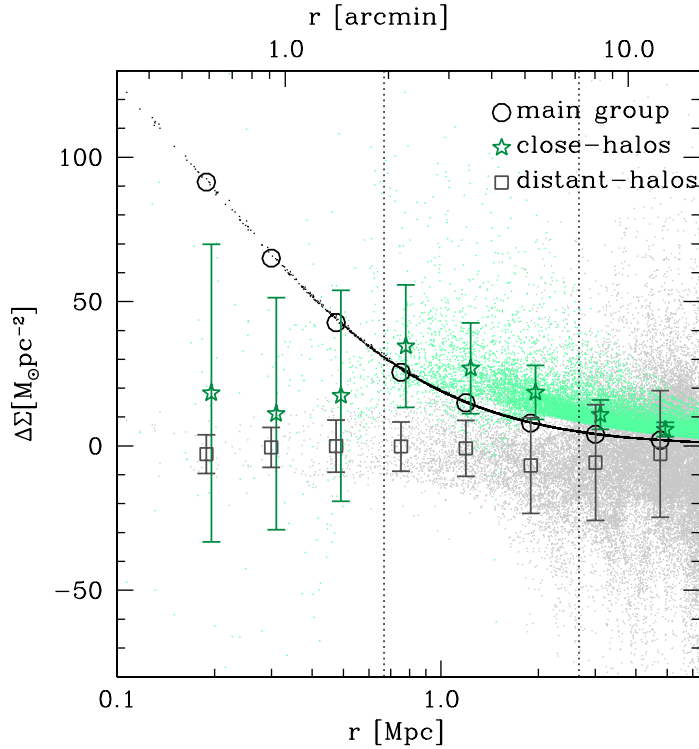
Figure 7.15: The density contrast profile of a test-case halo as a function of radius. The galaxy group shown in this plot is located at $z_d = 0.38$ and has $M_{200} = 5.13 \times 10^{13}\,M_\odot$ (ID=142 in Table A). Each tiny dot in the plot shows the density contrast value calculated for each background galaxy. The black dots show the density contrast of the main group, the light green dots show the values originating from the *close-halos* and the light gray dots from the *distant-halos*. To better visualize the contribution of each term, we overplot the density contrast profiles azimuthally averaged within eight bins. The azimuthally averaged profiles are shown by the big empty symbols with 1σ error bars: black circles show the azimuthally averaged profile of the main halo, the green stars show the azimuthally averaged profile originating from the *close-halos* and the gray squares from *distant-halos*. The error bars for the main group are not shown because they are too small. The vertical lines mark the positions of $r_{200} = 0.67$ Mpc and $r_{200} \times 4 = 2.68$ Mpc.

the contamination is of the order of 40% and for one case it reaches 100%. For the latter, the main galaxy group is located at high redshift and has a close galaxy group in projection ($\theta_{\rm close} < 1'$). On the other hand, the *distant-halos* term does not affect the density contrast estimate of the main galaxy group, with a mean value equal to zero (as expected) and an rms value of 0.06. This latter result is in agreement with Hoekstra (2001, 2003) findings. When the density contrast profile of several groups is stacked, the contamination of the *close-halos* term cancels out and the rms of the ratio drops to 0.07. This value is expected to drop even more if the stacking was performed over a larger number of galaxies groups within each bin. The rms of the *distant-halos* term is again consistent with zero when the stacking approach is considered. The measurements using a larger radius ($r_{200} \times 4$) show more scatter than within r_{200}. For both *close-halos* and *distant-halos* terms the mean values of the density contrast ratio are not zero and the rms value increases in comparison to measurements within r_{200}. The stacking technique does not help to decrease the rms value either. As it happened to the tangential shear dispersion measurements evaluated within $r_{200} \times 4$, the contribution of the terms *close-halos* and *distant-halos* are of the same order of importance. If the two terms are
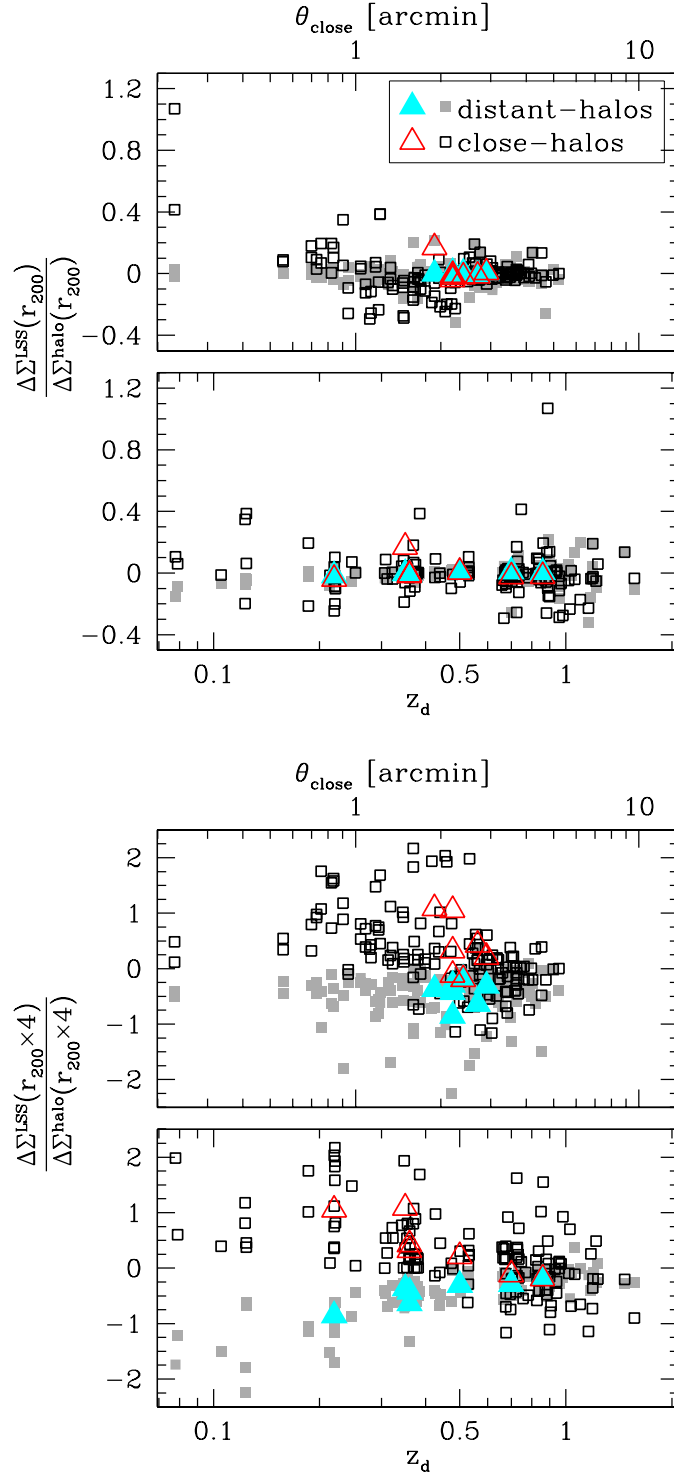
Figure 7.16: Contribution of the surrounding COSMOS halos to the estimated integrated density contrast of individual groups. The LSS terms of the density contrast is measured within $R = r_{200}$ (top) and $R = r_{200} \times 4$ (bottom) and divided by the integrated density contrast of the main group within same radii. In each plot the lowest panel show the ratio as a function of the redshift of the main galaxy group and the uppermost panel as a function of the projected distance to the closest neighbor. The ratio $\Delta\Sigma^{\text{close-halos}}(R)/\Delta\Sigma^{\text{halo}}(R)$ is shown by the black open squares, whereas the ratio $\Delta\Sigma^{\text{distant-halos}}(R)/\Delta\Sigma^{\text{halo}}(R)$ is shown by the filled gray squares. Triangles show the average values obtained by stacking the density contrast of several groups that are binned according to Table 7.2. Red open triangles show the ratio for *close-halos* and cyan triangles show the ratio for *distant-halos* of the averaged profiles.

R	Individual halo measurement		Stacked halo measurement	
	close-halos	*distant-halos*	*close-halos*	*distant-halos*
r_{200}	0.00	0.01	0.01	0.00
$r_{200} \times 4$	0.25	-0.43	0.40	-0.44

Table 7.3: Mean value of the ratio $\Delta\Sigma(R)^{\mathrm{LSS}}/\Delta\Sigma(R)^{\mathrm{halo}}$.

R	Individual halo measurement		Stacked halo measurement	
	close-halos	*distant-halos*	*close-halos*	*distant-halos*
r_{200}	0.15	0.06	0.07	0.01
$r_{200} \times 4$	0.72	0.58	0.62	0.49

Table 7.4: RMS of the ratio $\Delta\Sigma(R)^{\mathrm{LSS}}/\Delta\Sigma(R)^{\mathrm{halo}}$.

considered together, the mean value of the ratio $\Delta\Sigma(R)^{\mathrm{LSS}}/\Delta\Sigma(R)^{\mathrm{halo}}$ drops to zero, but the scatter remains high, around $\sim 55\%$.

Tables 7.3 and 7.4 summarize the mean and rms values of the ratios $\Delta\Sigma(R)^{\mathrm{LSS}}/\Delta\Sigma(R)^{\mathrm{halo}}$ considering the individual and stacking measurement scenario.

7.5 High Redshift Groups

Figure 7.16 demonstrates that the density contrast estimate can be biased by $\sim 100\%$ if the main lens is located at high redshift (high-z) and has another halo along the line-of-sight very close in projected distance ($\theta_{\mathrm{close}} < 1'$). In this section we briefly investigate the probability of finding such a configuration, considering that the COSMOS survey provides a representative distribution of halos in the sky.

We define high-z groups as the ones with $z_d \geq 0.8$, totaling 54 groups. In order to investigate the frequency of the high-z groups with close companions, we generate 1000 realizations of random positions for the groups in our sample. The groups are distributed within the same area as they are observed. For each realization and galaxy group, we calculate the projected distance of the nearest neighbor. Next, we evaluate the percentage of high-z groups with a companion within $1'$. We note that, the total number of high-z groups is kept fixed to all realizations, since the redshift distribution of the groups is not changed. Depending on the realization, the percentage of high-z groups with neighbors within $\theta_{\mathrm{close}} < 1'$ varies from 0 to 30%. On average, 13% of high-z groups have a another halo along the line-of-sight that is closer than $1'$. Figure 7.17 shows the distribution of this fraction for the 1000 random realizations of positions.

In order to understand why high-z groups have their shear signal contaminated by foreground masses more significantly than halos at intermediate redshifts, we recall the definition of the density contrast. Considering that the total shear observed is the sum of the shear introduced by the high-z halo $\gamma_{\mathrm{t}}^{\mathrm{high-z}}$ plus the shear introduced by a foreground halo $\gamma_{\mathrm{t}}^{\mathrm{fg}}$, we find the density contrast estimate equals
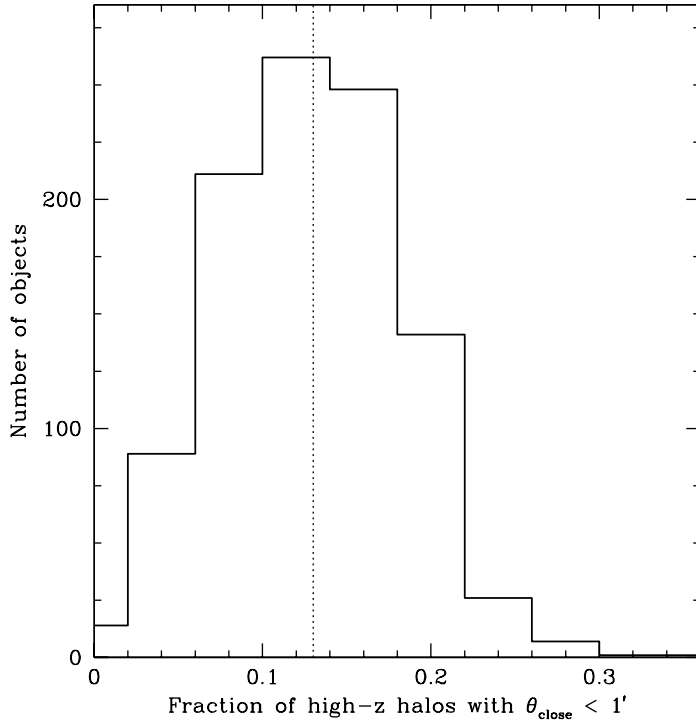
Figure 7.17: Distribution of the fraction of groups at $z_d \geq 0.8$ that have a neighbor within a distance $\theta_{\text{close}} < 1'$ over the total number of high-z groups. The distribution is drawn from 1000 realizations of random positions spread over the COSMOS field. From a total of 54 groups at $z_d \geq 0.8$ there is mean probability that $13\% \pm 5\%$ of the groups have a halo along the line-of-sight within $1'$.

$$
\begin{aligned}
\Delta\Sigma &= (\gamma_{\text{t}}^{\text{high}-z} + \gamma_{\text{t}}^{\text{fg}}) \times \Sigma_{crit}^{\text{high}-z} \\
&= \Delta\Sigma^{\text{high}-z} + \Delta\Sigma^{\text{fg}} \left(\frac{\Sigma_{crit}^{\text{high}-z}}{\Sigma_{crit}^{\text{fg}}} \right) .
\end{aligned}
\tag{7.25}
$$

The quantity $\Delta\Sigma^{\text{fg}}$ in the right-hand side of equation (7.25) is multiplied by the ratio between the critical density of the high-z halo and the critical density of foreground halo. For most of the cases this ratio is greater than one and hence the foreground halo contributes in a boosted way to the total $\Delta\Sigma$ budget. Figure 7.18 helps to understand this: since the critical density is proportional to $D_s/D_d D_{ds}$ we can analyze this factor as a function of the redshift of the halo z_d for fixed source population at redshift z_s. In Figure 7.18 we use three different redshifts values for the background sources: $z_s = 0.8$ which represents the median redshift of a shallow survey, $z_s = 1.0$ which is the median redshift of the galaxies found in this work and $z_s = 1.25$ which mimics the median redshift of background sources of high-z groups. The figure demonstrates that, for the three different source populations, halos at higher-z always have the factor $D_s/D_d D_{ds}$ higher than the halos at intermediate redshifts, meaning that the ratio $\Sigma_{crit}^{\text{high}-z}/\Sigma_{crit}^{\text{fg}} > 1$. The same happens to low-z halos ($z_d < 0.20$) as already previously noticed by Hoekstra (2001).
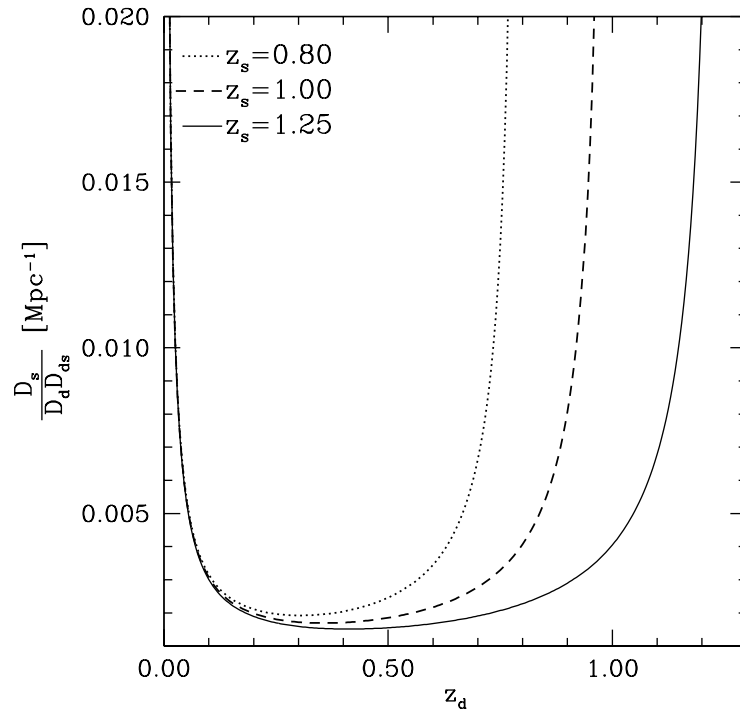
Figure 7.18: The factor $D_s/D_d D_{ds}$ as a function of the redshift of the lens for three different background populations, fixed at the redshifts: $z_s = 0.8$ (dotted line), $z_s = 1.0$ (dashed line) and $z_s = 1.25$ (solid line). The ratio $\Sigma_{crit}^{\text{high}-z}/\Sigma_{crit}^{\text{fg}}$ is equal to 2.3, 2.4, and 2.6, for a foreground lens at $z_d^{\text{fg}} = 0.35$ and the respective configurations: (1) source population at $z_s = 0.8$ and high-z lens at $z_d^{\text{high}-z} = 0.65$; (2) source population at $z_s = 1.0$ and high-z lens at $z_d^{\text{high}-z} = 0.80$; and (3) source population at $z_s = 1.25$ and high-z lens at $z_d^{\text{high}-z} = 1.00$.

Chapter 8

Summary and Conclusions

In the course of this thesis we have analyzed the shear signal of galaxy groups using 1 square degree of mock simulated data. We have shown how the close and distant galaxy groups observed in the field influence the weak lensing measurements of the individual groups. In particular, we have shown that galaxy groups at high redshifts are the most affected by the line-of-sight objects. We have also shown that shear field originating from all halos introduce an extra source of noise to the shear measurements of individual groups. The results of this thesis have been submitted to the Monthly Notices of the Royal Astronomical Society journal for a publication. Our main findings and methods are summarized in this chapter.

In Chapter 5 we derived the shear and photo-z catalogs using CFHT and Subaru observations of the COSMOS field, which were processed and reduced according to Chapter 4. The combined shear-photo-z catalogs resulted in a density of 29.7 and 21.7 galaxies arcmin^{-2} for the CFHT and Subaru, respectively. The two-component intrinsic ellipticity dispersion found was $\sigma_{\mathbf{e}^s} = 0.47$ and $\sigma_{\mathbf{e}^s} = 0.42$ for CFHT and Subaru. The final shear-photo-z catalogs plus the information on X-ray luminous galaxy groups found in the COSMOS field (Finoguenov et al. in preparation) were used as input to create shear mock catalogs, as described in Chapter 6. The shear field was calculated assuming that halos are described by an NFW density profile. Based on this, the distortion on the shape of the source galaxies due to each lens was calculated. Calculations taking into account the contribution of all lenses in the field were also computed. An intrinsic ellipticity distribution was randomly generated according to the observations and attributed to the source galaxies. Thus, a comparison between the shear signal of individual groups and the observed shear signal which is originating from all galaxy groups embedded in the field was established. This was the major part of this thesis which is contained in Chapter 7.

The two different data sets provide information that can be used to forecast results for future surveys, with a deeper or shallower strategy. The main conclusions of this thesis are:

- With both a CFHT and Subaru-like configuration, COSMOS-like groups can not be detected using the M_{ap} statistic approach, unless the intrinsic ellipticity acts cooperatively or a high-false detection rate is accepted.

- Positive and negative E and B-modes with $|\text{S/N}| \geq 3$ are likely to happen by accident for about ~ 200 positions out of 66820 investigated. Hence only S/N > 4 peaks, which happen with a probability < 0.01%, can be considered as safe.

- The filtering technique using optical plus weak lensing methods proposed in a recent paper by Bellagamba et al. (2011) is able to detect $\sim 7\%$ of total halos with almost no spurious detection, if the threshold for an optical plus weak lensing detection is S/N ≥ 4. For this technique, lower values of S/N increase the number of spurious detections as to $\sim 75\%$.

- If the COSMOS field provides a representative picture of the full sky, half of the X-ray detected groups have a neighbor (also detected in X-rays and with the mass characteristics as shown in Figure 5.1) within a distance of $\theta_{\text{close}} < 2.5'$.

- In spite of the low masses of COSMOS galaxy groups, their presence in the field can perturb the signal-to-noise ratio of another halo. The rms of the difference in signal-to-noise is $\Delta \text{S/N} \approx 15\% \times \sqrt{n_{gal}/30}$ when an aperture with optimal size for the group detection is used. One noticeable case shows a difference of $\sim 90\%$.

- The observed density contrast profile, often used as mass estimator, can also be affected by the presence of extra objects along the line-of-sight. When measured for individual groups within r_{200}, the average bias introduced by close halos in projection is zero with an rms value of $\sim 15\%$. Distant halos also introduce an average bias equal to zero but the rms is $\sim 6\%$. When the density contrast is measured inside a radius four times larger than r_{200}, the average bias originating from all extra groups together is still zero but the scatter increases to 55%. As expected, stacking the density contrast profile of several groups cancels out the biases introduced by close and distant halos.

- The shear signal originating from other halos than the main galaxy group introduces an uncertainty in the shear measurements that has to be added to the uncertainty from intrinsic ellipticity. The average value of the LSS uncertainty obtained from COSMOS halos is $\sigma_{\gamma_t}^{\text{LSS}} \sim 0.006$ per component, which corresponds to $\sim 1.8\%$ of the one component intrinsic ellipticity value.

- The LSS and intrinsic ellipticity noise have the same order of magnitude if there are shape measurements of $N \sim 3000$ galaxies within the aperture considered. Deep observations using current instruments can already achieve this density of galaxies and, therefore, the LSS error should be included in the total error budget.

- The tangential shear dispersion within randomly placed apertures of $\theta = 5 - 15'$ is about a factor of two higher than the value predicted in the works of Hoekstra et al. (2011) and Gruen et al. (2011). This can be explained by the overdense line-of-sight of the COSMOS field (cosmic variance). On the other hand, we show that the structures causing line-of-sight contamination up to $z_d = 1$ can be detected with deep X-ray observations and quantitatively modeled.

- High-z groups can have their shear signal more contaminated by foreground objects than groups at intermediate redshift. The crucial configuration is when there is a line-of-sight object within $1'$ from the center of the high-z galaxy group. Therefore, weak lensing study of low mass systems at high-z requires special attention regarding of the biases introduced by the LSS. From simulations, we concluded that on average 13% of groups at $z_d \geq 0.8$ have this configuration.

Our results are based on COSMOS ground-based observations but can be extended to other fields. The weak lensing study of galaxy groups can be favored by the wide-sky coverage of future surveys such as the Dark Energy Survey (DES)[1], the Large Synoptic Survey Telescope (LSST)[2] and the Kilo-Degree Survey (KIDS)[3], which will image more than 1,000 square degrees of the southern sky.

If deep observations and wide-sky coverage are available, then the study of individual groups is possible, though the contamination by near halos in projection has to be taken into account and modeled. With wide-sky coverage alone, we can extract the mean properties of ensembles of galaxy groups using the stacking technique of density contrast profiles, so that the contribution introduced by the large-scale structure is canceled out. Nevertheless, the uncertainty in the shear measurements introduced by the large-scale structure can not be eliminated and has to be taken into account in the total error budget.

---

[1]http://www.darkenergysurvey.org/
[2]http://www.lsst.org/lsst
[3]http://www.eso.org/sci/observing/policies/PublicSurveys/sciencePublicSurveys.html

Bibliography

Abell, G. O. 1958: *The Distribution of Rich Clusters of Galaxies.*, ApJS, 3, 211

Adelman-McCarthy, J. K., Agüeros, M. A., Allam, S. S., Allende Prieto, C., Anderson, K. S. J., Anderson, S. F., Annis, J., Bahcall, N. A., Bailer-Jones, C. A. L., Baldry, I. K., Barentine, J. C., et al. 2008: *The Sixth Data Release of the Sloan Digital Sky Survey*, ApJS, 175, 297

Albrecht, A., Bernstein, G., Cahn, R., Freedman, W. L., Hewitt, J., Hu, W., Huth, J., Kamionkowski, M., Kolb, E. W., Knox, L., Mather, J. C., et al. 2006: *Report of the Dark Energy Task Force*, ArXiv Astrophysics e-prints

Bartelmann, M. 1996: *Arcs from a universal dark-matter halo profile.*, A&A, 313, 697

Bartelmann, M. & Schneider, P. 2001: *Weak gravitational lensing*, Physics Reports, 340, 291

Bellagamba, F., Maturi, M., Hamana, T., Meneghetti, M., Miyazaki, S., & Moscardini, L. 2011: *Optimal filtering of optical and weak lensing data to search for galaxy clusters: application to the COSMOS field*, MNRAS, 217

Bender, R., Appenzeller, I., Böhm, A., Drory, N., Fricke, K. J., Gabasch, A., Heidt, J., Hopp, U., Jäger, K., Kümmel, M., Mehlert, D., et al. 2001: *The FORS Deep Field: Photometric Data and Photometric Redshifts*, in Deep Fields, ed. S. Cristiani, A. Renzini, & R. E. Williams, 96–+

Bertin, E. 2006: *Automatic Astrometric and Photometric Calibration with SCAMP*, in Astronomical Society of the Pacific Conference Series, Vol. 351, Astronomical Data Analysis Software and Systems XV, ed. C. Gabriel, C. Arviset, D. Ponz, & S. Enrique, 112–+

Bertin, E. & Arnouts, S. 1996: *SExtractor: Software for source extraction.*, A&AS, 117, 393

Birkinshaw, M. 1999: *The Sunyaev-Zel'dovich effect*, Physics Reports, 310, 97

Blandford, R. D., Saust, A. B., Brainerd, T. G., & Villumsen, J. V. 1991: *The distortion of distant galaxy images by large-scale structure*, MNRAS, 251, 600

Böhringer, H., Voges, W., Huchra, J. P., McLean, B., Giacconi, R., Rosati, P., Burg, R., Mader, J., Schuecker, P., Simiç, D., Komossa, S., et al. 2000: *The Northern ROSAT All-Sky (NORAS) Galaxy Cluster Survey. I. X-Ray Properties of Clusters Detected as Extended X-Ray Sources*, ApJS, 129, 435

Brainerd, T. G. 2010: *Multiple Weak Deflections in Galaxy-Galaxy Lensing*, ApJ, 713, 603

Brimioulle, F., Lerchster, M., Seitz, S., Bender, R., & Snigula, J. 2008: *Photometric redshifts for the CFHTLS-Wide*, ArXiv e-prints

Capak, P., Aussel, H., Ajiki, M., McCracken, H. J., Mobasher, B., Scoville, N., Shopbell, P., Taniguchi, Y., Thompson, D., Tribiano, S., Sasaki, S., et al. 2007: *The First Release COSMOS Optical and Near-IR Data and Catalog*, ApJS, 172, 99

Carlstrom, J. E., Holder, G. P., & Reese, E. D. 2002: *Cosmology with the Sunyaev-Zel'dovich Effect*, ARA&A, 40, 643

Cavaliere, A. & Fusco-Femiano, R. 1976: *X-rays from hot plasma in clusters of galaxies*, A&A, 49, 137

Clowe, D., Bradač, M., Gonzalez, A. H., Markevitch, M., Randall, S. W., Jones, C., & Zaritsky, D. 2006: *A Direct Empirical Proof of the Existence of Dark Matter*, ApJ, 648, L109

Colley, W. N., Schild, R. E., Abajas, C., Alcalde, D., Aslan, Z., Bikmaev, I., Chavushyan, V., Chinarro, L., Cournoyer, J., Crowe, R., Dudinov, V., et al. 2003: *Around-the-Clock Observations of the Q0957+561A,B Gravitationally Lensed Quasar. II. Results for the Second Observing Season*, ApJ, 587, 71

Courbin, F. & Minniti, D., eds. 2002, Lecture Notes in Physics, Berlin Springer Verlag, Vol. 608, Gravitational Lensing: An Astrophysical Tool

de Blok, W. J. G., McGaugh, S. S., & Rubin, V. C. 2001: *High-Resolution Rotation Curves of Low Surface Brightness Galaxies. II. Mass Models*, AJ, 122, 2396

Dodelson, S. 2003, Modern cosmology, ed. Dodelson, S.

Duffy, A. R., Schaye, J., Kay, S. T., & Dalla Vecchia, C. 2008: *Dark matter halo concentrations in the Wilkinson Microwave Anisotropy Probe year 5 cosmology*, MNRAS, 390, L64

Ebeling, H., Edge, A. C., Bohringer, H., Allen, S. W., Crawford, C. S., Fabian, A. C., Voges, W., & Huchra, J. P. 1998: *The ROSAT Brightest Cluster Sample - I. The compilation of the sample and the cluster log N-log S distribution*, MNRAS, 301, 881

Einstein, A. 1916: *Die Grundlage der allgemeinen Relativitätstheorie*, Annalen der Physik, 354, 769

Eke, V. R., Cole, S., & Frenk, C. S. 1996: *Cluster evolution as a diagnostic for Omega*, MNRAS, 282, 263

Erben, T., Hildebrandt, H., Lerchster, M., Hudelot, P., Benjamin, J., van Waerbeke, L., Schrabback, T., Brimioulle, F., Cordes, O., Dietrich, J. P., Holhjem, K., et al. 2009: *CARS: the CFHTLS-Archive-Research Survey. I. Five-band multi-colour data from 37 sq. deg. CFHTLS-wide observations*, A&A, 493, 1197

Erben, T., Schirmer, M., Dietrich, J. P., Cordes, O., Haberzettl, L., Hetterscheidt, M., Hilde-brandt, H., Schmithuesen, O., Schneider, P., Simon, P., Deul, E., et al. 2005: *GaBoDS: The Garching-Bonn Deep Survey. IV. Methods for the image reduction of multi-chip cameras demonstrated on data from the ESO Wide-Field Imager*, Astronomische Nachrichten, 326, 432

Erben, T., Van Waerbeke, L., Bertin, E., Mellier, Y., & Schneider, P. 2001: *How accurately can we measure weak gravitational shear?*, A&A, 366, 717

Fassnacht, C. D., Xanthopoulos, E., Koopmans, L. V. E., & Rusin, D. 2002: *A Determination of H_0 with the CLASS Gravitational Lens B1608+656. III. A Significant Improvement in the Precision of the Time Delay Measurements*, ApJ, 581, 823

Finoguenov, A., Guzzo, L., Hasinger, G., Scoville, N. Z., Aussel, H., Böhringer, H., Brusa, M., Capak, P., Cappelluti, N., Comastri, A., Giodini, S., et al. 2007: *The XMM-Newton Wide-Field Survey in the COSMOS Field: Statistical Properties of Clusters of Galaxies*, ApJS, 172, 182

Friedman, A. 1922: *Über die Krümmung des Raumes*, Zeitschrift fur Physik, 10, 377

Gabasch, A., Bender, R., Seitz, S., Hopp, U., Saglia, R. P., Feulner, G., Snigula, J., Drory, N., Appenzeller, I., Heidt, J., Mehlert, D., et al. 2004a: *The evolution of the luminosity functions in the FORS Deep Field from low to high redshift. I. The blue bands*, A&A, 421, 41

Gabasch, A., Goranova, Y., Hopp, U., Noll, S., & Pannella, M. 2008: *A deep i-selected multiwaveband galaxy catalogue in the COSMOS field*, MNRAS, 383, 1319

Gabasch, A., Salvato, M., Saglia, R. P., Bender, R., Hopp, U., Seitz, S., Feulner, G., Pannella, M., Drory, N., Schirmer, M., & Erben, T. 2004b: *The Star Formation Rate History in the FORS Deep and GOODS-South Fields*, ApJ, 616, L83

Gavazzi, R. & Soucail, G. 2007: *Weak lensing survey of galaxy clusters in the CFHTLS Deep*, A&A, 462, 459

Giodini, S., Pierini, D., Finoguenov, A., Pratt, G. W., Boehringer, H., Leauthaud, A., Guzzo, L., Aussel, H., Bolzonella, M., Capak, P., Elvis, M., et al. 2009: *Stellar and Total Baryon Mass Fractions in Groups and Clusters Since Redshift 1*, ApJ, 703, 982

Gladders, M. D. & Yee, H. K. C. 2000: *A New Method For Galaxy Cluster Detection. I. The Algorithm*, AJ, 120, 2148

Gruen, D., Bernstein, G. M., Lam, T. Y., & Seitz, S. 2011: *Optimizing weak lensing mass estimates for cluster profile uncertainty*, ArXiv e-prints

Hamana, T., Takada, M., & Yoshida, N. 2004: *Searching for massive clusters in weak lensing surveys*, MNRAS, 350, 893

Hetterscheidt, M., Erben, T., Schneider, P., Maoli, R., van Waerbeke, L., & Mellier, Y. 2005: *Searching for galaxy clusters using the aperture mass statistics in 50 VLT fields*, A&A, 442, 43

Heymans, C., Van Waerbeke, L., Bacon, D., Berge, J., Bernstein, G., Bertin, E., Bridle, S., Brown, M. L., Clowe, D., Dahle, H., Erben, T., et al. 2006: *The Shear Testing Programme - I. Weak lensing analysis of simulated ground-based observations*, MNRAS, 368, 1323

Hildebrandt, H., Pielorz, J., Erben, T., Schneider, P., Eifler, T., Simon, P., & Dietrich, J. P. 2007: *GaBoDS: the Garching-Bonn deep survey. VIII. Lyman-break galaxies in the ESO deep public survey*, A&A, 462, 865

Hinshaw, G., Weiland, J. L., Hill, R. S., Odegard, N., Larson, D., Bennett, C. L., Dunkley, J., Gold, B., Greason, M. R., Jarosik, N., Komatsu, E., et al. 2009: *Five-Year Wilkinson Microwave Anisotropy Probe Observations: Data Processing, Sky Maps, and Basic Results*, ApJS, 180, 225

Hoekstra, H. 2001: *The effect of distant large scale structure on weak lensing mass estimates*, A&A, 370, 743

Hoekstra, H. 2003: *How well can we determine cluster mass profiles from weak lensing?*, MNRAS, 339, 1155

Hoekstra, H., Franx, M., Kuijken, K., Carlberg, R. G., Yee, H. K. C., Lin, H., Morris, S. L., Hall, P. B., Patton, D. R., Sawicki, M., & Wirth, G. D. 2001: *Weak-Lensing Study of Low-Mass Galaxy Groups: Implications for Ω_m*, ApJ, 548, L5

Hoekstra, H., Franx, M., Kuijken, K., & Squires, G. 1998: *Weak Lensing Analysis of CL 1358+62 Using Hubble Space Telescope Observations*, ApJ, 504, 636

Hoekstra, H., Hartlap, J., Hilbert, S., & van Uitert, E. 2011: *Effects of distant large-scale structure on the precision of weak lensing mass measurements*, MNRAS, 412, 2095

Ilbert, O., Arnouts, S., McCracken, H. J., Bolzonella, M., Bertin, E., Le Fèvre, O., Mellier, Y., Zamorani, G., Pellò, R., Iovino, A., Tresse, L., et al. 2006: *Accurate photometric redshifts for the CFHT legacy survey calibrated using the VIMOS VLT deep survey*, A&A, 457, 841

Ilbert, O., Capak, P., Salvato, M., Aussel, H., McCracken, H. J., Sanders, D. B., Scoville, N., Kartaltepe, J., Arnouts, S., Le Floc'h, E., Mobasher, B., et al. 2009: *Cosmos Photometric Redshifts with 30-Bands for 2-deg^2*, ApJ, 690, 1236

Janiak, A. 2009, in The Stanford Encyclopedia of Philosophy, winter 2009 edn., ed. E. N. Zalta

Johnston, D. E., Sheldon, E. S., Wechsler, R. H., Rozo, E., Koester, B. P., Frieman, J. A., McKay, T. A., Evrard, A. E., Becker, M. R., & Annis, J. 2007: *Cross-correlation Weak Lensing of SDSS galaxy Clusters II: Cluster Density Profiles and the Mass–Richness Relation*, ArXiv e-prints

Kaiser, N. 1986: *Evolution and clustering of rich clusters*, MNRAS, 222, 323

Kaiser, N., Squires, G., & Broadhurst, T. 1995: *A Method for Weak Lensing Observations*, ApJ, 449, 460

Kasliwal, M. M., Massey, R., Ellis, R. S., Miyazaki, S., & Rhodes, J. 2008: *A Comparison of Weak-Lensing Measurements from Ground- and Space-Based Facilities*, ApJ, 684, 34

Klypin, A., Zhao, H., & Somerville, R. S. 2002: *ΛCDM-based Models for the Milky Way and M31. I. Dynamical Models*, ApJ, 573, 597

Komatsu, E., Dunkley, J., Nolta, M. R., Bennett, C. L., Gold, B., Hinshaw, G., Jarosik, N., Larson, D., Limon, M., Page, L., Spergel, D. N., et al. 2009: *Five-Year Wilkinson Microwave Anisotropy Probe Observations: Cosmological Interpretation*, ApJS, 180, 330

Koopmans, L. V. E. & Treu, T. 2003: *The Structure and Dynamics of Luminous and Dark Matter in the Early-Type Lens Galaxy of 0047-281 at z = 0.485*, ApJ, 583, 606

Leauthaud, A., Finoguenov, A., Kneib, J., Taylor, J. E., Massey, R., Rhodes, J., Ilbert, O., Bundy, K., Tinker, J., George, M. R., Capak, P., et al. 2010: *A Weak Lensing Study of X-ray Groups in the Cosmos Survey: Form and Evolution of the Mass-Luminosity Relation*, ApJ, 709, 97

Leauthaud, A., Massey, R., Kneib, J., Rhodes, J., Johnston, D. E., Capak, P., Heymans, C., Ellis, R. S., Koekemoer, A. M., Le Fèvre, O., Mellier, Y., et al. 2007: *Weak Gravitational Lensing with COSMOS: Galaxy Selection and Shape Measurements*, ApJS, 172, 219

Lerchster, M., Seitz, S., Brimioulle, F., Fassbender, R., Rovilos, M., Böhringer, H., Pierini, D., Kilbinger, M., Finoguenov, A., Quintana, H., & Bender, R. 2011: *The massive galaxy cluster XMMU J1230.3+1339 at z∼1: colour-magnitude relation, Butcher-Oemler effect, X-ray and weak lensing mass estimates*, MNRAS, 411, 2667

Lilly, S. J., Le Fèvre, O., Renzini, A., Zamorani, G., Scodeggio, M., Contini, T., Carollo, C. M., Hasinger, G., Kneib, J., Iovino, A., Le Brun, V., et al. 2007: *zCOSMOS: A Large VLT/VIMOS Redshift Survey Covering 0¡z¡3 in the COSMOS Field*, ApJS, 172, 70

Luppino, G. A. & Kaiser, N. 1997: *Detection of Weak Lensing by a Cluster of Galaxies at Z = 0.83*, ApJ, 475, 20

Markevitch, M. 1998: *The L X-T Relation and Temperature Function for Nearby Clusters Revisited*, ApJ, 504, 27

Marmo, C. & Bertin, E. 2008: *MissFITS and WeightWatcher: Two Optimised Tools for Managing FITS Data.*, in Astronomical Society of the Pacific Conference Series, Vol. 394, Astronomical Data Analysis Software and Systems XVII, ed. R. W. Argyle, P. S. Bunclark, & J. R. Lewis, 619–+

Maturi, M., Angrick, C., Pace, F., & Bartelmann, M. 2010: *An analytic approach to number counts of weak-lensing peak detections*, A&A, 519, A23+

Maturi, M., Meneghetti, M., Bartelmann, M., Dolag, K., & Moscardini, L. 2005: *An optimal filter for the detection of galaxy clusters through weak lensing*, A&A, 442, 851

McCracken, H. J., Peacock, J. A., Guzzo, L., Capak, P., Porciani, C., Scoville, N., Aussel, H., Finoguenov, A., James, J. B., Kitzbichler, M. G., Koekemoer, A., et al. 2007: *The Angular Correlations of Galaxies in the COSMOS Field*, ApJS, 172, 314

Miralda-Escude, J. 1991: *Gravitational lensing by clusters of galaxies - Constraining the mass distribution*, ApJ, 370, 1

Miyazaki, S., Hamana, T., Ellis, R. S., Kashikawa, N., Massey, R. J., Taylor, J., & Refregier, A. 2007: *A Subaru Weak-Lensing Survey. I. Cluster Candidates and Spectroscopic Verification*, ApJ, 669, 714

Murdin, P. 2001, Encyclopedia of astronomy and astrophysics, ed. Murdin, P.

Natarajan, P., ed. 2002, The Shapes of Galaxies and Their Dark Halos

Navarro, J. F., Frenk, C. S., & White, S. D. M. 1997: *A Universal Density Profile from Hierarchical Clustering*, ApJ, 490, 493

Ouchi, M., Shimasaku, K., Okamura, S., Furusawa, H., Kashikawa, N., Ota, K., Doi, M., Hamabe, M., Kimura, M., Komiyama, Y., Miyazaki, M., et al. 2004: *Subaru Deep Survey. V. A Census of Lyman Break Galaxies at z˜=4 and 5 in the Subaru Deep Fields: Photometric Properties*, ApJ, 611, 660

Parker, L. C., Hudson, M. J., Carlberg, R. G., & Hoekstra, H. 2005: *Mass-to-Light Ratios of Galaxy Groups from Weak Lensing*, ApJ, 634, 806

Peebles, P. J. & Ratra, B. 2003: *The cosmological constant and dark energy*, Reviews of Modern Physics, 75, 559

Perlmutter, S., Aldering, G., Goldhaber, G., Knop, R. A., Nugent, P., Castro, P. G., Deustua, S., Fabbro, S., Goobar, A., Groom, D. E., Hook, I. M., et al. 1999: *Measurements of Omega and Lambda from 42 High-Redshift Supernovae*, ApJ, 517, 565

Postman, M., Lubin, L. M., Gunn, J. E., Oke, J. B., Hoessel, J. G., Schneider, D. P., & Christensen, J. A. 1996: *The Palomar Distant Clusters Survey. I. The Cluster Catalog*, AJ, 111, 615

Press, W. H. 2002, Numerical recipes in C++ : the art of scientific computing, ed. Press, W. H.

Reiprich, T. H. & Böhringer, H. 2002: *The Mass Function of an X-Ray Flux-limited Sample of Galaxy Clusters*, ApJ, 567, 716

Riess, A. G., Filippenko, A. V., Challis, P., Clocchiatti, A., Diercks, A., Garnavich, P. M., Gilliland, R. L., Hogan, C. J., Jha, S., Kirshner, R. P., Leibundgut, B., et al. 1998: *Observational Evidence from Supernovae for an Accelerating Universe and a Cosmological Constant*, AJ, 116, 1009

Riffeser, A., Seitz, S., & Bender, R. 2008: *The M31 Microlensing Event WeCAPP-GL1/POINT-AGAPE-S3: Evidence for a MACHO Component in the Dark Halo of M31?*, ApJ, 684, 1093

Rosati, P., Borgani, S., & Norman, C. 2002: *The Evolution of X-ray Clusters of Galaxies*, ARA&A, 40, 539

Rowe, B. 2010: *Improving PSF modelling for weak gravitational lensing using new methods in model selection*, MNRAS, 404, 350

Rubin, V. C., Ford, W. K. J., & . Thonnard, N. 1980: *Rotational properties of 21 SC galaxies with a large range of luminosities and radii, from NGC 4605 /R = 4kpc/ to UGC 2885 /R = 122 kpc/,* ApJ, 238, 471

Salucci, P. & Burkert, A. 2000: *Dark Matter Scaling Relations,* ApJ, 537, L9

Saviane, I., Ivanov, V. D., & Borissova, J., eds. 2007, Groups of Galaxies in the Nearby Universe

Schirmer, M. 2004, in PhD thesis, ed. U. Bonn

Schirmer, M., Erben, T., Hetterscheidt, M., & Schneider, P. 2007: *GaBoDS: the Garching-Bonn Deep Survey. IX. A sample of 158 shear-selected mass concentration candidates,* A&A, 462, 875

Schneider, P. 1996: *Detection of (dark) matter concentrations via weak gravitational lensing,* MNRAS, 283, 837

Schneider, P., Kochanek, C. S., & Wambsganss, J. 2006, Gravitational Lensing: Strong, Weak and Micro, ed. Schneider, P., Kochanek, C. S., & Wambsganss, J.

Schneider, P. & Seitz, C. 1995: *Steps towards nonlinear cluster inversion through gravitational distortions. 1: Basic considerations and circular clusters,* A&A, 294, 411

Schneider, P., van Waerbeke, L., Jain, B., & Kruse, G. 1998: *A new measure for cosmic shear,* MNRAS, 296, 873

Schrabback, T., Erben, T., Simon, P., Miralles, J., Schneider, P., Heymans, C., Eifler, T., Fosbury, R. A. E., Freudling, W., Hetterscheidt, M., Hildebrandt, H., et al. 2007: *Cosmic shear analysis of archival HST/ACS data. I. Comparison of early ACS pure parallel data to the HST/GEMS survey,* A&A, 468, 823

Schrabback, T., Hartlap, J., Joachimi, B., Kilbinger, M., Simon, P., Benabed, K., Bradač, M., Eifler, T., Erben, T., Fassnacht, C. D., High, F. W., et al. 2010: *Evidence of the accelerated expansion of the Universe from weak lensing tomography with COSMOS,* A&A, 516, A63+

Schramm, T. & Kayser, R. 1995: *The complex theory of gravitational lensing. Beltrami equation and cluster lensing.,* A&A, 299, 1

Scoville, N., Aussel, H., Brusa, M., Capak, P., Carollo, C. M., Elvis, M., Giavalisco, M., Guzzo, L., Hasinger, G., Impey, C., Kneib, J., et al. 2007: *The Cosmic Evolution Survey (COSMOS): Overview,* ApJS, 172, 1

Seitz, C. & Schneider, P. 1995: *Steps towards nonlinear cluster inversion through gravitational distortions II. Generalization of the Kaiser and Squires method.,* A&A, 297, 287

Seitz, C. & Schneider, P. 1997: *Steps towards nonlinear cluster inversion through gravitational distortions. III. Including a redshift distribution of the sources.,* A&A, 318, 687

Serjeant, S. 2010, Observational Cosmology, ed. Serjeant, S.

Sofue, Y. & Rubin, V. 2001: *Rotation Curves of Spiral Galaxies,* ARA&A, 39, 137

Struble, M. F. & Rood, H. J. 1999: *A Compilation of Redshifts and Velocity Dispersions for ACO Clusters*, ApJS, 125, 35

Sunyaev, R. A. & Zeldovich, I. B. 1980: *Microwave background radiation as a probe of the contemporary structure and history of the universe*, 18, 537

Taniguchi, Y., Scoville, N., Murayama, T., Sanders, D. B., Mobasher, B., Aussel, H., Capak, P., Ajiki, M., Miyazaki, S., Komiyama, Y., Shioya, Y., et al. 2007: *The Cosmic Evolution Survey (COSMOS): Subaru Observations of the HST Cosmos Field*, ApJS, 172, 9

Umetsu, K., Medezinski, E., Broadhurst, T., Zitrin, A., Okabe, N., Hsieh, B.-C., & Molnar, S. M. 2010: *The Mass Structure of the Galaxy Cluster Cl0024+1654 from a Full Lensing Analysis of Joint Subaru and ACS/NIC3 Observations*, ApJ, 714, 1470

van Paradijs, J. & Bleeker, J. A. M., eds. 1999, Lecture Notes in Physics, Berlin Springer Verlag, Vol. 520, X-Ray Spectroscopy in Astrophysics

Walsh, D., Carswell, R. F., & Weymann, R. J. 1979: *0957 + 561 A, B - Twin quasistellar objects or gravitational lens*, Nat, 279, 381

Wright, C. O. & Brainerd, T. G. 2000: *Gravitational Lensing by NFW Halos*, ApJ, 534, 34

Yagi, M., Kashikawa, N., Sekiguchi, M., Doi, M., Yasuda, N., Shimasaku, K., & Okamura, S. 2002: *Luminosity Functions of 10 Nearby Clusters of Galaxies. I. Data*, AJ, 123, 66

Zwicky, F. 1937: *On the Masses of Nebulae and of Clusters of Nebulae*, ApJ, 86, 217

Group Catalog

This appendix lists the group catalog, which was selected from the COSMOS X-ray catalog of extended sources from Finoguenov et al., in preparation. Only groups lying in the CFHTLS-D2 field were selected, totaling 165 systems. Our group sample is characterized by a median mass of $M_{200} = 3.1 \times 10^{13} \, M_{\odot}$ and median redshift of $z = 0.68$.

The X-ray derived parameters are described in Section 5.1 of Chapter 5. Other parameters listed in the table which were derived specifically for this work are followed with a reference of where they are found in this thesis.

Table A.1: Catalog of selected galaxy groups taken from the COSMOS X-ray catalog of extended sources (Finoguenov et al., in preparation). Columns (1): Galaxy group ID; (2) and (3): Galaxy group coordinates in units of degrees (see Section 5.1 of Chapter 5 for further information); (4) Redshift; (5) M_{200} mass estimate in units of $10^{13} \, M_{\odot}$; (6) Apparent X-ray luminosity in the 0.1-2.4 keV band, in units of $10^{42} \, \mathrm{erg\,s^{-1}}$; (7) K-correction; (8) Extrapolated flux in the 0.5–2 keV band within r_{500}, in units of $10^{-14} \, \mathrm{erg\,s^{-1}\,cm^{-2}}$; (9) Estimated gas temperature in keV; (10) and (11) Estimated radius r_{200} in kiloparsecs and arcminutes (derived from the equation 6.2); (12) Angular distance in units of megaparsecs (derived from the equation 2.22); (13) Concentration c_{200} parameter derived from the $c_{200}(M_{200}, z_d)$ relation from Duffy et al. (2008) (calculated from the equation 6.4); (14) Conversion factor from kiloparsec to arcminute and; (14) Projected distance of the closest neighboring halo in units of arcminutes.

Table A.1

ID	R.A. [degree]	Dec. [degree]	z	M_{200} [$10^{13}\,M_\odot$]	$L_{X(0.1-2.4\text{keV})}$ [$10^{42}\,\text{erg s}^{-1}$]	K_{corr}	Flux [$10^{-14}\,\text{erg s}^{-1}\,\text{cm}^{-2}$]	T [keV]	r_{200} [kpc]	r_{200} [arcmin]	D_d [Mpc]	c_{200}	Scale [$10^{-3}\,\text{kpc arcmin}^{-1}$]	θ_{close} [arcmin]
(1)	(2)	(3)	(4)	(5)	(6)	(7)	(8)	(9)	(10)	(11)	(12)	(13)	(14)	(15)
1	149.85146	1.77319	0.124	4.09 ± 0.08	3.72 ± 0.12	1.58	6.027	0.95 ± 0.01	673.9	5.2	448.0	4.3	7.673	2.7
2	150.17996	1.76887	0.344	5.97 ± 0.22	8.76 ± 0.51	1.65	1.366	1.27 ± 0.03	712.6	2.5	989.9	3.8	3.473	3.6
3	150.25397	1.77215	0.527	2.09 ± 0.64	2.17 ± 1.11	1.88	0.107	0.73 ± 0.11	471.0	1.3	1278.0	3.9	2.690	2.3
4	150.49509	1.79411	0.958	6.47 ± 0.73	23.13 ± 4.23	1.82	0.269	1.65 ± 0.12	585.2	1.2	1629.5	3.2	2.110	2.7
5	150.23296	1.73957	0.980	3.78 ± 0.78	10.29 ± 3.50	2.27	0.091	1.18 ± 0.15	485.2	1.0	1639.5	3.3	2.097	2.3
6	150.20660	1.82327	0.530	4.04 ± 0.38	6.07 ± 0.92	1.75	0.319	1.06 ± 0.06	585.8	1.6	1281.8	3.7	2.682	3.6
7	149.89491	1.76497	0.531	3.79 ± 0.51	5.52 ± 1.20	1.76	0.286	1.02 ± 0.08	573.5	1.5	1283.1	3.8	2.679	2.7
8	149.82381	1.82527	0.531	3.54 ± 0.43	4.96 ± 0.98	1.77	0.255	0.98 ± 0.07	560.6	1.5	1283.1	3.8	2.679	3.0
9	150.41386	1.84759	0.969	7.56 ± 0.57	29.88 ± 3.62	1.75	0.352	1.83 ± 0.09	613.7	1.3	1634.5	3.1	2.103	2.9
10	149.93111	1.83463	0.530	2.53 ± 0.45	2.93 ± 0.86	1.82	0.147	0.81 ± 0.08	501.4	1.3	1281.8	3.9	2.682	0.7
11	150.52682	1.82698	1.061	4.99 ± 0.83	17.80 ± 4.81	2.07	0.141	1.45 ± 0.15	516.7	1.1	1671.6	3.2	2.057	2.7
12	149.80055	1.87037	1.567	6.31 ± 0.98	50.40 ± 12.77	2.07	0.149	2.00 ± 0.20	467.9	0.9	1757.2	2.8	1.956	3.0
13	150.25089	1.86400	0.529	2.91 ± 0.46	3.65 ± 0.94	1.80	0.186	0.87 ± 0.08	525.6	1.4	1280.6	3.8	2.685	3.6
14	150.44704	1.88285	0.671	4.31 ± 0.48	8.19 ± 1.46	1.82	0.231	1.15 ± 0.08	568.6	1.4	1435.6	3.6	2.395	1.7
15	150.57919	1.93556	0.469	5.73 ± 0.47	9.65 ± 1.27	1.69	0.709	1.29 ± 0.07	672.9	1.9	1198.9	3.7	2.867	6.8
16	150.45126	1.91018	1.179	6.22 ± 0.76	29.53 ± 5.86	1.98	0.187	1.74 ± 0.14	532.8	1.1	1707.1	3.0	2.014	1.7
17	150.12570	1.91369	0.736	3.18 ± 0.62	5.57 ± 1.80	2.00	0.114	0.98 ± 0.11	501.4	1.2	1491.6	3.6	2.305	3.7
18	150.35332	1.93337	1.233	5.10 ± 0.79	22.95 ± 5.76	2.25	0.117	1.55 ± 0.15	488.9	1.0	1719.6	3.1	1.999	4.1
19	150.19829	1.98628	0.439	3.21 ± 0.28	3.76 ± 0.53	1.70	0.319	0.90 ± 0.05	560.7	1.7	1153.8	3.9	2.979	3.3
20	150.42012	1.97080	0.862	2.69 ± 0.93	5.15 ± 3.03	2.40	0.058	0.93 ± 0.18	452.8	1.0	1578.8	3.5	2.177	0.8
21	150.36931	1.99949	0.829	4.78 ± 0.60	11.99 ± 2.44	1.88	0.193	1.30 ± 0.10	554.7	1.2	1558.4	3.4	2.206	3.2
22	150.10081	2.01119	0.222	1.76 ± 0.15	1.11 ± 0.15	1.61	0.492	0.61 ± 0.03	493.4	2.3	722.3	4.5	4.759	1.7
23	149.82365	2.01304	0.253	1.53 ± 0.20	0.92 ± 0.20	1.64	0.306	0.57 ± 0.04	466.1	2.0	797.3	4.5	4.312	3.9
24	150.05878	2.00911	0.078	0.62 ± 0.16	0.18 ± 0.08	1.73	0.727	0.38 ± 0.03	363.7	4.2	296.7	5.2	1.159	2.5
25	150.42249	2.00891	0.851	5.12 ± 0.70	13.81 ± 3.08	1.86	0.209	1.37 ± 0.12	562.9	1.2	1572.2	3.3	2.187	1.5
26	150.31282	2.00902	0.311	2.16 ± 0.22	1.71 ± 0.28	1.64	0.342	0.70 ± 0.04	513.5	1.9	924.5	4.2	3.719	2.6
27	150.27461	1.98884	0.838	4.04 ± 0.59	9.36 ± 2.22	1.98	0.139	1.17 ± 0.10	523.0	1.1	1564.1	3.4	2.198	2.6
28	150.44728	2.05392	0.323	4.63 ± 0.34	5.72 ± 0.67	1.64	1.046	1.08 ± 0.05	659.4	2.4	948.8	4.0	3.623	2.7
29	150.14661	2.06296	0.726	4.63 ± 0.42	9.89 ± 1.45	1.83	0.228	1.23 ± 0.07	570.5	1.3	1483.5	3.5	2.317	1.1
30	150.48813	2.01343	1.100	4.66 ± 0.94	16.89 ± 5.64	2.18	0.116	1.40 ± 0.18	498.0	1.0	1684.7	3.2	2.041	1.6
31	150.01474	2.02936	0.079	0.76 ± 0.10	0.26 ± 0.06	1.68	1.037	0.41 ± 0.02	389.9	4.5	300.1	5.1	1.145	2.9
32	150.51109	2.02699	0.899	4.31 ± 0.87	11.29 ± 3.74	2.04	0.137	1.25 ± 0.15	522.4	1.1	1599.7	3.4	2.149	1.6
33	150.50246	2.06821	0.440	3.78 ± 0.31	4.85 ± 0.63	1.70	0.413	0.99 ± 0.05	592.0	1.8	1155.4	3.9	2.975	2.5
34	150.14520	2.04411	0.361	1.66 ± 0.51	1.21 ± 0.63	1.71	0.163	0.61 ± 0.09	462.5	1.6	1021.8	4.3	3.364	1.1
35	150.21114	2.06981	0.370	0.87 ± 0.35	0.45 ± 0.31	1.94	0.050	0.46 ± 0.07	371.7	1.2	1038.2	4.5	3.311	0.8
36	149.66920	2.07406	0.339	2.90 ± 0.40	2.81 ± 0.63	1.65	0.458	0.82 ± 0.06	561.3	2.0	980.3	4.1	3.507	1.9
37	149.69217	2.05139	0.980	3.25 ± 0.72	8.13 ± 2.97	2.47	0.065	1.08 ± 0.14	461.4	1.0	1639.5	3.4	2.097	1.9
38	149.86638	2.06277	1.196	4.69 ± 0.72	19.46 ± 4.85	2.32	0.101	1.46 ± 0.14	482.0	1.0	1711.3	3.1	2.009	3.9
39	150.27736	2.05303	0.908	3.86 ± 0.79	9.63 ± 3.25	2.11	0.110	1.17 ± 0.14	501.9	1.1	1604.6	3.4	2.142	3.4
40	149.79297	2.12563	0.354	1.75 ± 0.26	1.30 ± 0.32	1.69	0.187	0.63 ± 0.05	471.9	1.6	1008.8	4.2	3.408	1.0
41	150.45384	2.09825	0.823	3.89 ± 0.53	8.58 ± 1.90	1.97	0.136	1.14 ± 0.09	519.0	1.1	1554.5	3.4	2.211	2.7

(1)	(2)	(3)	(4)	(5)	(6)	(7)	(8)	(9)	(10)	(11)	(12)	(13)	(15)	(15)
42	150.00801	2.11899	0.676	3.16 ± 0.41	5.08 ± 1.06	1.93	0.132	0.96 ± 0.07	511.7	1.2	1440.2	3.7	2.387	1.8
43	150.22694	2.11091	1.036	4.49 ± 0.80	14.58 ± 4.23	2.16	0.117	1.34 ± 0.15	503.4	1.0	1662.4	3.2	2.068	2.6
44	150.17979	2.11037	0.360	1.94 ± 0.56	1.54 ± 0.75	1.69	0.211	0.67 ± 0.10	487.1	1.6	1020.0	4.2	3.370	2.0
45	150.09966	2.10513	0.828	2.80 ± 1.05	5.18 ± 3.36	2.26	0.069	0.94 ± 0.20	464.2	1.0	1557.8	3.5	2.207	2.4
46	150.59059	2.13513	0.728	4.71 ± 0.55	10.15 ± 1.92	1.82	0.236	1.24 ± 0.09	573.4	1.3	1485.2	3.5	2.315	2.8
47	149.63463	2.13576	0.962	4.35 ± 0.75	12.49 ± 3.55	2.08	0.125	1.28 ± 0.14	511.8	1.1	1631.3	3.3	2.107	4.2
48	150.50502	2.22506	0.834	16.86 ± 0.49	86.80 ± 3.98	1.47	1.765	3.01 ± 0.06	843.0	1.9	1561.6	3.0	2.201	3.4
49	150.16100	2.13725	0.837	3.28 ± 0.63	6.73 ± 2.14	2.12	0.093	1.03 ± 0.12	487.7	1.1	1563.5	3.5	2.199	2.0
50	150.02039	2.14563	0.958	3.16 ± 0.65	7.54 ± 2.57	2.45	0.064	1.05 ± 0.13	460.6	1.0	1629.5	3.4	2.110	1.8
51	150.05656	2.20854	0.186	1.40 ± 0.13	0.75 ± 0.11	1.62	0.491	0.54 ± 0.02	463.1	2.5	628.5	4.6	5.470	2.0
52	150.44104	2.15873	0.377	2.14 ± 0.30	1.83 ± 0.42	1.69	0.227	0.70 ± 0.05	500.4	1.6	1050.8	4.1	3.272	3.7
53	150.58435	2.18116	0.556	3.51 ± 0.44	5.04 ± 1.01	1.79	0.232	0.98 ± 0.07	553.7	1.4	1314.0	3.7	2.616	2.8
54	150.27829	2.18053	0.373	1.27 ± 0.28	0.81 ± 0.30	1.79	0.097	0.54 ± 0.06	421.6	1.4	1043.6	4.3	3.294	3.0
55	150.02382	2.20323	0.942	5.85 ± 0.65	19.32 ± 3.45	1.87	0.227	1.54 ± 0.11	569.2	1.2	1621.8	3.2	2.120	2.0
56	150.23663	2.20721	0.360	1.73 ± 0.25	1.29 ± 0.30	1.70	0.176	0.63 ± 0.04	469.4	1.6	1020.0	4.2	3.370	3.0
57	149.64966	2.20925	0.954	5.36 ± 0.73	17.11 ± 3.79	1.92	0.190	1.46 ± 0.13	550.2	1.2	1627.6	3.3	2.112	3.6
58	150.09238	2.19365	0.685	2.79 ± 0.47	4.23 ± 1.17	1.98	0.102	0.89 ± 0.09	489.3	1.2	1448.4	3.7	2.373	0.7
59	150.17493	2.21706	0.677	2.74 ± 0.48	4.07 ± 1.18	2.00	0.101	0.88 ± 0.09	487.7	1.2	1441.1	3.7	2.385	3.7
60	149.96271	2.21024	0.425	1.82 ± 0.35	1.52 ± 0.48	1.77	0.134	0.65 ± 0.06	466.2	1.4	1131.8	4.1	3.037	3.4
61	150.00906	2.27497	0.473	2.32 ± 0.58	2.37 ± 0.99	1.78	0.161	0.76 ± 0.10	497.4	1.4	1204.7	4.0	2.854	1.4
62	150.28798	2.27696	0.123	1.03 ± 0.09	0.43 ± 0.06	1.64	0.695	0.47 ± 0.02	426.0	3.3	444.9	4.8	7.727	2.2
63	150.21454	2.28010	0.881	4.97 ± 0.56	13.73 ± 2.49	1.91	0.187	1.35 ± 0.10	551.3	1.2	1589.8	3.3	2.162	0.9
64	149.82921	2.26702	0.379	2.20 ± 0.27	1.93 ± 0.38	1.69	0.235	0.72 ± 0.05	505.1	1.6	1054.3	4.1	3.261	3.2
65	150.43257	2.29931	0.702	3.49 ± 0.74	6.15 ± 2.17	1.90	0.148	1.02 ± 0.13	523.8	1.2	1463.3	3.6	2.349	4.7
66	150.57664	2.25548	0.672	3.51 ± 0.59	5.94 ± 1.64	1.87	0.162	1.02 ± 0.10	530.6	1.3	1436.5	3.6	2.393	4.0
67	150.41566	2.43020	0.124	5.70 ± 0.08	6.26 ± 0.14	1.60	10.15	1.16 ± 0.01	753.0	5.8	448.0	4.2	7.673	1.2
68	149.98329	2.31713	0.932	6.27 ± 0.55	21.24 ± 2.98	1.82	0.263	1.60 ± 0.09	584.7	1.2	1616.9	3.2	2.126	2.4
69	150.32394	2.28235	0.981	4.45 ± 0.61	13.28 ± 2.95	2.10	0.126	1.31 ± 0.11	511.9	1.1	1639.9	3.3	2.096	1.5
70	150.50890	2.28147	0.841	4.16 ± 0.58	9.84 ± 2.23	1.97	0.145	1.19 ± 0.10	527.4	1.2	1566.0	3.4	2.195	3.4
71	150.59309	2.53890	1.045	7.36 ± 0.92	31.94 ± 6.48	1.78	0.304	1.85 ± 0.15	591.6	1.2	1665.8	3.1	2.064	2.8
72	150.34848	2.28162	0.373	2.08 ± 0.27	1.75 ± 0.37	1.69	0.221	0.69 ± 0.05	496.7	1.6	1043.6	4.2	3.294	1.5
73	149.86913	2.30127	0.380	2.19 ± 0.30	1.91 ± 0.42	1.69	0.231	0.71 ± 0.05	503.9	1.6	1056.1	4.1	3.255	3.2
74	149.95262	2.34188	0.942	5.02 ± 0.52	15.21 ± 2.53	1.97	0.170	1.39 ± 0.09	540.9	1.1	1621.8	3.3	2.120	2.4
75	150.02773	2.37396	0.221	1.63 ± 0.15	0.99 ± 0.15	1.62	0.440	0.59 ± 0.03	481.4	2.3	719.8	4.5	4.776	0.8
76	149.70033	2.30070	0.756	3.13 ± 0.58	5.58 ± 1.69	2.01	0.106	0.98 ± 0.10	495.1	1.1	1507.2	3.6	2.281	3.0
77	149.65721	2.32573	0.125	1.07 ± 0.13	0.46 ± 0.09	1.64	0.715	0.48 ± 0.02	431.1	3.3	451.1	4.8	7.620	1.7
78	150.09511	2.30050	0.360	2.19 ± 0.25	1.87 ± 0.34	1.67	0.260	0.71 ± 0.04	507.7	1.7	1020.0	4.2	3.370	3.6
79	149.66328	2.26777	0.676	3.60 ± 0.68	6.22 ± 1.93	1.87	0.167	1.04 ± 0.11	534.5	1.3	1440.2	3.6	2.387	3.0
80	149.92926	2.40902	0.874	3.66 ± 0.55	8.44 ± 2.06	2.11	0.106	1.12 ± 0.10	499.3	1.1	1585.8	3.4	2.168	3.7
81	150.05804	2.38045	0.348	2.56 ± 0.30	2.34 ± 0.44	1.66	0.355	0.77 ± 0.05	536.4	1.8	997.5	4.1	3.446	1.9
82	149.63988	2.34912	0.951	8.17 ± 0.85	32.97 ± 5.50	1.71	0.415	1.92 ± 0.13	634.1	1.3	1626.2	3.1	2.114	1.7

(1)	(2)	(3)	(4)	(5)	(6)	(7)	(8)	(9)	(10)	(11)	(12)	(13)	(15)	(15)
83	150.24123	2.34835	0.723	2.97 ± 0.52	4.90 ± 1.42	2.01	0.104	0.94 ± 0.09	492.3	1.1	1481.1	3.6	2.321	3.4
84	149.72818	2.35804	0.220	1.37 ± 0.21	0.75 ± 0.19	1.64	0.334	0.54 ± 0.04	454.7	2.2	717.3	4.5	4.793	1.2
85	150.53262	2.38075	0.214	1.35 ± 0.27	0.73 ± 0.24	1.64	0.347	0.54 ± 0.05	452.8	2.2	702.1	4.6	4.896	2.6
86	150.48891	2.38385	1.192	3.68 ± 0.75	13.23 ± 4.44	2.74	0.059	1.25 ± 0.15	445.1	0.9	1710.3	3.2	2.010	2.6
87	149.78014	2.39947	0.346	1.26 ± 0.30	0.77 ± 0.30	1.77	0.109	0.54 ± 0.06	423.6	1.5	993.7	4.4	3.459	3.0
88	150.21748	2.40032	0.905	5.15 ± 0.56	14.99 ± 2.63	1.91	0.192	1.40 ± 0.10	553.0	1.2	1603.0	3.3	2.145	3.4
89	150.11433	2.35651	0.221	1.89 ± 0.16	1.24 ± 0.17	1.60	0.565	0.63 ± 0.03	505.7	2.4	719.8	4.4	4.776	1.6
90	150.15298	2.39447	0.899	3.84 ± 0.56	9.44 ± 2.23	2.10	0.110	1.16 ± 0.10	502.4	1.1	1599.7	3.4	2.149	2.8
91	150.09093	2.39116	0.220	2.84 ± 0.14	2.35 ± 0.18	1.59	1.076	0.79 ± 0.02	579.6	2.8	717.3	4.3	4.793	2.1
92	149.69957	2.40280	0.354	1.92 ± 0.42	1.49 ± 0.54	1.68	0.221	0.66 ± 0.07	486.2	1.7	1008.8	4.2	3.408	3.2
93	150.27898	2.41927	0.123	1.04 ± 0.11	0.44 ± 0.07	1.64	0.679	0.47 ± 0.02	426.9	3.3	444.9	4.8	7.727	0.9
94	150.10551	2.42297	0.221	1.91 ± 0.14	1.27 ± 0.14	1.60	0.570	0.64 ± 0.02	507.6	2.4	719.8	4.4	4.776	2.1
95	149.66927	2.47365	0.957	5.59 ± 0.74	18.34 ± 3.93	1.90	0.204	1.50 ± 0.13	557.3	1.2	1629.0	3.2	2.110	4.6
96	149.78217	2.44935	0.675	3.36 ± 0.50	5.57 ± 1.34	1.90	0.147	0.99 ± 0.09	522.2	1.2	1439.3	3.6	2.389	1.1
97	150.08875	2.46070	0.727	3.92 ± 0.44	7.62 ± 1.38	1.88	0.170	1.11 ± 0.08	539.4	1.2	1484.4	3.5	2.316	2.3
98	149.88269	2.44837	0.359	3.15 ± 0.24	3.29 ± 0.40	1.65	0.465	0.87 ± 0.04	573.1	1.9	1018.1	4.0	3.377	1.6
99	150.40971	2.51164	0.883	3.97 ± 0.54	9.69 ± 2.13	2.06	0.122	1.18 ± 0.10	511.2	1.1	1590.9	3.4	2.161	4.5
100	149.94522	2.48562	0.735	5.14 ± 0.49	11.77 ± 1.78	1.80	0.268	1.31 ± 0.08	588.6	1.4	1490.8	3.4	2.306	2.7
101	150.17256	2.52335	0.697	2.89 ± 0.51	4.54 ± 1.33	1.98	0.107	0.91 ± 0.09	492.8	1.2	1459.0	3.7	2.356	4.1
102	150.06664	2.64744	0.696	4.27 ± 0.55	8.34 ± 1.74	1.83	0.213	1.16 ± 0.09	561.3	1.3	1458.1	3.5	2.358	2.9
103	150.00713	2.45343	0.731	3.09 ± 0.50	5.28 ± 1.41	2.00	0.109	0.96 ± 0.09	497.4	1.1	1487.6	3.6	2.311	1.3
104	149.78313	2.46741	0.735	2.23 ± 0.68	3.17 ± 1.64	2.23	0.057	0.80 ± 0.13	445.5	1.0	1490.8	3.7	2.306	1.1
105	150.27148	2.51344	0.704	3.30 ± 0.52	5.65 ± 1.45	1.92	0.134	0.99 ± 0.09	513.9	1.2	1465.1	3.6	2.346	3.2
106	149.92343	2.52499	0.729	21.91 ± 0.37	112.57 ± 2.98	1.42	3.305	3.47 ± 0.04	956.6	2.2	1486.0	3.1	2.313	2.7
107	150.57024	2.49864	1.146	5.84 ± 1.41	25.39 ± 10.21	2.00	0.173	1.65 ± 0.25	528.0	1.1	1698.4	3.1	2.024	1.3
108	150.05560	2.47828	1.160	5.26 ± 0.76	22.16 ± 5.17	2.12	0.136	1.55 ± 0.14	507.4	1.0	1702.2	3.1	2.020	2.3
109	149.91911	2.60087	0.247	1.36 ± 0.21	0.77 ± 0.19	1.66	0.257	0.54 ± 0.04	449.3	2.0	783.2	4.5	4.389	1.2
110	150.23337	2.47628	0.373	2.57 ± 0.24	2.44 ± 0.37	1.67	0.311	0.78 ± 0.04	533.1	1.8	1043.6	4.1	3.294	3.2
111	150.41061	2.58729	0.105	0.83 ± 0.15	0.30 ± 0.09	1.68	0.669	0.43 ± 0.03	398.4	3.5	387.4	5.0	8.873	4.5
112	150.23990	2.56280	0.220	2.02 ± 0.16	1.38 ± 0.17	1.60	0.626	0.66 ± 0.03	516.9	2.5	717.3	4.4	4.793	3.5
113	149.98776	2.58523	0.668	2.62 ± 0.56	3.75 ± 1.33	2.00	0.097	0.86 ± 0.10	482.3	1.2	1432.8	3.7	2.399	1.1
114	149.71248	2.54461	0.478	2.77 ± 0.38	3.15 ± 0.69	1.75	0.212	0.84 ± 0.06	526.7	1.5	1211.9	3.9	2.837	5.0
115	149.98592	2.56490	0.728	2.45 ± 0.55	3.67 ± 1.35	2.16	0.070	0.84 ± 0.10	461.2	1.1	1485.2	3.7	2.315	0.6
116	150.05421	2.58885	0.675	3.95 ± 1.57	7.20 ± 4.96	1.85	0.196	1.10 ± 0.25	551.6	1.3	1439.3	3.6	2.389	2.5
117	150.15816	2.60823	0.893	4.07 ± 0.61	10.16 ± 2.50	2.05	0.125	1.20 ± 0.11	513.3	1.1	1596.5	3.4	2.153	1.9
118	150.11774	2.68425	0.350	8.30 ± 0.32	14.75 ± 0.89	1.63	2.242	1.57 ± 0.04	793.7	2.7	1001.3	3.7	3.433	2.5
119	150.10533	2.72392	0.727	3.69 ± 0.69	6.97 ± 2.13	1.91	0.153	1.07 ± 0.12	528.9	1.2	1484.4	3.6	2.316	2.5
120	150.55049	2.72977	0.349	1.14 ± 0.39	0.66 ± 0.38	1.79	0.093	0.51 ± 0.08	410.0	1.4	999.4	4.4	3.440	11.7
121	150.23537	2.68038	1.840	6.27 ± 0.83	70.00 ± 14.91	2.05	0.140	2.18 ± 0.19	427.6	0.8	1754.1	2.7	1.960	6.3
122	150.30498	2.59318	0.220	1.78 ± 0.33	1.14 ± 0.35	1.61	0.514	0.62 ± 0.06	496.4	2.4	717.3	4.4	4.793	4.3
123	149.91772	2.70088	0.889	6.50 ± 0.76	21.16 ± 4.00	1.79	0.299	1.61 ± 0.12	601.0	1.3	1594.3	3.2	2.156	4.2

(1)	(2)	(3)	(4)	(5)	(6)	(7)	(8)	(9)	(10)	(11)	(12)	(13)	(15)	(15)
124	150.04784	2.69253	0.985	5.15 ± 0.76	16.83 ± 4.04	1.98	0.167	1.44 ± 0.13	536.9	1.1	1641.6	3.2	2.094	0.4
125	149.83878	2.67508	0.260	2.25 ± 0.48	1.71 ± 0.61	1.61	0.527	0.70 ± 0.08	529.1	2.2	813.5	4.3	4.226	5.0
126	149.98460	2.67900	0.678	4.15 ± 0.63	7.79 ± 1.92	1.83	0.213	1.13 ± 0.10	559.9	1.3	1442.0	3.6	2.384	3.0
127	150.00462	2.63275	0.677	2.76 ± 0.65	4.12 ± 1.62	2.00	0.103	0.89 ± 0.12	488.9	1.2	1441.1	3.7	2.385	3.0
128	149.76234	2.63336	0.306	1.23 ± 0.28	0.71 ± 0.27	1.73	0.139	0.52 ± 0.05	426.2	1.6	914.1	4.4	3.761	5.2
129	150.08617	2.53141	0.889	6.79 ± 0.60	22.62 ± 3.17	1.77	0.325	1.66 ± 0.09	610.0	1.3	1594.3	3.2	2.156	2.2
130	150.35568	2.64774	0.397	2.17 ± 0.30	1.92 ± 0.43	1.70	0.209	0.71 ± 0.05	499.1	1.6	1085.5	4.1	3.167	4.5
131	150.12906	2.59564	0.350	1.99 ± 0.32	1.58 ± 0.42	1.67	0.235	0.67 ± 0.06	493.1	1.7	1001.3	4.2	3.433	1.9
132	149.87796	2.57805	0.696	4.16 ± 0.49	8.02 ± 1.53	1.83	0.205	1.14 ± 0.08	556.6	1.3	1458.1	3.5	2.358	2.8
133	150.11256	2.55609	0.501	3.20 ± 0.42	4.06 ± 0.86	1.75	0.243	0.91 ± 0.07	547.7	1.5	1243.8	3.8	2.764	2.2
134	150.03307	2.55249	0.747	2.63 ± 0.77	4.20 ± 2.07	2.15	0.077	0.88 ± 0.14	469.0	1.1	1500.3	3.6	2.291	0.2
135	149.88622	1.94188	0.372	1.86 ± 0.30	1.46 ± 0.39	1.70	0.184	0.65 ± 0.05	478.1	1.6	1041.8	4.2	3.300	3.8
136	150.42104	1.98448	0.322	1.96 ± 0.37	1.50 ± 0.46	1.66	0.269	0.66 ± 0.06	495.5	1.8	946.8	4.2	3.631	0.8
137	150.19861	2.06839	0.186	1.10 ± 0.27	0.51 ± 0.21	1.67	0.324	0.49 ± 0.05	426.4	2.3	628.5	4.7	5.470	0.8
138	149.78191	2.13906	0.355	1.30 ± 0.52	0.82 ± 0.56	1.76	0.112	0.54 ± 0.10	427.1	1.5	1010.7	4.3	3.401	1.0
139	149.72893	2.23739	0.381	2.62 ± 0.37	2.53 ± 0.58	1.68	0.307	0.79 ± 0.06	534.5	1.7	1057.8	4.1	3.250	4.2
140	150.09077	2.20568	0.427	1.39 ± 0.35	0.99 ± 0.42	1.84	0.083	0.57 ± 0.07	425.5	1.3	1135.0	4.2	3.029	0.7
141	149.99364	2.25854	0.660	2.91 ± 0.81	4.37 ± 2.03	1.93	0.120	0.91 ± 0.14	500.9	1.2	1425.3	3.7	2.412	1.4
142	150.41328	2.40997	0.385	5.13 ± 0.24	7.28 ± 0.54	1.66	0.867	1.17 ± 0.03	668.1	2.2	1064.9	3.8	3.228	1.2
143	149.73943	2.34139	1.028	4.72 ± 0.70	15.60 ± 3.76	2.10	0.131	1.38 ± 0.13	513.5	1.1	1659.3	3.2	2.072	1.2
144	150.29137	2.41073	0.374	1.37 ± 0.29	0.92 ± 0.31	1.77	0.109	0.56 ± 0.05	432.3	1.4	1045.4	4.3	3.288	0.9
145	150.54851	2.49870	0.880	4.75 ± 1.11	12.79 ± 4.95	1.93	0.173	1.32 ± 0.19	543.4	1.2	1589.2	3.3	2.163	1.3
146	149.93796	2.60627	0.342	2.98 ± 0.23	2.94 ± 0.36	1.65	0.468	0.84 ± 0.04	565.4	2.0	986.1	4.1	3.486	1.2
147	149.97781	2.56936	0.308	0.68 ± 0.31	0.28 ± 0.22	1.95	0.048	0.41 ± 0.07	349.8	1.3	918.3	4.7	3.744	0.6
148	149.78278	1.92934	0.769	2.50 ± 0.61	4.00 ± 1.62	2.24	0.065	0.86 ± 0.12	457.0	1.0	1517.0	3.6	2.266	3.7
149	150.12646	1.99926	1.019	4.22 ± 0.61	12.90 ± 3.02	2.19	0.106	1.28 ± 0.11	496.0	1.0	1655.8	3.3	2.076	1.7
150	150.19350	2.04099	1.190	3.80 ± 0.79	13.85 ± 4.78	2.64	0.064	1.27 ± 0.16	450.1	0.9	1709.8	3.2	2.011	1.7
151	150.28905	2.11303	0.887	2.45 ± 1.28	4.58 ± 4.26	2.64	0.045	0.88 ± 0.25	434.3	0.9	1593.2	3.5	2.158	3.7
152	150.58397	2.32155	0.720	2.71 ± 0.72	4.23 ± 1.89	2.07	0.088	0.89 ± 0.13	478.0	1.1	1478.6	3.7	2.325	4.0
153	150.14027	2.35035	0.221	1.20 ± 0.15	0.61 ± 0.12	1.66	0.268	0.51 ± 0.03	435.0	2.1	719.8	4.6	4.776	1.6
154	150.22540	2.26873	0.677	2.91 ± 0.53	4.46 ± 1.35	1.95	0.114	0.91 ± 0.10	497.6	1.2	1441.1	3.7	2.385	0.9
155	150.02414	2.36050	0.726	2.09 ± 0.61	2.85 ± 1.39	2.32	0.051	0.77 ± 0.12	437.4	1.0	1483.5	3.7	2.317	0.8
156	150.13132	1.85240	0.529	1.90 ± 0.38	1.87 ± 0.62	1.92	0.089	0.69 ± 0.07	456.0	1.2	1280.6	4.0	2.685	3.7
157	149.87077	2.47241	1.220	4.39 ± 0.73	18.13 ± 4.94	2.46	0.084	1.41 ± 0.15	467.5	0.9	1716.8	3.1	2.002	1.6
158	149.94072	1.82807	0.369	0.86 ± 0.41	0.43 ± 0.36	1.94	0.049	0.45 ± 0.09	370.0	1.2	1036.4	4.5	3.317	0.7
159	150.01929	2.43490	0.220	0.80 ± 0.17	0.33 ± 0.12	1.78	0.133	0.43 ± 0.04	380.6	1.8	717.3	4.8	4.793	1.3
160	150.03670	2.55126	0.889	3.04 ± 0.70	6.44 ± 2.48	2.30	0.071	1.00 ± 0.13	466.7	1.0	1594.3	3.5	2.156	0.2
161	150.04230	2.69490	0.219	1.72 ± 0.24	1.07 ± 0.25	1.61	0.493	0.60 ± 0.04	490.3	2.4	714.8	4.5	4.810	0.4
162	150.06133	2.11702	0.663	3.07 ± 0.45	4.75 ± 1.14	1.92	0.131	0.94 ± 0.08	508.9	1.2	1428.1	3.7	2.407	1.5
163	150.05057	2.13923	0.959	2.64 ± 0.88	5.72 ± 3.25	2.74	0.043	0.94 ± 0.18	433.9	0.9	1629.9	3.4	2.109	1.5
164	149.84900	1.89033	0.782	2.31 ± 0.70	3.61 ± 1.85	2.36	0.053	0.83 ± 0.14	443.1	1.0	1526.5	3.6	2.252	3.1
165	150.34712	2.36811	1.470	4.75 ± 0.87	28.56 ± 8.62	2.51	0.082	1.61 ± 0.19	439.8	0.9	1752.0	2.9	1.962	4.2

Acknowledgments

Curriculum Vitæ

Name:	Patrícia Figueiró Spinelli
Citizenship:	Brazilian
Date of birth:	02 July 1983
Place of birth:	Caxias do Sul, Brazil

Education

- **2007–2011, Ph.D in Astrophysics**
  University Observatory Munich, Faculty of Physics, Ludwig-Maximilians-Universität (USM-LMU) & International Max Planck Research School (IMPRS)
  Munich, Germany

- **2005–2007, Masters in Physics**
  Faculty of Physics, Universidade Federal do Rio Grande do Sul (IF-UFRGS)
  Porto Alegre, Brazil

- **2001–2004, Bachelor in Physics**
  Faculty of Physics, Universidade Federal do Rio Grande do Sul (IF-UFRGS)
  Porto Alegre, Brazil

- **1998–2000, High School**
  Escola Santa Catarina
  Caxias do Sul, Brazil